



Max Planck Institut für Kolloid und Grenzflächenforschung



“Reactive Hard Templating”
From Carbon Nitrides to Metal Nitrides
Dissertation

zur Erlangung des akademischen Grades
"doctor rerum naturalium"
(Dr. rer. nat.)
in der Wissenschaftsdisziplin Kolloidchemie

eingereicht an der
Mathematisch-Naturwissenschaftlichen Fakultät
der Universität Potsdam

von
Anna Fischer

Potsdam, März 2008

This work is licensed under a Creative Commons License:
Attribution - Noncommercial - Share Alike 2.0 Germany
To view a copy of this license visit
<http://creativecommons.org/licenses/by-nc-sa/2.0/de/>

Online published at the
Institutional Repository of the Potsdam University:
<http://opus.kobv.de/ubp/volltexte/2008/1977/>
[urn:nbn:de:kobv:517-opus-19777](http://nbn-resolving.org/urn:nbn:de:kobv:517-opus-19777)
[<http://nbn-resolving.de/urn:nbn:de:kobv:517-opus-19777>]

Abstract

Nanostructured inorganic materials are routinely synthesized by the use of templates. Depending on the synthesis conditions of the product material, either “soft” or “hard” templates can be applied. For sol-gel processes, usually “soft” templating techniques are employed, while “hard” templates are used for high temperature synthesis pathways. In classical templating approaches, the template has the unique role of structure directing agent, in the sense that it is not participating to the chemical formation of the resulting material. This work investigates a new templating pathway to nanostructured materials, where the template is also a reagent in the formation of the final material. This concept is described as “reactive templating” and opens a synthetic path toward materials which cannot be synthesised on a nanometre scale by classical templating approaches. Metal nitrides are such kind of materials. They are usually produced by the conversion of metals or metal oxides in ammonia flow at high temperature ($T > 1000^{\circ}\text{C}$), which make the application of classical templating techniques difficult.

Graphitic carbon nitride, $g\text{-C}_3\text{N}_4$, despite its fundamental and theoretical importance, is probably one of the most promising materials to complement carbon in material science and many efforts are put in the synthesis of this material. A simple polyaddition/elimination reaction path at high temperature ($T = 550^{\circ}\text{C}$) allows the polymerisation of cyanamide toward graphitic carbon nitride solids. By hard templating, using nanostructured silica or aluminium oxide as nanotemplates, a variety of nanostructured graphitic carbon nitrides such as nanorods, nanotubes, meso- and macroporous powders could be obtained by nanocasting or nanocoating. Due to the special semi-conducting properties of the graphitic carbon nitride matrix, the nanostructured graphitic carbon nitrides show unexpected catalytic activity for the activation of benzene in Friedel-Crafts type reactions, making this material an interesting metal free catalyst. Furthermore, due to the chemical composition of $g\text{-C}_3\text{N}_4$ and the fact that it is totally decomposed at temperatures between 600°C and 800°C even under inert atmosphere, $g\text{-C}_3\text{N}_4$ was shown to be a good nitrogen donor for the synthesis of early transition metal nitrides at high temperatures. Thus using the nanostructured carbon nitrides as “reactive templates” or “nanoreactors”, various metal nitride nanostructures, such as nanoparticles and porous frameworks could be obtained at high temperature. In this approach the carbon nitride nanostructure played both the role of the nitrogen source and of the exotemplate, imprinting its size and shape to the resulting metal nitride nanostructure.

Zusammenfassung

Die Nanostrukturierung anorganischer Materialien, d.h. die Kontrolle ihrer Form und Größe auf der Nanometerebene durch unterschiedliche Herstellungsverfahren, ist ein sich immer noch erweiterndes Forschungsgebiet. Eine solche Nanostrukturierung wird oft über sogenannte Templatierungsverfahren erreicht: Hier werden Formgeber (Template) mit definierter Morphologie und Größe verwendet und deren Struktur in ein neues Material abgebildet. Templatierungsverfahren können, je nach der Beschaffenheit des Templats, zwischen „weich“ und „hart“ unterschieden werden. Die Begriffe beziehen sich dabei vor allem auf die mechanische und thermische Stabilität der Template, d.h. weiche Template sind vornehmlich organischer, harte Template anorganischer Natur. Wo weiche Template in milden chemischen Verfahren eingesetzt werden, werden harte Template zur Herstellung von Materialien bei Hochtemperaturverfahren verwendet (z. B. poröse Kohlenstoffe). Allgemein dienen Template ausschließlich als Strukturgeber und gehen in keiner Weise in Form einer chemischen Reaktion in die Synthese des gewünschten Materials mit ein. Gegenstand dieser Arbeit ist ein neues Templatierungsverfahren: Die „reaktive Templatierung“. Hierbei wird das Templat - neben seiner Funktion als Strukturgeber – auch als Reagenz für die Synthese des Produktes verwendet. Dieser Synthese-Ansatz öffnet damit neue Wege für die Synthese von nanostrukturierten Materialien, die durch klassische Templatierungsansätze schwer zugänglich sind. Hierzu zählen zum Beispiel die Metallnitride. Üblicherweise werden Metallnitride über die Umsetzung von Metallen oder Metalloxiden in einem Ammoniakstrom bei Mindesttemperaturen von 1000°C gewonnen, was die Anwendung klassischer Templatierungsverfahren beinahe unmöglich macht. Darüber hinaus sind konzentrierte Lauge oder Flusssäure, welche zur Entfernung klassischer harter Template benötigt werden auch Aufschlussmittel für Metallnitride.

Graphitisches Kohlenstoffnitrid, $g\text{-C}_3\text{N}_4$, ist wohl eines der meistversprechendsten Materialien um Kohlenstoff in der Materialwissenschaft zu ergänzen. Es wurden bereits viele potentielle Syntheseansätze beschrieben. Eine durch Groenewolt M. erstellte Route ist die thermisch induzierte Polykondensation von Cyanamid (NCNH_2) bei 550°C. Da $g\text{-C}_3\text{N}_4$ sich zwischen 600°C und 800°C vollständig in NH_3 und $\text{C}_x\text{N}_y\text{H}$ -Gase zersetzt, ist es eine geeignete Festkörper-Stickstoffquelle für die Herstellung von Metalnitriden. Daher boten sich nanostrukturierte graphitische Kohlenstoffnitride als geeignete reaktive Template oder Nanoreaktoren zur Herstellung von nano-strukturierten Metalnitriden an. Die Templatierung der $g\text{-C}_3\text{N}_4$ -Matrix wurde über klassische Harttemplatierungsverfahren erreicht. So konnte eine

Vielzahl nano-strukturierter $g\text{-C}_3\text{N}_4$ Materialien synthetisiert werden wie zum Beispiel Nanostäbchen, Nanoröhren, mesoporöse oder makroporöse graphitische Kohlenstoffnitride. Diese haben sich interessanterweise, als metalfreie Katalysatoren für die Aktivierung von Benzol in Friedel-Crafts-Acylierung und -Alkylierung erwiesen. Durch die Infiltrierung der nano-strukturierten $g\text{-C}_3\text{N}_4$ -Materialien mit diversen Metal-Präkursoren und nachfolgendem Tempern bei 800°C unter Schutzgas, konnten entsprechende nano-strukturierte Metalnitride, als Nanoabdrücke der vorgegebenen Kohlenstoffnitrid Nanostrukturen hergestellt werden. So konnten TiN, VN, GaN, AlGaN und TiVN Nanopartikel synthetisiert werden, macroporöse TiN/Kohlenstoff Komposite sowie TiN Hohlkugeln. Die so hergestellten Materialien erwiesen sich als effektive basische Katalysatoren für Aldol-Kondensations Reaktionen.

Table of Contents

Table of Contents	4
1 Introduction	7
1.1 Metal Nitrides	7
1.2 Creation of nanostructures through hard templating	8
1.3 Graphitic carbon nitride or g-C₃N₄	10
1.3.1 Synthesis of bulk g-C ₃ N ₄	13
2 Characterisation methods	19
2.1 Nitrogen sorption	19
2.1.1 Determination of the surface area.....	20
2.1.2 Determination of the pore size of mesoporous materials.....	21
2.2 Electron microscopy (EM)	22
2.2.1 Scanning electron microscopy (SEM).....	23
2.2.2 Transmission electron microscopy (TEM).....	25
2.3 X-Ray Diffraction	26
3 Experimental Section	32
3.1 Synthesis of nanostructured graphitic carbon nitrides	32
3.1.1 Synthesis of mesoporous graphitic carbon nitrides (mpg-C ₃ N ₄)	32
3.1.2 Synthesis of macroporous graphitic carbon nitrides.....	33
3.1.3 Synthesis of bimodal graphitic carbon nitride (bmg-C ₃ N ₄).....	34
3.1.4 Synthesis of graphitic carbon nitrides nanorods and nanotubes.....	34
3.1.5 Synthesis of graphitic carbon nitride coatings on mesoporous silica microspheres....	35
3.2 Synthesis of nanostructured metal nitrides	35
3.2.1 Synthesis of metal nitride nanoparticles in mpg-C ₃ N ₄	35
3.2.2 Synthesis of ternary metal nitride alloy nanoparticle A _x B _(1-x) N	36
3.2.3 Synthesis of a macroporous titanium nitride/carbon composite.....	36

3.2.4	Synthesis of mesoporous titanium nitride from mesoporous anatase	37
4	Synthesis and characterisation of nanostructured graphitic carbon nitrides	39
4.1	Synthesis of mesoporous graphitic carbon nitride (mpg-C₃N₄)	39
4.1.1	The template	39
4.1.2	The synthetic strategy	40
4.1.3	The removal of the template	42
4.1.4	Characterisation of mesoporous graphitic carbon nitride with 12 nm pores (mpg-C ₃ N ₄ -LHS40)	44
4.1.5	Characterisation of mesoporous graphitic carbon nitride with 23nm pores (mpg-C ₃ N ₄ -LTMA).....	48
4.1.6	Mesoporous g-C ₃ N ₄ as metal free catalyst for benzene activation in Friedel-Crafts type reactions.....	52
4.2	Synthesis of macroporous graphitic carbon nitride	57
4.3	Synthesis and characterisation of bimodal graphitic carbon nitride	60
4.4	Synthesis and characterisation of carbon nitride coatings on mesoporous silica structures	62
4.4.1	Synthesis of carbon nitride coatings on silica microspheres	62
4.5	Synthesis of graphitic carbon nitride nanorods and nanotubes	66
5	Metal nitride nanostructures through reactive hard templating with graphitic carbon nitrides	70
5.1	Synthesis of binary metal nitride nanoparticles in a meso-porous graphitic carbon nitride nanoreactor	70
5.1.1	Synthesis of titanium nitride nanoparticles	72
5.1.2	Synthesis of vanadium and gallium nitride nanoparticles	78
5.1.3	Synthesis of ternary metal nitride nanoparticles in a mesoporous graphitic carbon nitride nanoreactor	82
5.1.4	Synthesis of TiVN nanoparticles in mesoporous graphitic carbon nitride.....	88
5.2	Synthesis of a macroporous titanium nitride/carbon foam	94
5.3	Synthesis of titanium nitride/carbon hollow spheres	99

5.4	Synthesis of mesoporous titanium nitride into mesoporous titanium oxide: maintaining the structure through the nitrogen source	103
5.4.1	Synthesis of mesoporous titanium nitride	104
5.4.2	Application of mesoporous TiN in catalysis	110
6	Conclusion and outlook.....	114
7	Instrumental details	116
8	Publication List	118
9	Acknowledgements.....	119
10	References	120

1 Introduction

The aim of this work is to synthesize nanostructured graphitic carbon nitride materials and to investigate their use as nanoreactors for the synthesis of nanostructured metal nitrides. The underlying idea of this synthetic approach toward metal nitride nanostructures is the new concept of “reactive hard templating”. This concept implies that the structuring agent, or the hard template which gives the final nanostructure to the synthesized material, also acts as the reagent in the chemical formation reaction of the product material. Since the reactive template, in our case nanostructured g-C₃N₄, is itself prepared by templating, the here described synthetic approach toward metal nitrides can be regarded as repeated templating.^[1]

1.1 Metal Nitrides

Metal nitrides are a class of material, which have received a growing attention during the past decade because of their technological importance. Compared to metal oxides or metals, the properties of the corresponding nitrides are superior in some respects. For example transition metal nitrides are used because of their extremely high melting points, their hardness, their quasi metallic conduction properties, their opto-electronic properties, as well as their catalytic activity. For example, TiN melts at temperatures higher than 3000°C, is used for its hardness as super-hard coating in the manufacturing of cutting tools^[2] and also catalytic activity was reported.^[3, 4] VN is known for similar properties.^[5, 6] Group III nitrides such as AlN and GaN are typical wide band-gap semiconductors and find a multitude of applications in high power, short-wavelength optoelectronic devices, in field-effect transistors, thermal radiation sensors and electric coatings.^[7]

Metal nitrides traditionally were produced by heating the corresponding metal with elemental nitrogen at very high temperatures. This preparation method is highly energy consuming because long reaction times at elevated temperatures are required ($T > 1300^{\circ}\text{C}$) and leads usually to low surface area materials. Procedures leading to high surface area materials are related on the utilisation of more reactive nitrogen sources, which require lower temperature to assure the complete conversion to the metal nitride. Thus nowadays new synthetic strategies to high surface area metal nitrides are based on the conversion of metal oxide nanopowders into the corresponding nitride using nitrogen sources, such as ammonia^[6, 8, 9] or hydrazine.^[10, 11] Also synthetic routes based on the thermolysis of metal-amine complexes are reported.^[12] Recently, Zhao *et al.*^[13, 14] reported the synthesis of metal nitrides by using carbon nitride

related materials as nitrogen source. Thus g-C₃N₄ nanostructures should be suitable reactive hard templates for the synthesis of nanostructured metal nitrides.

1.2 Creation of nanostructures through hard templating

Nanostructured materials have become a field of research on its own, since materials properties can highly profit from the introduction of nanosized dimensions into their structure. A good example to illustrate this is related to the field of catalysis. In catalysis high surface area materials are required due to the multiplication of accessible catalytic sites on their surface, compared to the bulk material yielding enhanced catalytic properties. That is why most of the reported heterogeneous catalysts are nanosized materials, such as nanoparticles, supported nanoparticles, microporous zeolites or mesoporous metal oxides. Several of these nano-sized materials can be produced by templating techniques. The “templating” process in general involves the replication of one structure into another with structural inversion. In analogy to macroscopic procedures, such as metal manufacturing, this process is also called “casting” or “moulding”. The soldiers in **Figure 1.1** are in fact cast from a preformed mould, which is filled with molten metal. Once the metal is cooled, the mould is removed and the final soldiers are ready for the shelf of some collector.

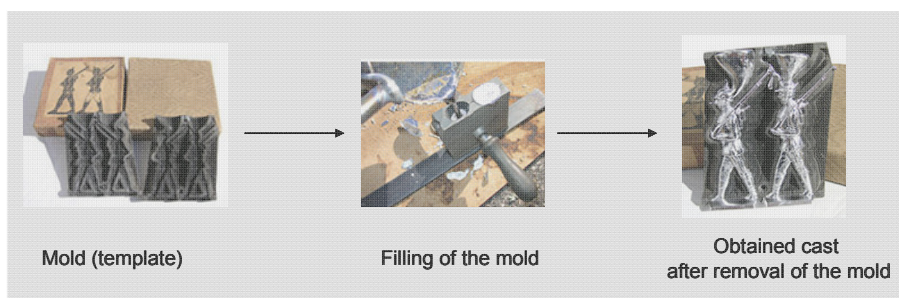


Figure 1.1: Mould casting in metal manufacturing.

In the context of material chemistry, the expression “template” is another word for a structure-directing agent. For example, the micropores in zeolites (pore size < 2 nm) result from the replication of single molecules, while mesoporous silicas (pore size 2-50 nm) result from the replication of self-assembled molecular aggregates such as micelles. In strict terms, a “true” templating or “nanocasting” results in a product material which is a one-to-one inverse copy, or replica, of the template morphology. Templating is a versatile technique for the formation of nanoshaped materials, as the size and shape of the obtained material can be easily adjusted by choosing an appropriate template with various sizes and morphologies. Thus if one is interested in the synthesis of spherical nanoparticles, a mesoporous silica with spherical pores is a template of choice, whereas for rod-like structures a mesoporous silica with a cylindrical channel structure would be required. Beside the nanocasting, nanocoating techniques deposit

only a thin layer on the surface of the template, resulting after its removal into partially replicated structures. The difference between nanocasting and nanocoating is schematically depicted in **Figure 1.2**.

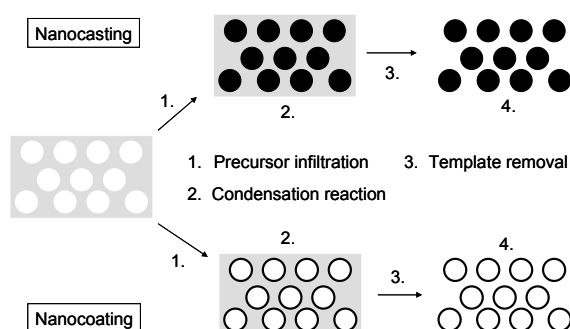


Figure 1.2: Schematic presentation of templating approaches towards nanostructured materials using nanocasting and nanocoating techniques.

In general, templating procedures can be classified into two types, dependent on the template used. On the one hand, there are the so called “soft” templates, which can be single molecules or aggregates such as surfactant or block-copolymer micelles. Those templates are widely used for the synthesis of inorganic nanostructures resulting from soft chemistry processes, i.e. chemistry at low temperatures and pressures, from molecular or colloidal precursors. On the other hand, for materials affording much harsher synthesis conditions, such as for example high temperature carbonisation for porous carbon materials, so called “hard” templates, mostly inorganic nanostructures made of silica or aluminium oxide are employed. While the soft templates are usually removed by extraction or calcination, the hard templates need to be etched away to free the required nanostructures. For silica templates NaOH or HF are commonly used. Moreover, the templates are classified in exo- and endotemplates, depending if the synthesised material condenses inside the template (exotemplates), or around the template (endotemplate),^[15] as shown in **Figure 1.3**.

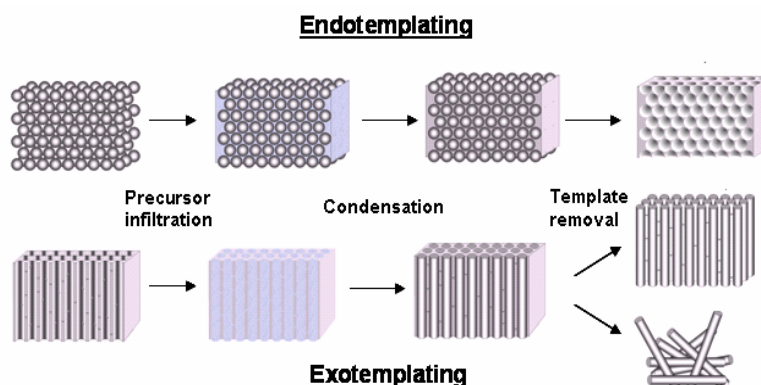


Figure 1.3: Schematic presentation of templating approaches towards nanostructured materials using endo- and exotemplates.

For the synthesis of nanoshaped metal nitrides through reactive hard templating, it was necessary to design g-C₃N₄ “reactive nano hard templates” or “nanoreactors”. The synthesis of graphitic carbon nitride, based on the condensation of cyanamide, is a high temperature process ($T > 500^{\circ}\text{C}$), as will be shown below. This means that in order to produce nanostructured g-C₃N₄, hard templates need to be used. In this work, both endotemplates and exotemplates were used to produce nanostructured g-C₃N₄ leading to various reactive templates in sizes and morphologies.

1.3 Graphitic carbon nitride or g-C₃N₄

One of the oldest carbon nitride related material, a polymeric derivative, was made by Berzelius in 1830 and named by Liebig as “melon” in 1834.^[16] In 1985 Cohen predicted for that diamond like β -C₃N₄, derived in structure from β -Si₃N₄, should be of similar hardness and low compressibility as diamond.^[17-19] Since then many other crystalline phases of C₃N₄ were predicted^[20, 21] (such as α -C₃N₄^[22], “pseudo-cubic” C₃N₄^[23] and “cubic” C₃N₄^[24]). However, at ambient conditions, graphitic C₃N₄ (g-C₃N₄) is regarded to be the most stable allotrope. g-C₃N₄ is a potentially useful substitute for amorphous and graphitic carbon in a variety of material science applications, e.g. as a catalyst or an active catalytic support, as a membrane material or for gas storage^[25]. This has motivated much research into novel procedures for the synthesis of defined carbon nitride materials and towards improving understanding of the reaction sequence. Both triazine and tri-s-triazine were discussed as tectonic units to constitute potential allotropes of g-C₃N₄, which differ in their stability – due to the different electronic environment of the N atom – and the size of the nitride pores, as seen in **Figure 1.4**.

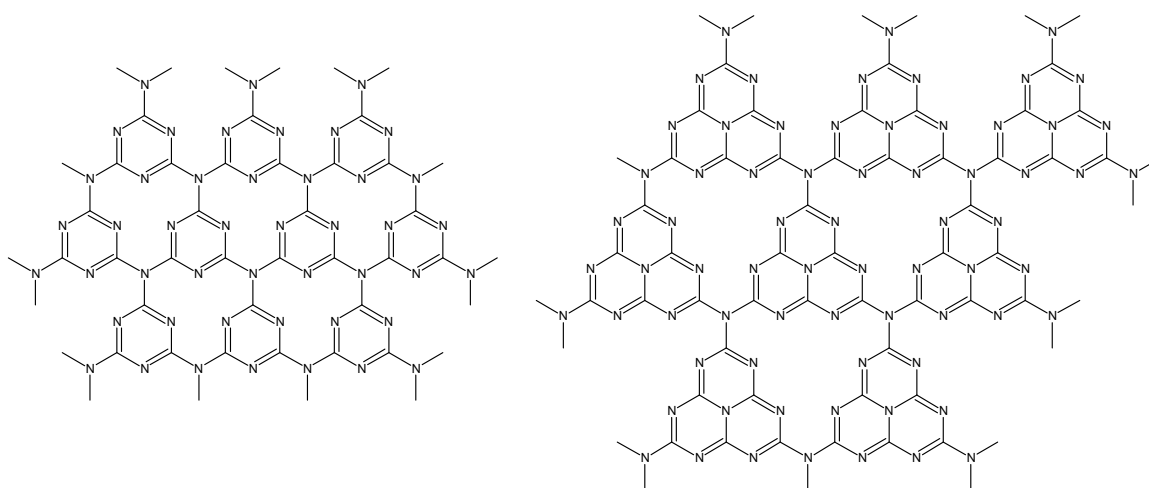


Figure 1.4: triazine- (left) and tri-s-triazine-based (right) connection patterns of potential g-C₃N₄ allotropes.

In fact Kroke *et al.*^[21] calculated on the base of DFT that the tris-*s*-triazine based structure is by 30 KJ/mol more stable than the triazine based one, so that it is widely admitted that g-C₃N₄ is built from tri-*s*-triazine units. Even after 30 years of intensive research the “ideal” g-C₃N₄ material has still not been synthesised. However the synthesis of g-C₃N₄-like materials covers a broad spectrum of synthesis routes starting from diverse carbon and nitrogen sources. **Table 1.1** gives an overview about recent synthesis procedures of carbon nitride materials approaching the ideal g-C₃N₄. For example, Kouvetakis *et al.* reported on the decomposition of derivatized melamine precursors between 400°C and 500°C. They obtained an amorphous carbon nitride with about correct composition but only a broad graphitic stacking peak was observed in the X-Ray diffraction.^[26] The solvothermal condensation of melamine with cyanurichloride, which also worked at larger scales, was investigated by Montigaud *et al.*^[27] The condensation reaction performed at 250 C and 140 MPa revealed a weakly condensed product with low order and many pendant amino groups. In another work, they also reported on the pyrolysis of melamine in presence of hydrazine to 800 °C at 2.5 GPa, which resulted in carbonitrides with about perfect graphitic stacking, but a large excess of carbon was found in the material and no regular in-plane order was observed.^[28] Zhang *et al.* used 2-amino-4,6-dichlorotriazine as a precursor in a high pressure-high temperature approach and obtained a close-to-crystalline graphitic-C₃N₄ derivative, where the HCl generated *in-situ* during the reaction played the role of a template to fill the nitridic in-plane holes of a triazin-based condensation pattern.^[29] The structure of the products was quite refined, as they exhibited both, a regular in plane packing of the nitridic triazine-based holes as well as X-ray patterns which could be quantitatively assigned. Guo *et al.* showed that g-C₃N₄ is an outcome of the solvothermal reaction between cyanurichloride and sodiumamide in benzene by heating to about 200 °C for 8 – 12 h.^[30] The same group reported on the synthesis by a similar reaction of carbon-nitride nanotubes from cyanurichloride and sodiumazide.^[31] Graphitic packing in the nanotubes samples was less pronounced compared to the bulk material, which however can also be due to the nanostructure. Komatsu *et al.*^[32, 33] reported on a highly ordered model carbon nitride, C₉₁H₁₄N₁₂₄. The same group also reported about a highly crystalline species which they called “high molecular weight” melon.^[34, 35] The X-ray diffractograms of both observed species were – for polymeric materials – highly textured. Another benchmark-step towards better defined and organized graphitic C₃N₄ systems was published by Schnick *et al.*^[36] They were able to isolate and solve the crystal structure of another rather stable intermediate, 2,5,8-triamino-tri-*s*-triazine, or the so called melon (C₆N₁₀H₆).

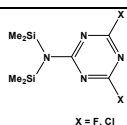
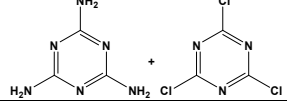
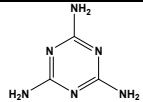
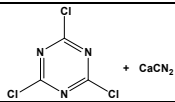
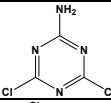
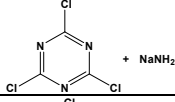
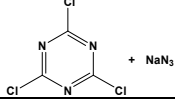
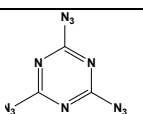
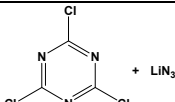
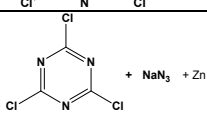
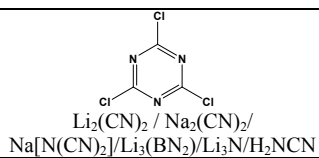
Precursor	Conditions	Temp. °C	C:N ratio of the product ^a	Observations	Ref.
	Thin layer deposition (CVD)	450-500	0.81	Amorphous material	Kouvetakis 1994 [26]
	Solvothermal, in super-critical Et ₃ N (140 MPa)	250	0.81 (37 at % of H)	Slightly Crystalline material	Montigaud 2000 [27]
	Solvothermal in hydrazine (2.5 GPa)	800-850	0.90 (19 at % of H)	Crystalline material	Montigaud 2000 [27]
	Solid state reaction	500-550	0.75	Crystalline material (some amounts of graphite)	Gu 2003 [37]
	Solid state reaction (1-1.5 GPa)	500-600	0.68 (7 at % of Cl)	Crystalline material	Zhang 2001 [29]
	Solvothermal in benzene	180-220	0.72	Crystalline material	Guo 2003 [30]
	Solvothermal in benzene	220	0.80	Nanotubes	Guo 2004 [31]
(C ₆ N ₇ (NCNK) ₃) _n + C ₆ N ₇ Cl ₃	Solid state reaction	300→600	0.71	Oligomere	Komatsu 2001 [34]
Melone	Solid state reaction	700	0.67	Crystalline material	Komatsu 2001 [35]
	Thermal Decomposition	185	0.77	Amorphous	Gillan 2000 [38]
C ₆ N ₇ (N ₃) ₃	Thermal Decomposition	~ 200°C	0.83-0.71	Amorphous (Rods / Porous Materials)	Gillan 2007 [39]
	Solid state reaction	500°C	0.8	Amorphous (hollow spheres)	Zimmerman 2001 [40]
	Solid State reaction (400 MPa)	220°C	1.01	Crystalline (Nanowires)	Lu 2007 [41]
Melamine / Dicyandiamide	CCl ₄ (4.5-5 MPa)	290°C	0.72	Graphite like nanobelts and nanotubes	Li 2007 [42]
	Solid state reaction	250°C-350°C	0.61-0.70	Micro- and Nanotubular	Tragl 2007 [43]
Melamine	Solid state reaction	350°C-650°C	0.65	Crystalline (flake and strip-like morphology)	Zhao 2005 [44]
Tricyanomelaminates salts	Thermal Decomposition	> 450°C	0.66	Graphitic	Lotsch 2006 [45]

Table 1.1: Some recent reported syntheses of carbon nitrides approaching the ideal g-C₃N₄ material. [a] The C:N ratio of ideal C₃N₄ is 0.75.

Contrary to the experiments reported by Komatsu further heating only resulted in badly defined amorphous graphitic- C_3N_4 , as reported by the authors. Recently, the same group of authors was able to clarify the structure of a highly defined melon polymer^[46] thus giving further evidence that already the polymeric species can undergo high local crystal packing. Physical and chemical vapor deposition methods to synthesize thin films are also described quite often^[47-50] but all of them are dogged by the elimination of the very stable N_2 , which results in disordered, quite carbon-rich materials.

1.3.1 Synthesis of bulk $g-C_3N_4$

The synthetic strategy toward $g-C_3N_4$ material presented here is based on the self-condensation of cyanamide (dicyandiamide or melamine) and was developed by M. Groenewolt^[51] following the reaction path described in **Figure 1.5**.

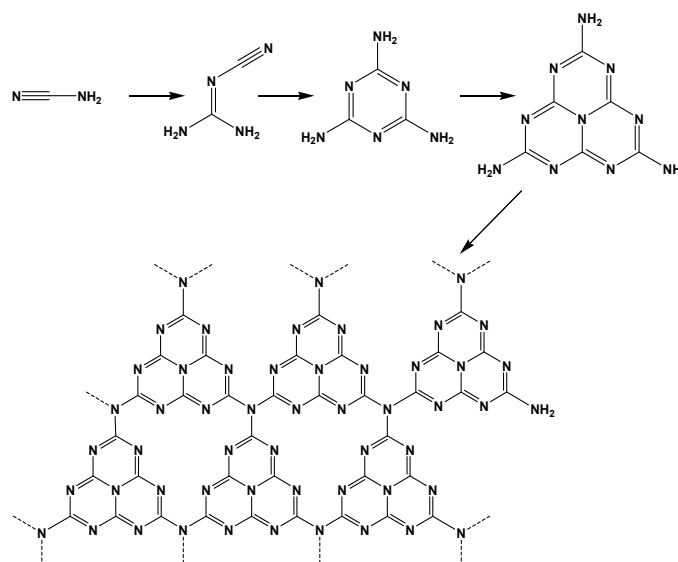


Figure 1.5: Reaction path for the formation of graphitic C_3N_4 out of cyanamide

The synthesis via a readily accessible liquid monomer (cyanamide) toward $g-C_3N_4$ is certainly one of the advantages of this synthesis allowing it to be easily combined with hard templates to yield nanostructured $g-C_3N_4$ nanoreactors with high surface areas and defined morphologies. The reaction is a combination of polyaddition and polycondensation reaction scheme where the precursors are first condensing into melamine at around 235°C . The second step is a condensation under release of ammonia. Up to 350°C essentially melamine based products are found, while the tri-s-triazine nucleus forms via melamine rearrangements at around 390°C , as already reported by Schnick *et al.* in the synthesis of melem.^[36] This condensation product is rather stable and can be isolated by stopping the reaction at 400°C in closed glass tubes under

high partial pressure of ammonia. Condensation of this unit to polymers, networks and potentially final polymeric- C_3N_4 occurs at around 520°C . Finally the material starts to decompose slightly above 600°C . Heating to 800°C results in the residue-free disappearance of the material via the generation of ammonia and $C_xN_yH_z$ gases, as shown by TGA-MS measurements (**Figure 1.6**). One yield limiting factor of this synthesis is the easy sublimation of melamine.

Temperature	Related process
47°C	Melting point of cyanamide
137°C	Reaction of cyanamide into dicyandiamide
203°C	Melting point of dicyandiamide
234°C	Reaction of dicyandiamide into melamine
335°C	Sublimation of melamine
389°C	Formation of the cyameluric core, C_6N_7 out of melamine
525°C	Formation of the C_3N_4 network

Table 1.2: From cyanamide to g- C_3N_4

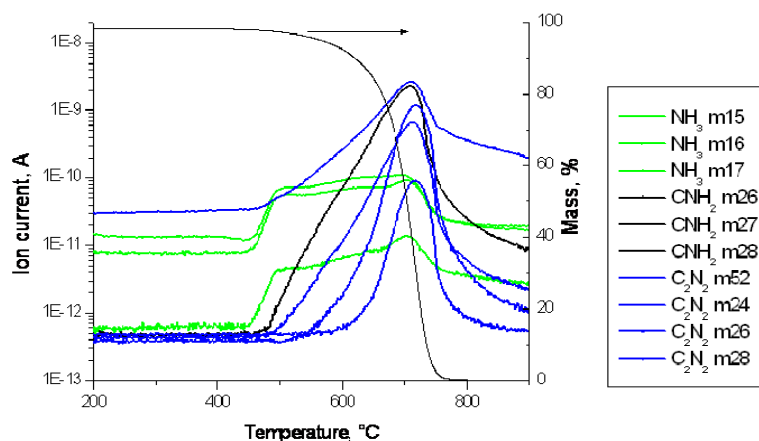


Figure 1.6: TGA-MS measurement under nitrogen of the decomposition of g- C_3N_4 .

The structural changes during the heating process can be followed by temperature dependent WAXS experiments, depicted in **Figure 1.7**. The strongest peak observed in the diffractogram of the 550°C heated compound at 27.3° is characteristic for interplanar stacking of aromatic systems and can be indexed as the (002) peak. This peak corresponds to a stacking distance of $d = 0.326$ nm. Compared to a carbon system with graphene units where the stacking distance is about 0.353 nm the stacking observed here is significantly tighter and is even 3% denser than the packing in crystalline graphite ($d=0.335$ nm).^[52] This higher packing density perpendicular to the layers is not surprising and well understood for aromatic systems with heteroatomic substitution. It can be attributed to the localization of electrons and stronger binding between

the layers. In addition a pronounced peak is observed at 13.1° , corresponding to a stacking distance $d = 0.675$ nm. This peak is typical for oriented melon materials.^[30, 31] Based on the electron microscopy evidence reported below, the 13.1° peak presumably relates to an in-plane structural packing motif, such as the hole-to-hole distance in a sheet. Indeed, the measured distance is only slightly below the size of one tri-s-triazine unit (~ 0.713 nm). **Figure 1.8** shows the FTIR spectrum of the polymeric- C_3N_4 heated at 550°C for 4 hours. Several strong bands in the $1200\text{-}1600\text{ cm}^{-1}$ region are found. They are typical for CN heterocycle stretching modes, which are also found in melamine and in melem.^[36] Additionally a strong vibration at 800 cm^{-1} is characteristic for the breathing modes of both triazine and tri-s-triazine units. Finally, the adsorption above 3000 cm^{-1} is related to residual amino groups in the material. XPS measurements confirm that the obtained material is build up from melem units connected through ternary amine bridges. An average C/N ratio of 0.71 is usually found by elemental analysis (theoretical value of C_3N_4 : 0.75). Small amounts of hydrogen (~ 2 wt%) from uncondensed amino groups and adsorbed water indicate the incomplete condensation.

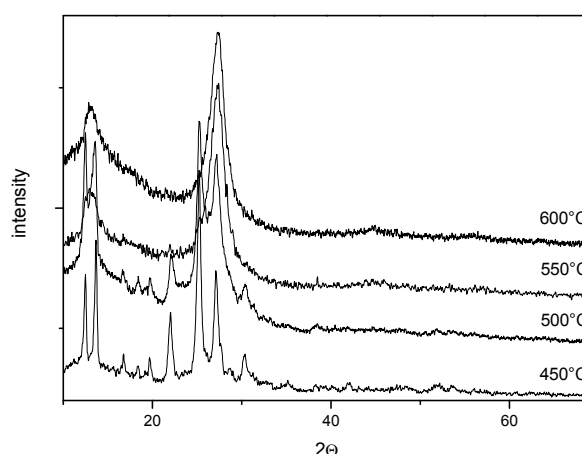


Figure 1.7: WAXS measurements characterising the transition from polymeric C_3N_4 to the so-called g- C_3N_4 . The reaction was stopped immediately after the listed temperature was reached.

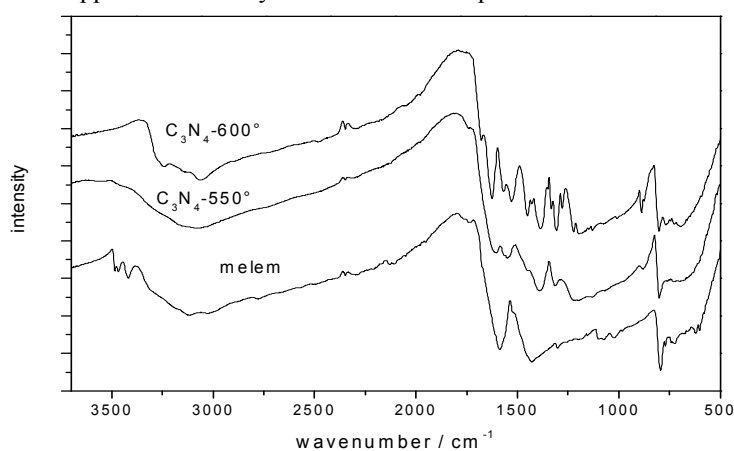


Figure 1.8: FTIR spectra of the synthesized materials at 550°C and at 600°C in comparison to the data of melem.

It was shown that it is very difficult to lower the hydrogen content by simple condensation beyond this limit, indicating that the final elimination step is most probably an endothermic process. Indeed the maximum temperature the material can be heated to without a depletion of the structure is 600°C, and this only in sealed quartz ampoules. A significant structural improvement of the material can still be obtained, as shown in **Figure 1.9**, when it is heated to 600°C for 10 hours in a sealed quartz ampoule. The interlayer organization becomes much better, indicated by the refinement of the (002) peak. This is accompanied by a compression of the average interlayer distance toward smaller d-values ($d = 0.319$). In addition, the in-plane peak becomes more defined, is weaker in relative intensity to the graphitic peak and has shifted to larger distances (from 0.675 nm to 0.689 nm). Also the stretching modes of the skeletal $\text{g-C}_3\text{N}_4$ network in the FTIR-spectrum are better resolved in the tempered material see **Figure 1.8**, probably due to a decoupling of the vibration modes by the better organization.

In order to investigate the local structure of the material on a nanometre scale, HRTEM measurements were performed in collaboration with Dr. J-O. Müller (Fritz Haber Institute, Inorganic chemistry department). While the material heated to 550°C is unstable and suffered a rapid structural decomposition in the intense electron beam, the 600°C tempered material is stable enough to allow for HRTEM and EELS measurements. The investigations were performed using the lowest possible beam intensity combined with short acquisition times for image recording. A representative overview of the material is given in **Figure 1.10**. Several crystallites with platelet-like morphologies in the size range of 500 nm are observable. At higher resolutions, (HRTEM, **Figure 1.12**) the graphitic like stacking of the material becomes visible and a stacking distance of $d = 0.327$ nm is measured, which is in close agreement with the XRD data.

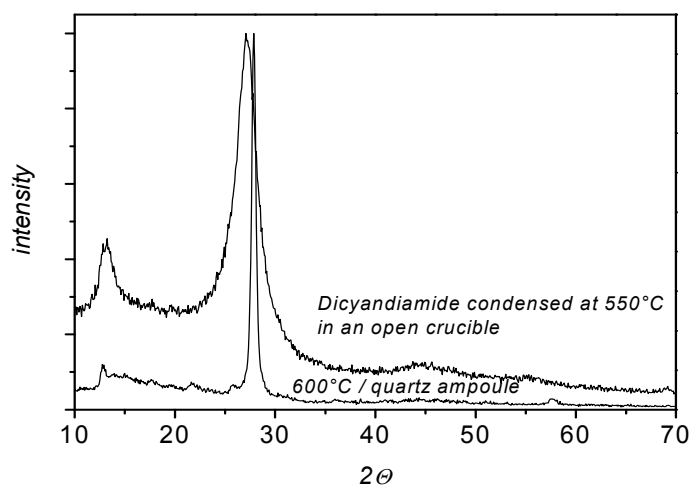


Figure 1.9: XRD patterns of the synthesized carbon nitride materials prior and after a structural optimization step at 600 °C.

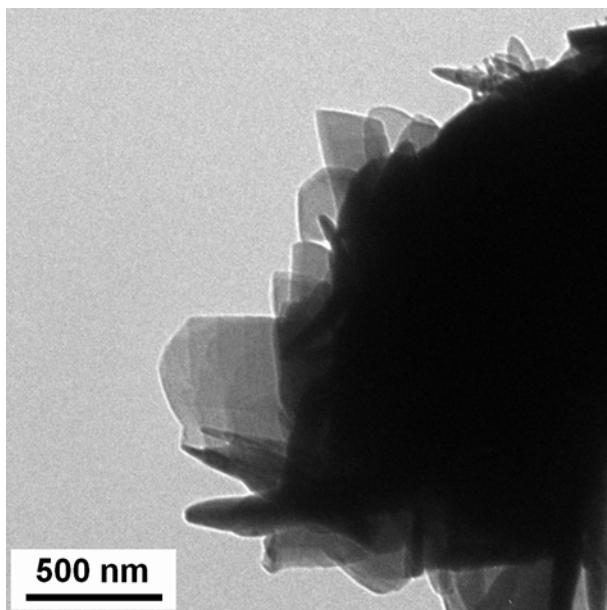


Figure 1.10: TEM micrograph of the crystallized $g\text{-C}_3\text{N}_4$. The morphology is layered, platelet-like.

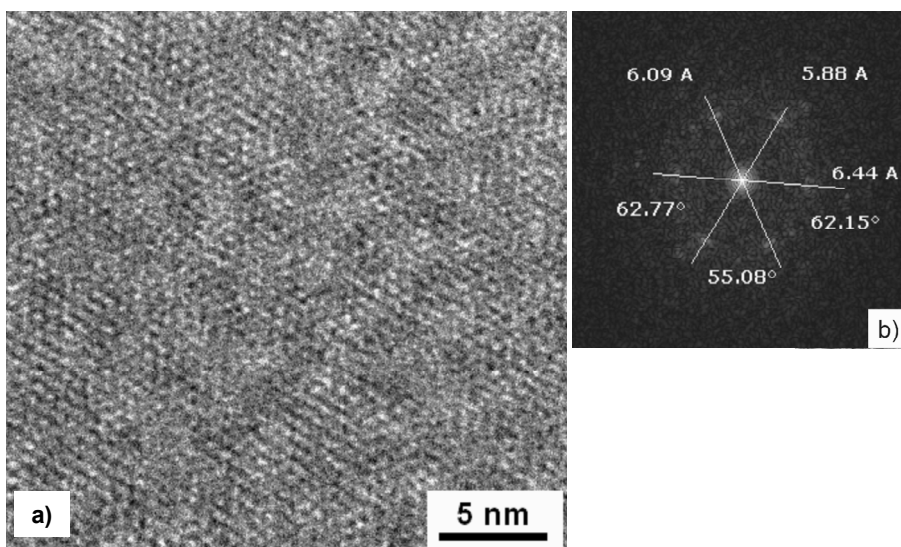


Figure 1.11: a) In plane organization of the condensed $g\text{-C}_3\text{N}_4$ material formed by tri-s-triazine units. b) The corresponding FFT of the micrograph underlines hexagonal symmetry.

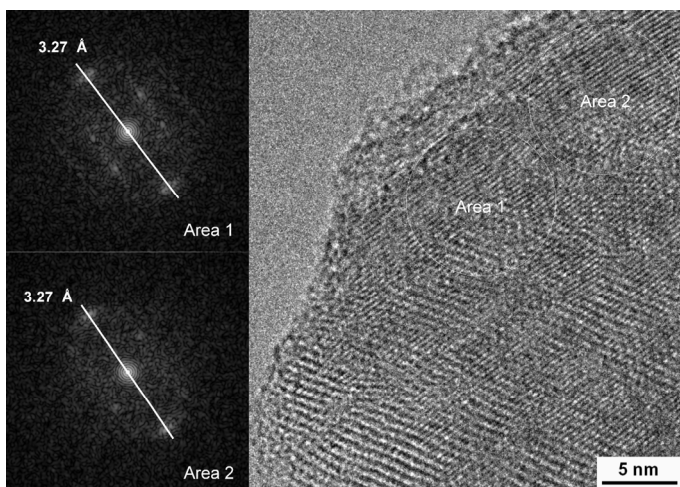


Figure 1.12: Graphite like stacking of the material visualized with HRTEM. The FFT of the circular areas 1 and 2 reveal an inter-planar distance of 0.327 nm and a periodicity orthogonal to the layer direction. Streaks due to stacking faults are visible.

It can be seen that the material is composed of domains, is rich in defects and the inter-layer spacing differs slightly from domain to domain (**Figure 1.12**). The micrograph in **Figure 1.11** indicates a close to hexagonal arrangement, which could correspond to the scaffolding tri-s-triazine structure. Apparent plane distances between 0.58 and 0.65 nm are measured and correspond with the in-plane peak measured from XRD. In fact, a perfect crystalline material consisting of tri-s-triazine units should reveal a six fold or threefold symmetry with distances of $d = 0.71$ nm. The recorded core-level EELS spectrum of the samples demonstrates that the material is almost exclusively composed of sp²-hybridized carbon and nitrogen atoms, as for both elements the $1s \rightarrow \pi^*$ transition is present. The carbon-K-ionization edge and the nitrogen-K-ionization edge show identical near edge structures, thus indicating that the carbon and the nitrogen are in a similar threefold coordination and electronic environment. In summary the material resulting from the high temperature ($T = 600^\circ\text{C}$) condensation of cyanamide is clearly a graphitic carbon nitride system. Evidence from XRD to HRTEM indicate that it is apparently composed of graphite-like stacks, which exhibits at least a close to hexagonal order within the layers. It can be concluded that thermal condensation of cyanamide represents an easy synthetic route to graphitic like carbon nitrides, which, as it will be shown in this work, can easily be combined with hard templating techniques to yield well defined g-C₃N₄ nanostructures.

The present work is divided into two main parts. The first part will focus on the synthesis of graphitic carbon nitride “reactive hard templates” and how control of the structure and morphology of g-C₃N₄ on a nanometre scale can be achieved through hard-templating procedures. It will be shown that the as-synthesised materials can act, beside their function as reactive templates, as metal free catalysts for the activation of benzene in Friedel-Crafts type reactions. The second part deals with the synthesis of nanostructured metal nitrides in and through the thermal decomposition of the previously mentioned graphitic carbon nitride nanostructures. The so synthesised metal nitrides were successfully applied as catalysts for aldol condensation reactions.

2 Characterisation methods

This chapter gives a brief introduction to the main analytical methods used in this work.

2.1 Nitrogen sorption

The physical parameters of porous materials are mainly their pore volume, their surface area and the size of the pores present. A powerful technique that is commonly used to characterise porous materials is gas sorption, mainly nitrogen sorption. In this method the sample to be analysed, the adsorbent, is cooled to a constant temperature, by immersing the measuring cell in a liquid nitrogen bath ($T_{\text{liquid N}_2} = 77 \text{ K}$). A known quantity of gas, the adsorbate, is then dosed into the measuring cell, during which time a certain quantity of the introduced gas becomes adsorbed at the surface of the sample. The plot of the adsorbed gas quantity as a function of the relative gas pressure p/p_o gives a typical adsorption isotherm. The following stepwise decrease of the pressure yield the desorption isotherm. The forces between molecules and a surface in general can be of two different types. On the one hand, molecules can bind through the formation of chemical bonds to the surface and chemisorption occurs, limiting the adsorption to a monolayer. However this process is characterized by high activation energies and occurs reversibly only at high temperatures. In the here described case, at temperatures below the critical temperature of the adsorbate only reversible physisorption takes place. The adsorbate gas molecules adsorb to the surface through weak Van der Waals forces resulting in a multilayer adsorption of the adsorbate molecules on the surface.

Different types of porous materials can be distinguished as illustrated by the IUPAC classification.^[53] The IUPAC differentiate between three classes of porous materials as a function of their pore size: micropores with a pore diameter (PD) less than 2 nm, mesopores with a PD between 2 and 50 nm and macropores with a PD bigger than 50 nm. The reason for this classification is that each size range of pores has a characteristic adsorption effect, which is reflected in the adsorption-desorption isotherm. There are six types of isotherms^[53] (**Figure 2.1**). Type I isotherms are characteristic for pure microporous materials with low external surface area. The micropores become filled at relatively low partial pressures ($p/p_o < 0.1$). Type II and type III isotherms describe the adsorption on macroporous or non porous adsorbents with strong and weak adsorbate-adsorbent interactions, respectively.

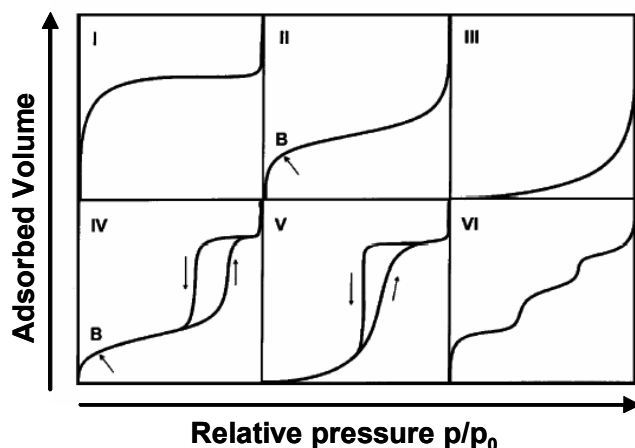


Figure 2.1: Classification of adsorption-desorption isotherms by the IUPAC.

The point B, highlighted with an arrow in **Figure 2.1**, represents the stage where the monolayer is completed and the multilayer formation begins. Type IV isotherms are characteristic for mesoporous materials. Their distinctive feature is the presence of a hysteresis loop, due to the capillary condensation of the gas in the mesopores. Different shapes of hysteresis loops are observed.^[53] The origin of the hysteresis is still under discussion however it is admitted that the different shapes of the hysteresis are related to different pore structures of the adsorbent in terms of shape, pore connectivity and cavitation, which are influencing the capillary condensation inside the mesopores. Type V isotherms are rarer and observed for mesoporous materials with weak adsorbate-adsorbent interactions. Finally type VI isotherms represent the stepwise adsorption of several layers on a non porous surface.

2.1.1 Determination of the surface area

Various mathematical models were developed to calculate key parameters of porous solids such as surface area and pore size distribution from the physisorption isotherms. The resulting values must be carefully interpreted due to the different approximations used in all sorption models. Concerning the determination of the surface area, the classical model used is the so called BET model, developed by *Brunauer, Emmet* and *Teller* in 1938.^[54] The BET theory is based on the kinetics of gas adsorption, originally described by *Langmuir*.^[55] He assumed that the surface of the solid consists of an arrangement of adsorption sites. Assuming that the system is in thermodynamic equilibrium, with equal adsorption and desorption rates of the gas molecules on the surface, and following the assumption that the adsorption is limited to a monolayer, the *Langmuir* equation is obtained:

$$\frac{n}{n_m} = \frac{B(p/p_o)}{1 + B(p/p_o)} \quad \text{with} \quad B = \frac{a_1 \kappa}{z_m \nu_1} e^{H_1/RT} \quad \text{Equ. 2.1}$$

Where n is the adsorbed gas quantity, n_m the monolayer capacity, p/p_o the relative pressure, κ the kinetic gas constant, a_1 the condensation coefficient, z_m the number of adsorption sites per surface unit, ν_1 the oscillation frequencies of the gas molecules perpendicular to the surface and H_1 the adsorption enthalpy. *Brunauer, Emmet and Teller* adopted the *Langmuir* mechanism, which lead to insolvable equations in the case of multilayer adsorption and simplified it by the following assumptions:

- 1) All adsorption sites for multilayer adsorption are of same energy in all the layers, except in the first one.
- 2) The adsorption heat (H_1) is equal to the molar condensation heat (H_L).
- 3) All layers after the first one show liquid-like properties.

With these assumptions the BET equation is obtained:

$$\frac{p/p_o}{n(1 - p/p_o)} = \frac{1}{n_m C} + \frac{C-1}{n_m C} (p/p_o) \quad \text{with} \quad C = e^{(H_1 - H_L)/RT} \quad \text{Equ. 2.2}$$

with n the total amount of adsorbed molecules and n_m the monolayer capacity. C is correlated with the adsorption- and condensation enthalpies, H_1 and H_L . By plotting the left side of the equation against p/p_o (usually in the range between $p/p_o = 0.1-0.3$) a straight line is observed. n_m and C can be derived from the ascending slope and the axis intercept, respectively. The specific surface area S can be calculated from n_m by assuming an average area σ that each adsorbed molecule occupies on the surface in a monolayer, through the simple equation:

$S = n_m \sigma N_A$, where N_A is the Avogadro constant. In addition to the previously mentioned assumptions, the exact value for σ is not accurately known and still under discussion. Usually, values for σ around 0.162 nm^2 are assumed for the adsorption of nitrogen. Furthermore, the presence of micropores can strongly affect the results obtained by the BET theory since the model does not take into account pore filling at low relative pressures.

2.1.2 Determination of the pore size of mesoporous materials

The classical models for the calculation of mesopore size distributions are based on the *Kelvin* equation. It expresses that due to the curvature of the pores, the saturation pressure above the

meniscus of the condensed gas is lowered. An analytical expression for this phenomenon is given by the following equation:

$$\ln \frac{p}{p_o} = -\frac{2\gamma v}{r_k RT} \quad \text{with} \quad r_k = r_m \cos \theta \quad \text{Equ. 2.3}$$

where r_k is the mean radius of curvature of the meniscus, γ is the surface tension and v the molar volume of the liquid condensed in the pores. The BJH model, developed by *Barrett, Joyner* and *Halenda*,^[56] uses a modified form of the *Kelvin* equation:

$$r_p(p/p_o) = \frac{2\gamma v}{RT \ln(p/p_o)} + t(p/p_o) \quad \text{Equ. 2.4}$$

Besides assuming the presence of cylindrical pores, the BJH model also assumes the formation of a physisorbed layer on the pore walls prior to the condensation. The thickness of the physisorbed film before condensation is t . However three main concerns question the validity of this formula: First, the exact relation between the meniscus curvature and the pore size, especially when the pore shape differs from cylindrical shape. Second the validity of the model for pores smaller than 4 nm and third the assumed constancy of the surface tension that probably varies with the pore diameter.

Finally, the total pore volume can be obtained by the amount of gas adsorbed at the plateau, provided that the condensate has the same density as the corresponding bulk liquid at the experimental temperature.

2.2 Electron microscopy (EM)

Electron microscopes are a class of imaging instruments that use a focused electron beam to examine objects at a very fine scale. Electron microscopy can give information about the structure and morphology of a sample as well as its composition and crystallinity.

Concerning microscopy in general, the resolution d (i.e. the ability to discriminate between two points) is given by the *Abbe* equation:

$$d = \frac{\lambda}{2n \sin \alpha} \quad \text{Equ. 2.5}$$

with λ the wavelength, n the refraction index of the medium and α the half aperture angle in radians. For light microscopes ($\lambda_{\text{vis}} > 400$ nm), this equation limits the resolution to ~ 300 nm. A much better resolution can be obtained by using electrons instead of visible light as imaging radiation. Indeed, *De Broglie* described moving particles as wave-like and their wavelength is

linked to their mass m , their velocity v and the Planck's constant h by the *De Broglie* equation as follows:

$$\lambda = \frac{h}{mv} \quad \text{Equ. 2.6}$$

For electrons in an electron microscope their velocity and hence their momentum depends on the accelerating voltage and is determined by equating the potential energy and the kinetic energy $eV = \frac{1}{2}mv^2$ which gives, combined with equation **Equ. 2.6** the following expression for λ :

$$\lambda = \frac{h}{\sqrt{2meV}} \approx \sqrt{\frac{1,5}{V}} \text{ (nm)} \quad \text{Equ. 2.7}$$

However this equation is only an approximation and requires a relativistic correction of the electron mass and velocity. For example electrons which are accelerated at a voltage of 120 kV have a wavelength of around 0.0035 nm, permitting to access higher resolutions.

The basic steps in EM (regardless the type) are:

- 1) Electrons are generated and accelerated toward the sample.
- 2) Magnetic lenses are used to focus the electron beam onto the sample.
- 3) The electron beam and the sample interact with each other.
- 4) The interactions are detected and transferred into an image.

The use of electrons instead of light as radiation source requires the use of magnetic lenses instead of optical ones, to guide and focus the electron beam. Each lens and aperture has its own set of aberration and distortions that determine the practical final obtained resolution.

The two major types of EM are on the one hand the scanning electron microscope (SEM) and on the other hand the transmission electron microscope (TEM). Both were used in this work to characterize the synthesized material on a nanometre scale in terms of topography and structure.

2.2.1 Scanning electron microscopy (SEM)

Scanning electron microscopy (SEM) uses the scattering of electrons from the sample's surface. The schematic presentation of an SEM set-up is presented in **Figure 2.2**. A beam of electrons is generated under vacuum inside the microscope. The beam is collimated by electromagnetic condenser lenses, focused by an objective lens into a spot of typically 1-5 nm in size and scanned, in a raster fashion, across the surface of the sample by electromagnetic

deflection coils. When the beam hits the surface of the sample, the electrons interact with its surface and if their energy is higher than the ionization potential of the elements constituting the surface, secondary electrons are emitted (SE). These electrons are relatively slow and are deflected from the sample by a weak electric field. The SE are selectively attracted towards the detector, through a grid held at a low positive potential. The electron detector counts the number of secondary electrons arriving per unit time and transfers this count rate into an electric signal. The final image is built up from the information of the number of electrons collected from each point of the sample. The release of SE by the sample is highly dependent of the surface geometry of the sample. Edges or convex surfaces within the sample facilitate the release of SE and appear brighter, since the brightness is related to the increasing number of counted electrons, while concave surfaces restrain the release of SE and appear darker. Through this mechanism the observed pictures appear spatial and rich in contrast leading to magnified images with structural and topographic details of the sample's surface. The yield of the SE also depends on the material. During the bombardment of the sample with electrons, charge is built on the surface, which in the case of non-conducting materials can not be dissipated. As a result the obtained image looks bright throughout the sample. That's why non-conductive materials have to be sputtered with a thin layer of conducting material (usually gold or gold/palladium alloys).

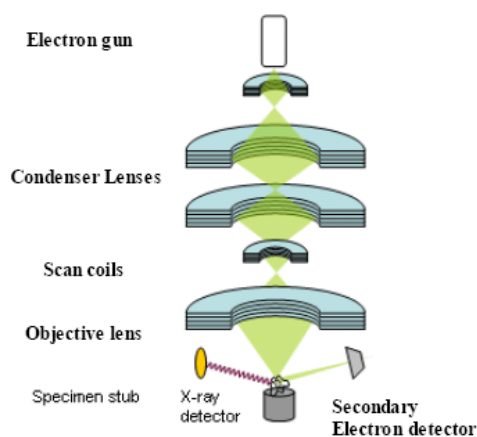


Figure 2.2: Schematic description of the optics of an SEM set-up.

The SEM can further be equipped with an energy dispersive X-ray spectrometer. **Energy dispersive X-ray spectroscopy** (EDS or EDX) is a technique widely used for chemical characterisation. Each element of the periodic table has a unique electronic structure and, thus, a unique response to electromagnetic waves. When the electrons of the beam interact with the elements constituting the sample, X-rays are created and their analysis allows the

determination of the elemental composition of the irradiated sample. When an atom of the sample is hit by the electron beam, an electron from an inner shell gets excited, leading to its ejection and resulting in the formation of an electron hole within the atom's electronic structure. This induces the relaxation toward the depopulated shell of an electron from an outer, higher-energy shell. The excess energy of that electron is released in the form of an X-ray. The release of X-rays creates spectral lines that are highly specific to individual elements and allows thus the elemental analysis of the sample. One inconvenient of this technique is that it is highly surface sensitive compared to the bulk volume of the material, which is related to the penetration depth of the electrons into the sample.

2.2.2 Transmission electron microscopy (TEM)

Compared to the scanning electron microscope, a higher resolution can be obtained with the transmission electron microscope. Here the electron beam passes through the sample and thus requires the preparation of very thin probes. The electron gun (electron source) is a heated cathode producing a stream of monochromatic electrons. Electrons are produced either by thermoionic emission using a heated filament (e.g. LaB₆) or in a field emission gun from a thin tungsten tip and accelerated towards an anode. First and second condenser lenses are then used to focus the electrons into a thin and coherent beam. When the beam reaches the sample, the electrons either pass the sample or may undergo several kinds of interactions with the material, namely absorption, diffraction and elastic or inelastic scattering. The instrument can be operated in two modes. In the image mode, the scattered electrons are suppressed by an aperture under the sample and the transmitted non affected portion of the beam passes the further lenses and is focused by the objective lens into an image. The visualisation of the image is a representation of the real space. Since the scattering processes occur when the electrons interact with the nuclei of the sample, heavy elements, with high Z values, therefore lead to higher scattering, which implies that fewer electrons are passing through the sample to reach the image plate. As a consequence the sample regions containing heavy elements appear dark. Conversely, regions containing lighter elements, such as organic compound, lead to limited scattering and appear much brighter. In general, the contrast is proportional to Z^2 . In the diffraction mode, the elastic scattered electrons are used to obtain selected area diffraction pattern (SAED) of the "illuminated" part of the sample and the observed diffraction pattern is a representation of the reciprocal space. The diffraction mode is used to investigate the crystalline structure on a nanometre scale of the observed sample. Besides the higher resolution obtained by TEM, the main advantage of the TEM, is the possibility to switch between the image mode and the diffraction mode. For example the image mode can be used to

visualise the morphology of nanoparticles, and the diffraction mode can then be used, just by removing the condenser aperture and introducing the selected area aperture, to investigate their crystal structure.

High resolution electron microscopy (HRTEM) allows the examination of structures even smaller than 1 Å such as the lattice fringes of nanocrystals. Those lattice fringes result from the formation of interference fringes between the scattered beam through crystal planes and the primary beam. TEM and HRTEM are major characterisation techniques in nanoscience and were widely used in this work to characterise the synthesised samples, in the case of nanostructured carbon nitrides, as well as for the nanostructured metal nitrides.

2.3 X-Ray Diffraction

X-ray diffraction is a technique based on the interaction of electromagnetic radiation with matter. X-rays are defined as short wavelength electromagnetic radiation (wavelength around 10^{-10} meter) produced by the deceleration of high-energy electrons or by electronic transitions involving electrons in the inner orbitals of atoms. The X-rays are produced in a vacuum X-ray tube that contains essentially two electrodes: an anode commonly made of copper, and as a cathode (electron source) usually a tungsten filament. By heating the cathode, electrons are emitted and accelerated with a high voltage till they collide with the anode. If the electrons are energetic enough, they are able to knock out an electron from the inner shell of the metal atom constituting the anode. As a result electrons from higher energy levels fill up the induced vacancy and X-ray photons are emitted. The spectral lines generated depend on the anode material and are called characteristic lines. Usually these are transitions from upper shells into K shell (called K lines), into L shell (called L lines) and so on. There is also a continuum “Bremsstrahlung” radiation given off by the electrons as they are scattered by the strong electric field near the high-Z (proton number) nuclei.

Three different types of scattering are emitted when matter is irradiated by X-rays: coherent (or elastic) scattering, *Compton* (or inelastic) scattering and fluorescence radiation. For *elastic scattering*, the outgoing X-rays have the same energy, so the same wavelength, as the incoming X-rays, only with altered direction. In contrast, *inelastic scattering* occurs when energy is transferred from the incoming X-ray to the crystal, e.g. by exciting an inner-shell electron to a higher energy level. Such inelastic scattering changes the wavelength of the outgoing beam, making it longer and less energetic. If the energy of the X-ray is higher than the ionisation potential of the bombarded atoms in the samples, fluorescence radiation can be produced, by the relaxation of a high energy electron into a lower energy state. This X-ray

fluorescence is used to perform chemical analysis. Only the coherent scattering is required for structural studies.

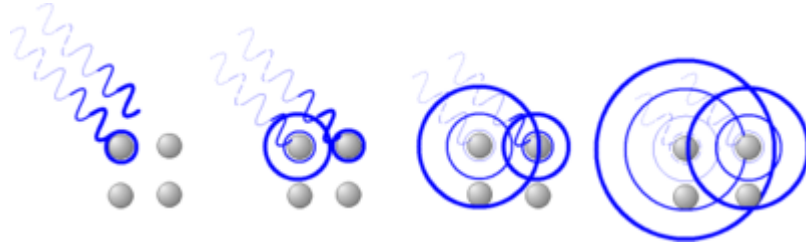
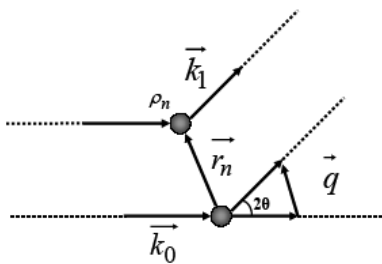


Figure 2.3: Formation of secondary waves

When an X-ray wave hits an atom, an interaction takes place with the electron shell of the atom. The electrons start to oscillate and create spherical waves, also called secondary waves (**Figure 2.3**). Therefore each atom in the crystal acts as a source for secondary X-rays. As a consequence the scattering amplitude $A(\vec{s})$ for the whole sample is a linear superposition of all scattering waves from each scattering center at the position \vec{r}_n and can be described:

$$A(\vec{s}) = \sum_{n=1}^N \rho_n \exp(2\pi \cdot i\vec{r}_n \cdot \vec{s}) \quad \text{Equ. 2.8}$$

where N is the number of scattering centers, ρ_n the scattering power and finally \vec{s} the scattering vector. \vec{s} is defined, for coherent scattering, as $\vec{s} = \frac{\vec{e} - \vec{e}_0}{\lambda}$. \vec{e} and \vec{e}_0 are the unit vectors of the incident and the scattered beam and λ the corresponding wavelength.



$$\vec{q} = \vec{k}_1 - \vec{k}_0 \quad \vec{q} = 2\pi \cdot \vec{s}$$

$$q = |\vec{q}| = \frac{4\pi}{\lambda} \sin(\theta) \quad \vec{k}_i = |\vec{k}_i| \cdot \vec{e}_i = \frac{2\pi}{\lambda} \cdot \vec{e}$$

Figure 2.4: Scattering from two scattering centres.

Real systems have a continuous electron density distribution $\rho(\vec{r})$ so that in the irradiated volume V the scattered amplitude $A(\vec{s})$ is related to $\rho(\vec{r})$ by a 3D Fourier transform F :

$$A(\vec{s}) = F(\rho(\vec{r})) = \int_V \rho(\vec{r}) \exp(2\pi \cdot i\vec{r} \cdot \vec{s}) dV \quad \text{Equ. 2.9}$$

However experimentally $A(\vec{s})$ is not directly accessible and only the scattered intensity $I(\vec{s})$ described in **Equ. 2.10**, which is the squared absolute value of the complex scattering amplitude, can be directly measured.

$$I(\vec{s}) = |A(\vec{s})|^2 = A^*(\vec{s}) \cdot A(\vec{s}) = \int_V P(\vec{r}) \exp(2\pi i \vec{r} \cdot \vec{s}) dV = F(P(\vec{r})) \quad \text{Equ. 2.10}$$

where $P(\vec{r})$ is an autocorrelation function, or the so called *Patterson* function. The scattering intensity and the *Patterson* function form a reciprocal pair of transforms, exactly as in the case of the scattering amplitude and the electron density distribution. The relations between the parameters in the real space and in the reciprocal space are shown in **Figure 2.5**.

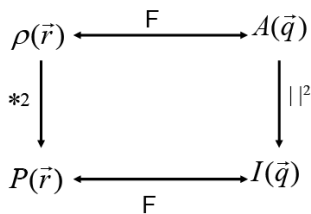


Figure 2.5: The relation between the parameters in the real (r) and in the reciprocal (q) space.

From the scattering intensity $I(\vec{s})$ in reciprocal space, it is not possible to know unambiguously the electron density distribution $\rho(\vec{r})$ in real space, because the information about the phase is lost. Therefore, each analysis of a scattering curve should only be a proposition and should be confirmed by other methods. During a typical scattering experiment, the scattering intensity $I(\vec{s})$ is measured as a function of the scattering angle 2θ . For crystalline systems, which are constructed by the infinite repetition of structural units in space, the *Braggs Law* applies. *William Lawrence Bragg* proposed a model in which the incoming X-rays are scattered specularly (mirror-like) from each plane. The planes are separated by the distance d . X-rays scattered from adjacent planes will combine constructively (constructive interference) when the angle θ between the plane and the X-ray results in a path-length difference that is an integer multiple n of the X-ray wavelength λ , resulting in the *Bragg equation* (**Equ. 2.11**). A reflection is said to be *indexed* when its Miller indices hkl (or, more correctly, its reciprocal lattice vector components) have been identified from the known wavelength and the scattering angle 2θ . Such indexing gives the unit-cell parameters, the lengths and angles of the unit-cell, as well as its space group. The line profiles of the so called *Bragg* reflections increases in width with decreasing size and increasing lattice imperfection.

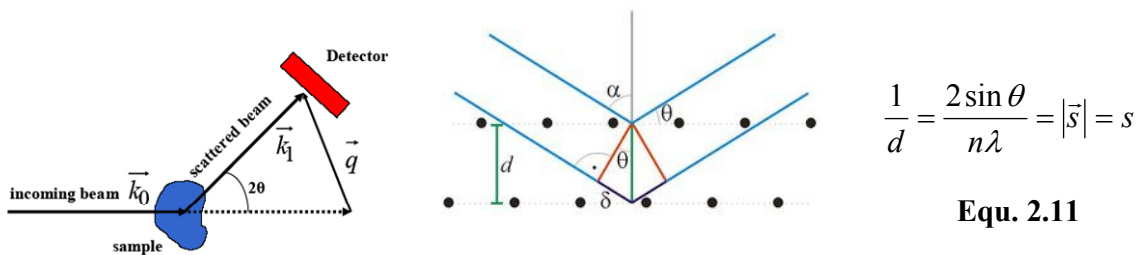


Figure 2.6: Schematically representation of the scattering set-up and of the Bragg Law.

Furthermore, the integral intensity of the lines decreases and the diffuse background increases so that an appropriate line separation becomes eventually impossible. An estimation of the crystallite sizes can be made according to the *Scherrer* equation (**Equ. 2.12**):

$$\Delta d = \frac{0.9\lambda}{B \cos \theta} \quad \text{Equ. 2.12}$$

where B is the measured full width at half minimum of a diffraction peak. The factor 0.9 is introduced for diffraction peaks, which can be described by a Gaussian function.

A result of the *Bragg* equation is that big structures are detected at small scattering vectors respectively scattering angles and smaller structures at higher angles. As a consequence, dependent of the dimension of the scattering angle, wide-angle x-ray scattering (WAXS) and small angle x-ray scattering (SAXS) are differentiated. As illustrated in **Figure 2.7** WAXS (typically at $2\theta > 5^\circ$) is used to investigate atomic structures, such as in crystallography, while SAXS (typically at $2\theta < 5^\circ$) is used to investigate structures in the colloidal dimensions (1-100 nm in size).

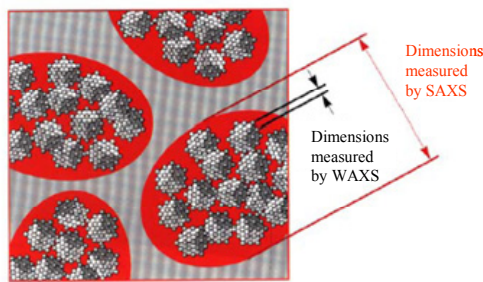


Figure 2.7: Schematic illustration of the dimensions of the scattering objects accessible with SAXS and WAXS.

In this work, in addition to WAXS for the characterisation of the crystalline structures, also SAXS was used for the characterisation of mesoporous graphitic carbon nitrides. An overview about the SAXS model used in this work, based on *Porod's* SAXS theory is given in the following.

Consider a two-phase system, with one phase called α , and the other β . If the electron density of each phase is constant but different from the electron density of the other phase, then, following the *Babinet's* Theorem, the scattering intensity $I(\vec{s})$ depends only on the difference in averaged electron density between the two phases ($\Delta\rho(\vec{r})$) as follows:

$$I(\vec{s}) \propto (\Delta\rho(\vec{r}))^2 \left| \int_V \Theta(\vec{r}) \exp(2\pi \cdot i\vec{s} \cdot \vec{r}) dV \right| \quad \text{Equ. 2.13}$$

$$\text{With } \Theta(\vec{r}) = \begin{cases} 1 & \alpha \text{ phase} \\ 0 & \beta \text{ phase} \end{cases}$$

The normalised *Patterson* function $\gamma(\vec{r})$, the so called “characteristic function” is one of the key functions concerning the SAXS theory and is defined as:

$$\gamma(\vec{r}) = \frac{P(\vec{r})}{P(0)} \quad \text{Equ. 2.14}$$

The scattering intensity at small angles can be described as the product of the *Porod* constant k and of the Fourier transform of the characteristic function $\gamma(\vec{r})$:

$$I(\vec{s}) = kF(\gamma(\vec{r})) = k \int_V \gamma(\vec{r}) \exp(2\pi \cdot i \cdot \vec{r} \cdot \vec{s}) dV \quad \text{Equ. 2.15}$$

In this formula the *Porod* constant k plays an important role, since it is connected to the volume fraction of each phase (ϕ_α, ϕ_β):

$$k = \int_V I(\vec{s}) dV = (\Delta\rho(\vec{r}))^2 V \phi_\alpha \phi_\beta \quad \text{Equ. 2.16}$$

Moreover, *Porod* showed that $\gamma(\vec{r})$ is directly connected to the existing interface S/V between the two phases, through the relation:

$$\gamma(\vec{r}) = \gamma(r) = 1 - \frac{|\vec{r}|S}{4\phi_\alpha\phi_\beta V} + \dots = 1 - \frac{r}{l_p} + \dots \quad \text{Equ. 2.17}$$

Where l_p is the *Porod* length defined as:

$$l_p = \frac{4\phi(1-\phi)V}{S} \quad \text{Equ. 2.18}$$

ϕ is the volume fraction of one of the two phases of the system. For porous systems, ϕ represents the volume fraction of pores in the system, in other words the porosity. The *Porod length* also gives information about the average segmental length of each phase (**Figure 2.**).

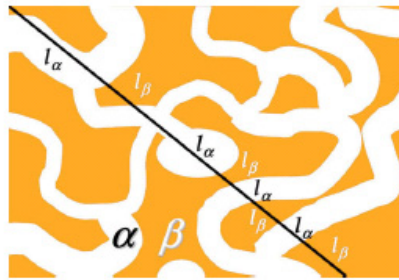


Figure 2.8: Schematic representation of an unordered 2 phase system.

So that information about the pore size of a system, independent of pore shape and morphology can be obtained through the following equation:

$$\frac{1}{l_p} = \frac{1}{\langle l_\alpha \rangle} + \frac{1}{\langle l_\beta \rangle} = \frac{1}{\langle l_\alpha \rangle \phi_\beta} = \frac{1}{\langle l_\beta \rangle \phi_\alpha} \quad \text{Equ. 2.19}$$

Moreover the scattered intensity of a two phase system with sharp interfaces has a characteristic behaviour at high scattering vectors s given by the *Porod*-Asymptote:

$$\lim_{s \rightarrow \infty} s^4 I(s) = \frac{k}{2\pi \cdot l_p} \quad \text{Equ. 2.20}$$

This implies that the scattered intensity decreases with s^{-4} at high scattering vectors. Through this it is possible to estimate numerically the *Porod* length with the following equation:

$$l_p = \frac{4\pi \int_{s=0}^{\infty} s^2 I(s) ds}{2\pi^3 \lim_{s \rightarrow \infty} s^4 I(s)} \quad \text{Equ. 2.21}$$

If the system to be investigated contains scattering units with a defined geometry, such as spheres, cylinders or plates, it is possible to fit the scattering curve with a defined “form factor” $F(s)$. Furthermore if a long range order exists between these scattering elements, this can be considered through the incorporation of a “lattice factor” $S(s)$. In this case: $I(s) \propto F^2(\vec{s})S^2(\vec{s})$. This gives information about the interactions between the scattering entities, about their size and their polydispersity.

3 Experimental Section

3.1 Synthesis of nanostructured graphitic carbon nitrides

3.1.1 Synthesis of mesoporous graphitic carbon nitrides (mpg-C₃N₄)

3.1.1.1 Synthesis of mesoporous g-C₃N₄ with 12 nm pores: mpg-C₃N₄-x-LHS40

Cyanamide (CH₂N₂, Aldrich) was used as a molecular precursor for g-C₃N₄. To 1 g cyanamide (24 mmol), different amounts of a 40% water dispersion of 12 nm SiO₂ spheres (Ludox HS40, Aldrich) were added drop wise under stirring and sonication (1.25 g, 2.0 g and 4.0 g Ludox for the corresponding x values 0.5, 1 and 1.6 with $x = m_{\text{silica}} / m_{\text{cyanamide}}$). The resulting transparent mixtures were then heated under vigorous stirring to 100°C to slowly evaporate the water. A white solid composed of dicyandiamide and silica is obtained, which is subsequently heated in a covered ceramic crucible to 550°C for 4 hours with a heating ramp of 2.2°C min⁻¹. The resulting brown-yellow powders were treated with a 4 M solution of NH₄HF₂ for two days in order to remove the silica template (50 mL of etching solution for 1g powder). The collected powders were washed 1-2 days in distilled water (100 mL for 1g powder) and several hours in ethanol. Finally the powders were dried at 70°C under vacuum. Typically for 1g cyanamide used, 280 mg of mesoporous g-C₃N₄ is obtained, which corresponds to a weight yield of 28%.

3.1.1.2 Synthesis of mesoporous g-C₃N₄ with 23 nm pores: mpg-C₃N₄-x-LTMA

For the synthesis of the mpg-C₃N₄-x-LTMA powders the same procedure as for the mpg-C₃N₄-x-LHS40 was applied, except that a 35% water dispersion of 23 nm SiO₂ spherical colloids (Ludox TMA, Aldrich) was used as template. For 1 g cyanamide the LTMA amount was varied from 1.5 g, 2.3 g, 3.2 g to 4.1 g for the corresponding x values 0.5, 0.8, 1.1 and 1.4 with $x = m_{\text{silica}} / m_{\text{cyanamide}}$.

3.1.1.3 Catalytic tests with mpg-C₃N₄-LHS40

Friedel-Crafts alkylation

25 mg of mpg-C₃N₄-1-LHS40 (0.5 mmol of melem units) were suspended in a solution of benzene (150 mg, 2 mmol) and hexanoyl chloride (50 mg, 0.75 mmol) in the respective solvent (heptane, anisole, benzene). The mixture was heated to reflux. After 20 hours of reaction, an aliquot of the mixture was poured into ethanol and analysed by GC. The structure of the product was confirmed by ¹H NMR.

Friedel-Crafts alkylation

50 mg of mpg-C₃N₄-1-LHS40 were placed in a 40 mL autoclave, fitted with a Teflon cup, to avoid any metal contamination. Since the previous experiments concerning the Friedel-Crafts acylation of benzene with hexanoyl chloride have shown that the solvent could dramatically affect the efficiency of the catalyst, two series of catalytic tests were performed. In the first one, the solution added to the catalyst in the autoclave contained 5 mL of the electrophile and 200 mg of benzene. This was the case when the used electrophile is an alcohol (methanol, ethanol, isopropanol). In the second one, the solution consisted in 5 mL of benzene and 200 mg of the desired electrophile (formic acid, tetra methyl ammonium bromide). The sealed autoclave was heated to 150°C for 24 hours. The products of the reaction were analysed and quantified by GC and the products attribution was ascertained by ¹H NMR. The conversion rates were calculated on the amount of obtained product compared to the initial amount of limiting reactant.

3.1.2 Synthesis of macroporous graphitic carbon nitrides

3.1.2.1 Synthesis of 60 nm silica nanoparticles (ST-60)

The silica nanoparticle were synthesised with a slight modification of the approach described by Johnson *et al.*^[57] A microemulsion was prepared by rapidly stirring 150 mL of cyclohexane, 6 mL of n-hexanol, 19 mL of Triton NP-9, 7 mL of water and 1.7 mL of 28% aqueous ammonia. To this solution 10 mL of tetraethylorthosilicate (TEOS) was added. The mixture was stirred at ambient temperature for 2 days. Most of the solvent was removed by rotary evaporation. The obtained viscous gel was then calcined at 200 °C for 2 hours, at 350 °C for 3 hours and at 550 °C for 5 hours. A white powder composed of highly monodispersed silica particles, with a diameter of 60-65 nm was obtained.

3.1.2.2 Synthesis of macroporous graphitic carbon nitride with 60 nm pores (CN-60)

The 60 nm silica particles (ST60), described in section 3.1.2.1, were pressed into a pellet and annealed at 800°C for 5 hours. The cooled pellet was infiltrated with molten cyanamide. To achieve a perfect infiltration of the pellet with the carbon nitride precursor, the pellet was placed in a 40°C tempered vacuum oven for 10 minutes. The infiltrated pellet was then placed in a covered crucible and heated to 550°C for 5 hours with a heating ramp of 2.2°C min⁻¹. To remove the silica template, the resulting yellow pellet, was shaken in a 4M NH₄HF₂ for 2 days. The powder was collected by centrifugation, redispersed and shaken in distilled water for two

days to be finally washed with ethanol. After the drying in a vacuum oven at 70°C (overnight), a macroporous yellow powder was obtained.

3.1.2.3 Synthesis of macroporous graphitic carbon nitride with 500 nm pores (CN-500)

The 500 nm silica spheres M500 were kindly provided by Merck. 1 g of M500 was dispersed in 5 g of molten cyanamide by high power sonication and calcined at 550°C for 4 hours, with a heating ramp of 2.2°C min⁻¹. The resulting yellow powder was then treated with NH₄HF₂, water and ethanol as described for the sample CN-60.

3.1.3 Synthesis of bimodal graphitic carbon nitride (bmg-C₃N₄)

Bimodal graphitic carbon nitride was prepared by combining two types of silica nanoparticles. Commercial LHS40 (Ludox HS40, 12 nm silica spheres dispersed in water 40 wt%, Aldrich) were employed to create mesopores and 500 nm Monospheres (M500) provided by Merck were used to create macropores in the material. 1g of M500 was mixed with LHS-40 in quantities varying from 1g to 3g. The template mixture was sonicated twice with a high power sonication micro-tip for 30 seconds, prior the addition of 5 g molten cyanamide. The mixture was stirred and sonicated again to reach a good dispersion of the template in the cyanamide. The cooled pasty mixture was placed in a covered crucible and calcined at 550°C for 4 hours with a heating ramp of 2.2°C min⁻¹. A yellow orange powder was obtained. The removal of the template was made by following the procedure applied for the synthesis of the mpg-C₃N₄-x-LHS40 samples.

3.1.4 Synthesis of graphitic carbon nitrides nanorods and nanotubes

For the synthesis of graphitic C₃N₄ nanorods, commercially available aluminium oxide membranes (Anodisc, Whatman, pore size 0,2 µm) were used as template. The membranes were infiltrated with molten cyanamide and placed under vacuum for several minutes. The excess of cyanamide was subsequently removed by rinsing the membrane with distilled water. The membranes were let to dry, placed between two petri dishes and calcined at 550 °C for 4 hours under nitrogen flow (heating ramp: 2.2°C min⁻¹). To remove the aluminium oxide, the g-C₃N₄ loaded membrane was treated with concentrated phosphoric acid for 2 days. The rods were then centrifuged and extensively washed with distilled water and ethanol before being dried for one day at 70°C.

The same procedure was applied for the synthesis of graphitic C_3N_4 nanotubes. The only difference was that an aqueous cyanamide solution (1.7 mol.L^{-1}) was employed to infiltrate the alumina membranes.

3.1.5 Synthesis of graphitic carbon nitride coatings on mesoporous silica microspheres

3.1.5.1 Amine functionalisation of mesoporous silica microspheres: Si100-N

The silica microspheres from Merck were amine functionalised by post-synthetic grafting. 160 mL (1 mmol) of APTES (3- Aminopropyltriethoxysilan, Aldrich) was added to 1 g of silica spheres in 100 mL of anhydrous toluene under nitrogen atmosphere. The mixture was stirred over night at room-temperature and the functionalised powder was collected by suction filtration, washed with 1L deionised water and air-dried.

3.1.5.2 Synthesis of g- C_3N_4 coatings on Si100 and Si100-N supports

Mesoporous silica microspheres from Merck (Lichrospheres Si 100 (Si100), 5 μm in diameter, pore size 9 nm) were used as support material for g- C_3N_4 coatings. The Si100 silica spheres were infiltrated with aqueous cyanamide solutions of different concentrations (1 g cyanamide in 1 g, 2 g and 4 g water respectively). The infiltrated powders were collected by centrifugation. The wet powders were placed in covered crucibles and calcined at 550°C for 4 hours with a heating ramp of $2.2^\circ\text{C min}^{-1}$ under nitrogen flow, to avoid the sublimation of melamine during the condensation reaction. Yellow to light yellow samples were obtained. For the coating of the amine pre-functionalised powders, brown ochre to light brown ochre powders were obtained.

3.2 Synthesis of nanostructured metal nitrides

3.2.1 Synthesis of metal nitride nanoparticles in mpg- C_3N_4

In a general synthesis 2.5 g (denoted as “concentrated”) or 1.5 g (“diluted”) of the metal precursor was dissolved in 2.0 g of ethanol. Caution is advised because the described metal precursors (GaCl_3 , VOCl_3 and TiCl_4) react vigorously with ethanol. To this solution 500 mg of mesoporous C_3N_4 [mpg- C_3N_4 -1-LHS40] was added. After 10 minutes under stirring and sonication complete penetration of the solutions into the mesoporous framework was assumed. To be sure, the mixture was additionally placed several minutes under vacuum, to eventually free pores from air bubbles. The infiltrated mesoporous C_3N_4 was collected by suction

filtration and washed twice on the filter with 2 mL of ethanol. The resulting powder was heated in 4 hours to 800°C and kept at this temperature for 3 hours under nitrogen flow. It should be explicitly noted that the oven has to be cooled down to room temperature before the samples are taken out, as they are sensitive to oxidation in air even at slightly elevated temperatures. However, after being properly removed from the oven, the samples are stable and do not need to be stored or manipulated under inert gas. This procedure is applied to all further nitride syntheses.

3.2.2 Synthesis of ternary metal nitride alloy nanoparticle $A_xB_{(1-x)}N$

In a general synthesis, x mol of precursor A and (1-x) mol of precursor B were dissolved in 2g of ethanol.

AlGaN	AlCl ₃ [mg]	GaCl ₃ [mg]	EtOH [g]	Al/Ga mol. ratio
AF117-0.16	110	730	2	0.20
AF117-0.35	290	530	2	0.72
AF117-0.59	397	360	2	1.46
TiVN	VOCl ₃ [mg]	TiCl ₄ [mg]	EtOH [g]	V/Ti mol. ratio
AF154-0.16	170	1000	2	0.19
AF154-0.35	400	800	2	0.55
AF154-0.59	800	600	2	1.46

Caution is advised because the described metal precursors (GaCl₃, AlCl₃, TiCl₄, VOCl₃) react vigorously with ethanol. To these transparent solutions mesoporous C₃N₄ [mpg-C₃N₄-1-LHS40] was added. The mixture was sonicated for 10 minutes and placed under vacuum, to free the pores from air and to achieve a good penetration of the solution inside the pores. The infiltrated mesoporous powder was collected by suction filtration and dried on the filter. The resulting powder was heated up to 800°C under nitrogen flow in 4 hours and kept there for 3 hours. After the heat-treatment, depending of the synthesized alloy, grey powders for the AlGaN system and black powders for the TiVN system were obtained.

3.2.3 Synthesis of a macroporous titanium nitride/carbon composite

3.2.3.1 Synthesis of porous titanium nitride/carbon nanocomposite with 60 nm pores (TN-60)

The porous carbon nitride powder (PCN60) was infiltrated with a titanium tetrachloride/ethanol solution with the mass ratio: TiCl₄/EtOH = 2.3 g / 5 g. The infiltrated powder was filtrated and aged at 100°C for one night. Finally the aged powder was heated in a closed crucible under nitrogen flow to 800°C for 3 hours with a heating ramp of 194°C /min.

When the oven is totally cooled down to room temperature, the samples are removed from the oven.

3.2.3.2 Synthesis of titanium nitride hollow spheres

The same procedure as for the synthesis of the sample TN-60 was employed. In this case the macroporous sample CN-500 was used as reactive template.

3.2.4 Synthesis of mesoporous titanium nitride from mesoporous anatase

3.2.4.1 Synthesis of bulk mesoporous titanium oxide

All chemicals were used as received. The mesoporous TiO₂ was prepared according to Wang and co-workers by the following hydrolysis condensation method using tetrabutyl orthotitanate (TBOT, Aldrich) as a metal precursor and Triton X-100 (TX-100, 4-(C₈H₁₇)C₆H₄(OCH₂CH₂)_nOH, n~10, Aldrich) as the structuring agent. In a typical procedure TBOT (6.80 g = 19.98 mmol) and TX-100 (6.46 g = 10.00 mmol) were mixed with absolute ethanol (38.00 g = 0.825 mol) under vigorous stirring. Then water (168.00 g = 9.33 mol) was added drop wise under continuous stirring, which induced the immediate precipitation of a white solid. The molar composition of the reaction mixture was: TBOT: TX-100: EtOH: H₂O ~2:1:82.5:933. The mixture was aged at room temperature for 24h and at 80°C for another 24h without stirring. The supernatant solution was removed and the solid isolated by centrifugation. The obtained white powder was washed twice with first 40 mL of water and then 40 mL of EtOH. Finally the powder was dried overnight under vacuum at 100°C.

3.2.4.2 Synthesis of the mesoporous titanium nitride

The mesoporous Titanium nitride powders were prepared by using the above described mesoporous TiO₂ powder and cyanamide (CA, NH₂CN, Aldrich) as nitrogen source. In a typical synthesis, 100 mg of the TiO₂ powder were mixed with a given amount of molten CA for the high amounts or CA dissolved in 0.5 mL of water for the small amounts in a covered crucible, in order to penetrate the porous network of the TiO₂. The amount of CA was varied in order to vary the CA/TiO₂ mass ratio x from $x = 2$ to 14. The covered crucible was then heated to 800°C under nitrogen for 3 h with a heating ramp of 3.3 K/min, in a chamber kiln from Nabertherm GmbH. The resulting powders were labelled P- x . Attention is recommended as high surface area TiN proved to be very pyrophoric! The oven has to be totally cooled down ($T < 40^\circ\text{C}$) before removing the samples

3.2.4.3 Catalytic tests with TiN

As the aim was to access cheap and easy to handle catalysts, the obtained powders were neither stored nor handled under inert gas. The used chemicals were employed as received and the solvents were not further purified. More over the scaling up of the synthesis of mesoporous TiN (in order to be able to run a large number of catalytic tests) proved easier with the procedure with the highest initial cyanamide/TiO₂ ratio. We thus used the powders resulting from this synthesis (P-14) as a catalyst even if they featured a large amount of residual carbon as discussed in **section 5.4.1**. As preliminary tests, the activity of our TiN powder was tested in aldol condensation and further compared to the activity of mesoporous TiO₂ in the alkylation of ketones with alcohols.

Aldol condensation

In a typical reaction, 50 mg of mesoporous TiN (P-14) were weighted in a SCHOTT screw capped glass tube (160 mm length, about 10 mm inside diameter). The wanted amount of the pure ketone or alternatively a 2 ml xylene solution of ketone and aldehyde was added. The tube was closed and heated to 150°C for 48h. The products were analyzed and quantified by GC-MS (Agilent Technologies, GC 6890N, MS 5975).

Alkylation reactions

In a typical reaction 50 mg of titanium dioxide or nitride were weighted in a similar screw capped glass tube (160 mm length, about 10 mm inside diameter). 2 ml of a solution of 1 mmol of ketone and 1 mmol of alcohol in xylene were added. The tube was closed and heated to 150°C in an oil bath (only 20 mm of the tube were in contact with the oil) without stirring. The products of the reaction were analyzed by GC-MS (Agilent Technologies, GC 6890N, MS 5975) and ¹H NMR (Bruker DMX 400).

4 Synthesis and characterisation of nanostructured graphitic carbon nitrides

Graphitic carbon nitride is a potentially useful substitute for amorphous or graphitic carbon in a variety of applications, for example, as a catalytic support and for gas storage. Therefore, in addition to the big effort concerning the synthesis of bulk graphitic C_3N_4 (g- C_3N_4), new synthesis strategies for nanostructured carbon nitrides are of high interest.^[58-60] There are already some attempts to synthesise nanostructured g- C_3N_4 reported in the literature. Vinu *et al.*^[58] recently reported the synthesis of mesoporous carbon nitride materials by nanocasting. They used SBA-15 and SBA-16 as an exotemplate and succeeded in obtaining highly ordered mesoporous carbon nitride powders with high surface areas, via a polymerization/carbonisation process of ethylenediamine with carbon tetrachloride. However the C/N ratio of the as prepared material was around 5 and indicated the loss of the vast majority of the nitrogen, while the X-Ray diffraction pattern showed only poor crystallinity of the pore walls. Groenewolt *et al.*,^[61] who developed the presented bulk synthesis of g- C_3N_4 (see introduction, section 1.3), developed the synthesis of well defined and crystalline g- C_3N_4 nanoparticles by infiltrating mesoporous silica host matrixes with spherical pores with molten cyanamide as molecular precursor, showing that hard templating is the technique of choice to form nanostructured g- C_3N_4 . The C/N ratio of the obtained particles was close to 0.64 versus 0.71 for the bulk material, pointing toward a larger amount of uncondensed amino functions. This was attributed to an increased number of terminating amine functions due to the materials nanoscale. Furthermore a highly developed graphitic stacking as for the bulk material was observed. The control over the particle size was easily controlled by the pore size of the silica host matrix. Thus pores of 50-70 nm in size yielded particles of 50-70 nm in diameter, while the use of smaller pores yielded smaller particles. This chapter focuses on the synthesis of carbon nitride nanostructures, based on the combination of the thermal condensation of cyanamide inside (exotemplate) or around (endotemplate) different kind of hard templates.

4.1 Synthesis of mesoporous graphitic carbon nitride (mpg- C_3N_4)

4.1.1 The template

Mesoporous materials in general, are materials with pore sizes in the range of 2-50 nm, as defined by the IUPAC. Since the synthesis of graphitic carbon nitrides (g- C_3N_4) is a high temperature procedure (see introduction, section 1.3), occurring at temperatures higher than

400°C, appropriate templates that withstand 600°C for at least 12 hours were needed. This is given by hard templates, e.g. inorganic nanostructures, which can be removed by etching. Silica nanostructures can be synthesised in highly controlled fashion or are even commercially available and thus are widely used for hard templating synthetic approaches. For the synthesis of mesoporous graphitic carbon nitrides (mpg-C₃N₄) commercial aqueous colloidal silica suspensions were used as templates (LUDOX, Aldrich). Two types of Ludox templates with different particle sizes were used to vary the pore size of the resulting material. First Ludox HS-40 (LHS40), which is a 40 weight % silica colloidal water dispersion with colloids of a mean size of 12 nm (**Figure 4.1**) and Ludox TMA (LTMA), which is a 35 weight % silica colloidal water dispersion with colloids of a mean size of 23 nm (**Figure 4.2**).

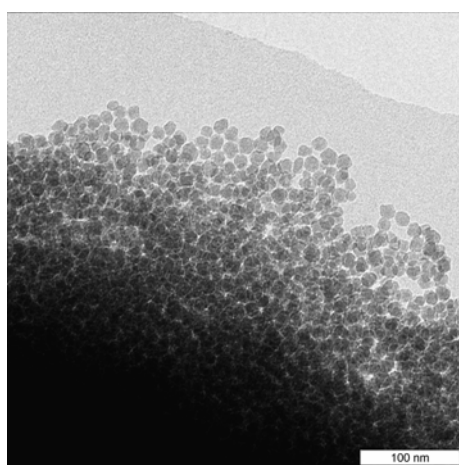


Figure 4.1: TEM image of LHS-40

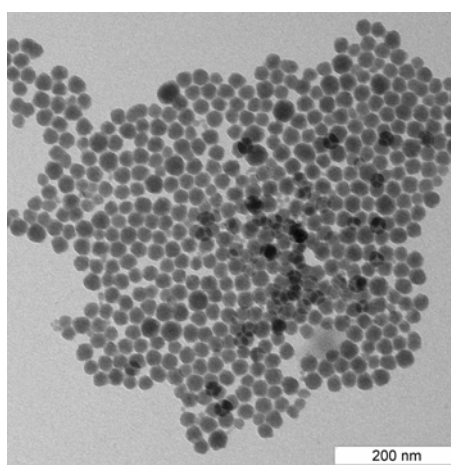


Figure 4.2: TEM image of LTMA

4.1.2 The synthetic strategy

As shown before (introduction, section 1.3), the synthesis of the graphitic carbon nitride network, g-C₃N₄, is based on the thermal condensation of cyanamide (NH₂CN), dicyandiamide or melamine. For the synthesis of nanostructured graphitic carbon nitrides, cyanamide was chosen as precursor instead of dicyandiamide or melamine for two practical reasons: First of all cyanamide is highly water soluble (775 g/L at 15°C), so perfectly compatible with the aqueous LUDOX template dispersion. Thus organic polar solvents, as DMF, could be avoided, as these solvents would destabilise the colloidal silica suspensions, leading to aggregation or even gelation of the template. Second, cyanamide has a low melting point ($T_m = 42^\circ\text{C}$) and thus dry templates can be easily infiltrated with the melt. In the particular case of the synthesis of mesoporous graphitic C₃N₄ powders (mpg-C₃N₄), the cyanamide was directly mixed with different amounts of aqueous dispersion of the template (LUDOX HS40, Aldrich, denoted as LHS-40) under vigorous stirring and sonication at 40°C until the cyanamide was fully dissolved. After the mixture was heated under stirring to 100°C, evaporation of the water

occurs, resulting in the formation of a white solid. The obtained white solid is a mixture of dicyandiamide and silica nanoparticles, as shown by X-Ray diffraction measurements (XRD) and FT-IR spectroscopy (**Figure 4.3**). Thus the first condensation step from cyanamide to dicyandiamide had already occurred at 100°C, whereas in the absence of silica colloids, this first condensation step takes place at slightly higher temperatures (at 137°C, see introduction, **Table 1.2**). The heat treatment at 100°C allowed to remove slowly the water and to trap the silica colloids in a solid matrix of dicyandiamide thus avoiding organic/inorganic phase separation. Indeed, during further heat treatment at 550°C, which induces the condensation under release of ammonia into the g-C₃N₄ network, the dicyandiamide does not melt but reacts directly in the solid phase into melamine, melem, melon and finally results in the graphitic carbon nitride, as already mentioned in the introduction. XRD and FT-IR measurements (**Figure 4.4**) reveal that the thermal condensation of the dicyandiamide in the composite occurs similar as observed in the bulk material (see introduction). The final composite at 550°C exhibits, despite the broad amorphous silica background around $2\theta = 20^\circ$, the graphitic interlayer stacking (peak at 27.3°) and the intralayer packing features (peak at 13.1°) of g-C₃N₄. The FT-IR spectrum of the composite reveals also the characteristic bands observed for the bulk g-C₃N₄, whereas the composite heated to 300°C exhibited the typical vibrations of a melamine like compound (bands between 2200-2100 cm⁻¹, corresponding to the vibrations of nitriles – C \equiv N, have disappeared, band at 815 cm⁻¹, corresponding to the triazine breathing modes is formed).

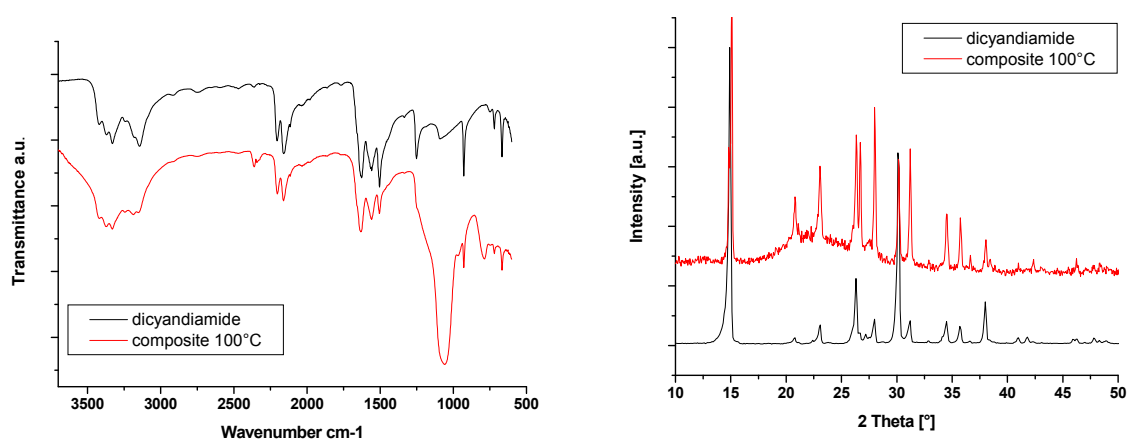


Figure 4.3: IR spectrogram (left) and X Ray diffractogram (right) of dicyandiamide and of the white solid obtained after the water evaporation at 100°C.

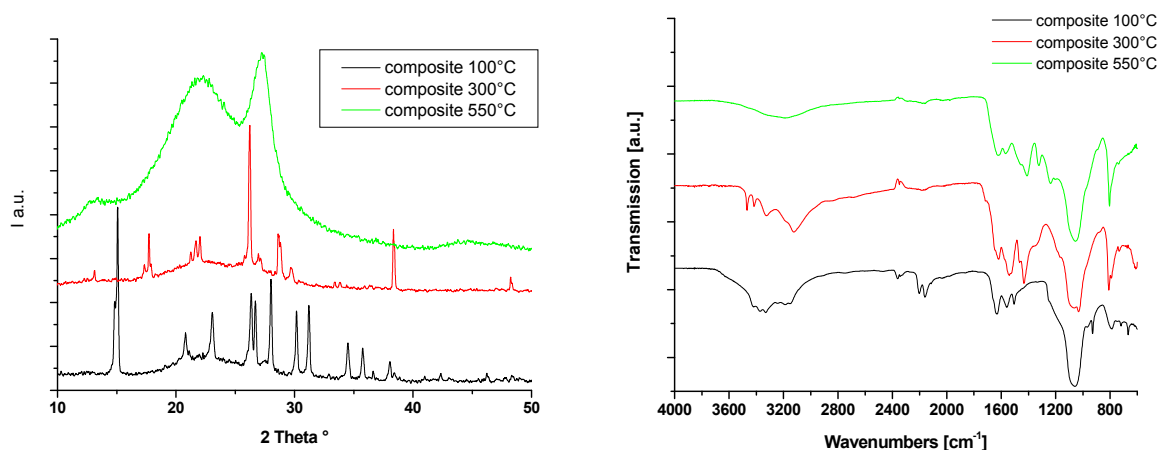


Figure 4.4: X-ray diffraction pattern (left) and FT-IR spectrograms (right) of the dicyandiamide/silica white solid heated at different temperatures during the thermal condensation of the g- C₃N₄ network.

4.1.3 The removal of the template

To obtain the mesoporous graphitic C₃N₄ powders (mpg-C₃N₄), it was necessary to remove the silica template. (NH₄)HF₂ aqueous solution was used as an etching agent. The dissolution reaction of the silica occurs as depicted in the following chemical equation:



To follow the dissolution of the silica and to investigate if it affects the structure and/or the chemical composition of the obtained mesoporous g-C₃N₄, each step involved in the removal of the silica template was characterised. The results presented here are obtained for a mpg-C₃N₄ with a cyanamide/silica mass ratio of 1:1. In the first step the hybrid powder (C₃N₄+Ludox) was stirred for 24 hours in a NH₄HF₂ 4M solution, filtrated and dried under vacuum. The removal of the silica was successful, as shown by XRD and FT-IR (**Figure 4.5**). As expected the broad peak with a maximum at 2θ = 22°, corresponding to amorphous silica, disappeared after the NH₄HF₂ treatment. The crystalline features of the g-C₃N₄ matrix e.g. the peak at 2θ = 13.1° and at 2θ = 27.3° are almost unchanged by the NH₄HF₂ treatment compared to the composite material and are similar to those observed for the bulk g-C₃N₄ (see introduction, **Figure 1.9**). From FTIR spectroscopy, the absence of the Si-O-Si vibration band at 1048 cm⁻¹ after the NH₄HF₂ treatment confirmed the dissolution of the silica. Furthermore, the NH₄HF₂ treated material exhibits the same vibration bands as the bulk g-C₃N₄, indicating that the NH₄HF₂ treatment has no influence on the chemical composition and structure of the g-C₃N₄ network.

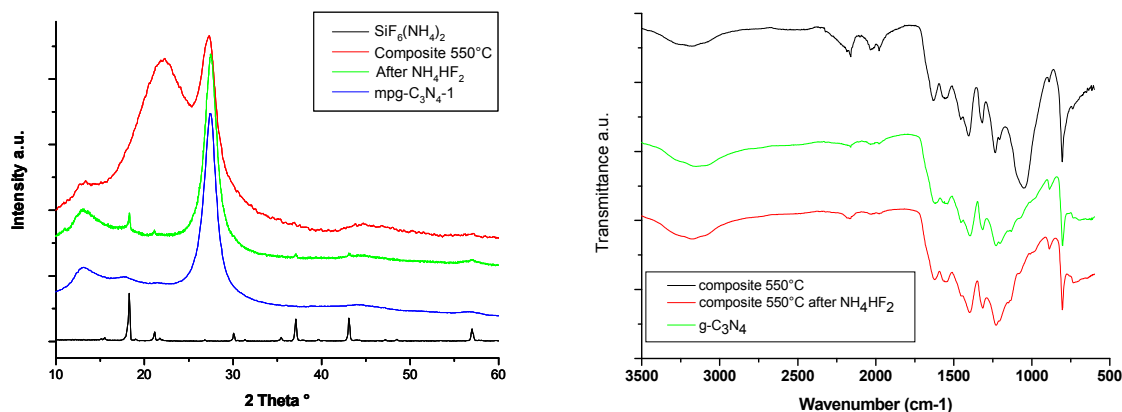


Figure 4.5: Left Side: X-Ray diffraction pattern of the hybrid Silica/ C_3N_4 powder (red curve), the NH_4HF_2 4M treated mpg- C_3N_4 powder without any further washing step (green curve), the final mpg- C_3N_4 -1-LHS40 and $(NH_4)_2SiF_6$ crystals precipitated from the filtrated solution in ethanol. Right side: FT-IR spectra of the hybrid silica/ C_3N_4 material calcined at 550°C (black curve), the final mpg- C_3N_4 -1-LHS40 after NH_4HF_2 treatment (red curve) and the bulk g- C_3N_4 at 550°C (green curve).

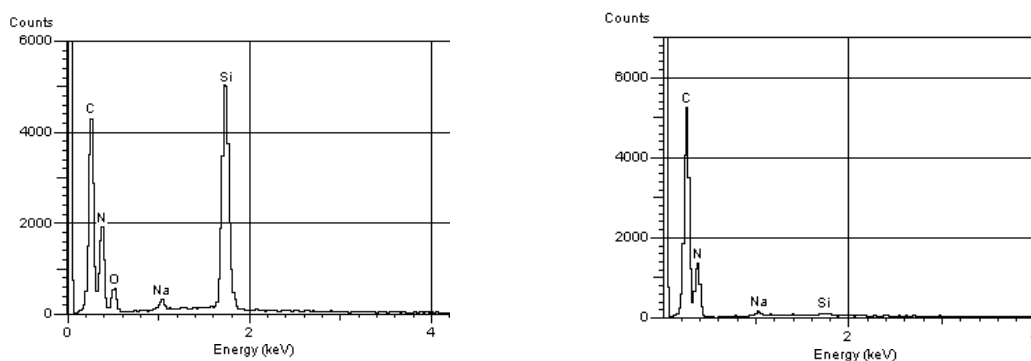


Figure 4.6: EDX spectrums of mpg- C_3N_4 before (left) and after the removal of the template (right).

Sample	C/N mol. ratio	SiO ₂ wt %	H wt%	C _x N _y H _z
Bulk g- C_3N_4	0.710	-	1.27	C ₃ N _{4.22} H _{1.22}
mpg- C_3N_4 -1-LHS40	0,701	60	0.92	C ₃ N _{4.28} H _{2.33}
mpg- C_3N_4 -1	0,705	-	2.55	C ₃ N _{4.25} H _{2.67}

Table 4.1: Composition of the mp- C_3N_4 -1 powder determined from elemental analysis before and after the removal of the silica template LHS-40.

However the presence of $(NH_4)_2SiF_6$ crystals in the pores of the NH_4HF_2 treated material is observed (peaks at $2\theta = 18.31^\circ$, 21.14° , 37.11° and 34.07° , **Figure 4.5**, left side, green curve). A supplementary washing step in water (at least 24 hours) is needed, to completely free the pores from any inorganic compound. Finally, the powder is washed in ethanol for several hours and dried in a vacuum oven. After the final washing step, the composition of the powder was determined by EDX measurements (**Figure 4.6**). As expected, only traces of silicon could be revealed (less than 0.2 weight %) and neither fluoride ions nor oxygen could be detected, proving the almost complete removal of the template and of the $(NH_4)_2SiF_6$. This was confirmed by TGA measurements. The residual mass after calcination under air up to 900°C

was less than 0.1 wt %. The composition of the powder was determined by elemental analysis both before and after the removal of the template. The results listed in **Table 4.1** show that the g-C₃N₄ network is not affected by the etching treatment. Indeed there is almost no change in the value of the C/N ratio (~0.7) before and after the removal of the template. The only difference is concerning the hydrogen amount in the samples. The hydrogen amount increases after the NH₄HF₂ treatment, which might be attributed to the protonation of the terminating amine groups present on the surface of the material and/or to physisorbed water residues. In this sense it is not surprising that the hydrogen content is lower for the bulk g-C₃N₄ than for the mesoporous C₃N₄ with high surface area.

To conclude the optimal dissolution procedure to completely free the porosity of the material was shown to be a treatment of 48 hours in 4 M NH₄HF₂, followed by a water washing under stirring of 48 hours, succeeded by an ethanol washing of 5 hours, followed by the drying at 80°C under vacuum of the powder. This etching procedure was applied for all silica templated g-C₃N₄ materials synthesised in this work.

4.1.4 Characterisation of mesoporous graphitic carbon nitride with 12 nm pores (mpg-C₃N₄-LHS40)

Mesoporous graphitic carbon nitride powders (mpg-C₃N₄-x-LHS40) with different silica/cyanamide weight ratios were synthesised with the procedure described above. **Table 4.2** gives the composition in mass of cyanamide and used template (Ludox HS 40, LHS40) of the different mesoporous powders.

Sample	mpg-C ₃ N ₄ -0.5-LHS40	mpg-C ₃ N ₄ -1-LHS40	mpg-C ₃ N ₄ -1.6-LHS40
Ludox HS 40 (g)	1.25	2.5	4
Cyanamide (g)	1	1	1

Table 4.2: Composition in cyanamide and silica template (LHS40) in mass (g) of different mesoporous graphitic C₃N₄ powders with 12 nm pores.

Elemental analysis (results listed in **Table 4.**) shows that the composition of the powders is almost not affected by the increasing template amount. The C/N ratios are slightly rising in value with increasing template amount but stays around 0.7 (before and after the removal of the template in each case). The main difference between the samples is the hydrogen amount after the NH₄HF₂ treatment, which increases with the template content of the powders, probably resulting from protonated surface amine functions or from physisorbed water. In this sense it is not surprising that the highest hydrogen content is found for the powder with the highest expected surface area.

Sample	C/N mol. ratio	SiO ₂ wt %	H wt%	C _x N _y H _z
Bulk g-C ₃ N ₄	0.71	-	1.27	C ₃ N _{4.22} H _{1.22}
mpg-C ₃ N ₄ -0.5-550°C	0.70	45	1.12	C ₃ N _{4.22} H _{1.99}
mpg-C ₃ N ₄ -0.5-LHS40	0.695	-	1.96	C ₃ N _{4.31} H _{2.03}
mpg-C ₃ N ₄ -1-550°C	0.70	60	0.92	C ₃ N _{4.28} H _{2.33}
mpg-C ₃ N ₄ -1-LHS40	0.705	-	2.55	C ₃ N _{4.25} H _{2.67}
mpg-C ₃ N ₄ -1.6-550°C	0.696	73	0.69	C ₃ N _{4.30} H _{2.57}
mpg-C ₃ N ₄ -1.6-LHS40	0.708	-	2.90	C ₃ N _{4.23} H _{3.10}

Table 4.3: Composition of the mp- C₃N₄ powders determined from elemental analysis before (mpg-C₃N₄-x-550°C) and after (mpg-C₃N₄-0.5-LHS40) the removal of the template.

After removal of the template, the porosity of the powders was investigated with nitrogen sorption measurements. **Figure 4.7** shows the adsorption isotherms for three mpg-C₃N₄-x-LHS40 powders, where increasing silica/cyanamide ratios were used in the synthesis. The isotherms are of type IV, typical for mesoporous materials, showing a hysteresis in the relative pressure range corresponding to mesopores. Unusual is the fact that at $p/p_0 > 0.9$, no plateau is observed, as it should be for purely mesoporous materials. This could reflect the presence of macropores in the materials, which probably results from the inter grain microstructure of the powders, as it can be seen by SEM (**Figure 4.9**). The surface area of the powders was estimated by using the BET model (**Table 4.4**). The surface area of the mpg-C₃N₄-LHS40 powders increases with increasing template content (**Figure 4.8**), related to the creation of a larger interface through incorporation of larger amounts of silica colloids. For evaluation of the pore size the BJH model was used. It should be noticed, that this model was developed for materials with cylindrical pores (see characterisation methods, section 2.1.2). Since there is no model developed for materials with spherical pores and that the BJH model still remains the most widely used for the determination of mesopore size, the BJH model was used for the pore size estimation for all the materials synthesised in this work. In all the samples, a pore size of 10 - 11 nm was determined. For a first estimation, the pore size is in good agreement with the size of the used silica template ($\varnothing \sim 12$ nm). This deviation of the calculated pore size with respect to the size of the template particles can be explained by three factors: first, as already mentioned the BJH model is not accurate for spherical pores; second one has to take into account the polydispersity of the particles ($\varnothing \sim 11-13$ nm) and finally, shrinkage of the silica colloids during thermal treatment at 550°C as well as shrinkage of the C₃N₄ network during the template removal can not be excluded.

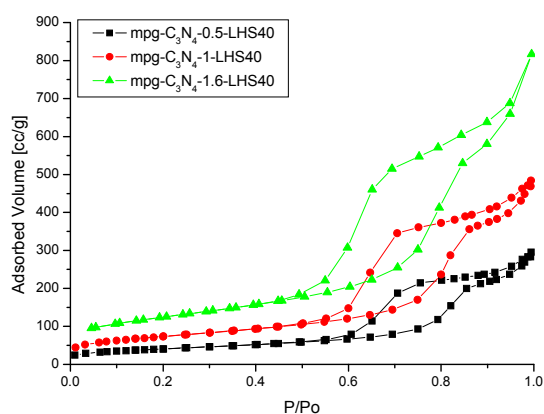


Figure 4.7: Nitrogen adsorption and desorption isotherms for mp-C₃N₄-LHS40 powders with increasing template content.

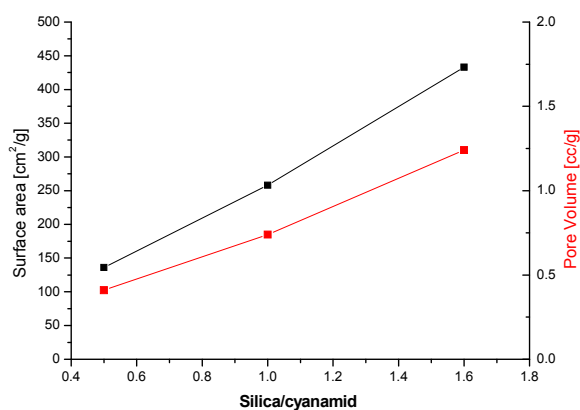


Figure 4.8: Behaviour of the surface area and the pore volume the mp-C₃N₄-LHS40 powders as a function of the silica/cyanamide ratio

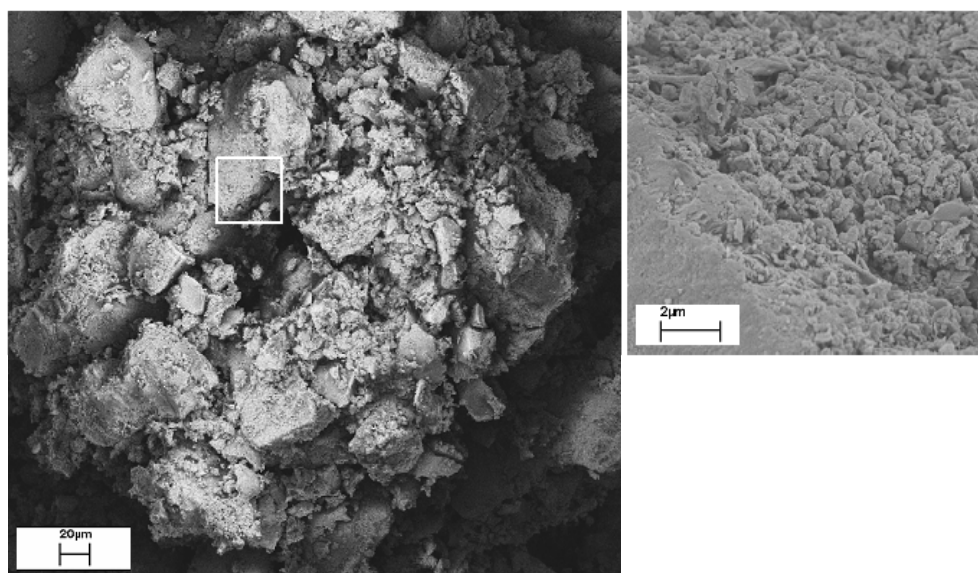


Figure 4.9: SEM micrographs of the mp-C₃N₄-1-LHS40 after NH₄HF₂ treatment.

Sample	Surface area (BET) [m ² /g]	Total Pore vol. [cc/g]	Pore diameter (BJH) [nm]
mpg-C ₃ N ₄ -0.5-LHS40	136	0.44	11.0
mpg-C ₃ N ₄ -1-LHS40	258	0.72	11.0
mpg-C ₃ N ₄ -1.6-LHS40	433	1.26	10.2

Table 4.4: Surface area, total pore volume and pore size of different mpg-C₃N₄ with increasing silica/cyanamide ratios after the removal of the template.

The nanostructure of the mpg-C₃N₄-LHS40 powders was furthermore investigated with TEM measurements. As can be seen in **Figure 4.10**, the mpg-C₃N₄-1-LHS40 features nearly spherical pores with diameters between 10 - 12 nm, confirming the results obtained from the nitrogen sorption. A comparison between the TEM image of the template LHS40 (**Figure 4.1**)

and the TEM image of the mpg-C₃N₄-LHS40, evidences that the disordered pore system can be regarded as a “replica”, i. e. as a negative image of the silica sol used as template. In addition, electron diffraction of a selected area proves the partial crystallinity of the pore walls, which is revealed by one intense diffraction ring at $d = 0.33$ nm, corresponding to the stacking distance of g-C₃N₄.

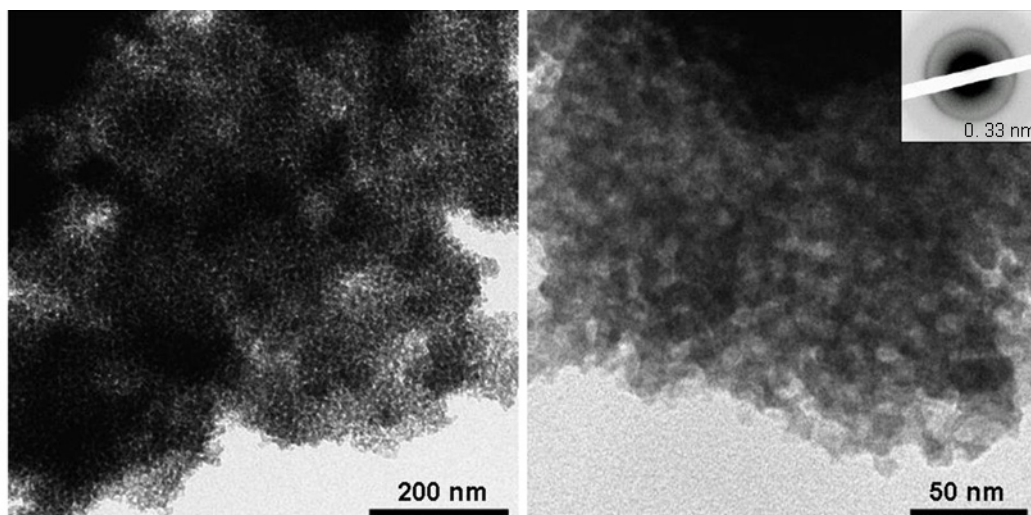


Figure 4.10: TEM images of the sample mpg-C₃N₄-1-LHS40 after template removal. The inset in the right image shows the diffraction figure obtained from selected area electron diffraction (SAED). The intensive diffraction ring corresponds to a distance of $d = 0.33$ nm.

To get a closer insight the nanostructure of the mpg-C₃N₄ powders, small angle X-Ray scattering (SAXS) measurements were performed. For all the samples, the scattering curves exhibit a form factor contribution of more or less monodispersed spheres, so that the presence of spherical pores could be assumed. For a first approximation, the curves were fitted with a model for hard spheres without interactions. A mean diameter of 11.5 nm was determined with a polydispersity of 1.6. For all samples the scattering curves showed a so called *Porod* behaviour, e.g. that the intensity decreases with s^{-4} , where s is the scattering vector in the reciprocal space (**Figure 4.11**). The *Porod* behaviour is typical for a two phase system with sharp interfaces. Using the *Porod* theory, presented in the characterisation method part, it was possible to determine numerically the *Porod* length l_p from **Equ. 2.21** and to give an estimation about the surface area S/V , the pore and wall dimension in the different samples with **Equ. 2.18** and **Equ. 2.19**. The porosity Φ can be calculated from the pore volume determined by nitrogen sorption. For this the density of the mpg-C₃N₄ is required and was determined by ultracentrifugation techniques ($d_{g-C_3N_4} = 1.85$). The results are summarized in **Table 4.5**. Concerning the surface area, the values obtained from the SAXS analysis are in good agreement with the values obtained from the nitrogen sorption (BET). This is especially true for the two samples with the lowest amount of template. The deviance for the sample mpg-C₃N₄-1.6-LHS40 with the highest template content, might originate from a higher amount

of macropores in the sample, creating additional surface area, and which is not “seen” by SAXS. The pore sizes determined by the SAXS analysis are in a very good agreement with the values obtained with the BJH model from the sorption experiments. This confirms that the pores in the mpg-C₃N₄-LHS40 powders are around 11 nm in diameter corresponding well with the size of the LHS40 template particles (12 nm).

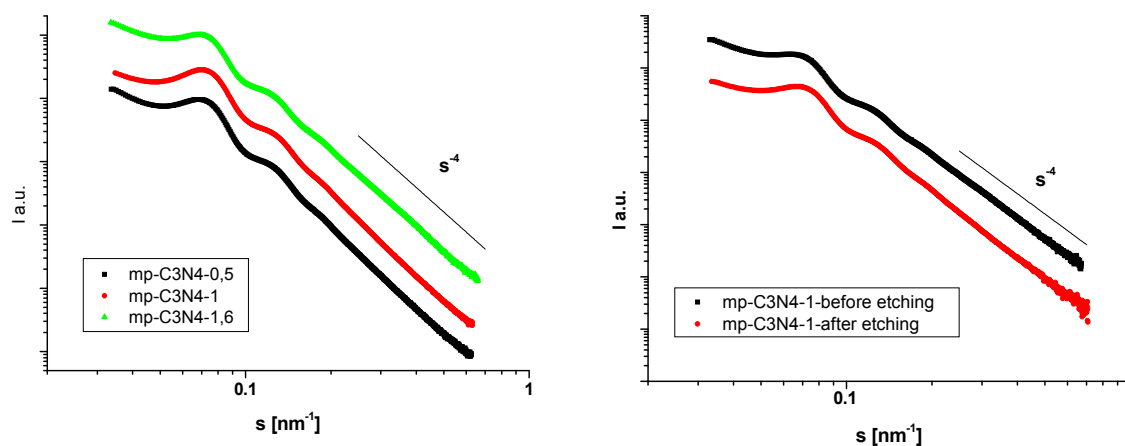


Figure 4.11: Right side: SAXS data from mp-C₃N₄-LHS40 powders after the removal of the template with increasing template content. Left side: SAXS data from mp-C₃N₄-1-LHS40 before and after the removal of the template.

Sample	Pore.Vol ($\Phi < 40$ nm) [cc/g]	Φ	I_p	S/V (SAXS) [m ² /g]	Surf. area (BET) [m ² /g]	D_{pore} SAXS [nm]	D_{pore} BET [nm]	D_{wall} SAXS [nm]
mpg-C ₃ N ₄ -0.5-LHS40	0.438	0.45	6.17	154	136	11.3	11.0	13.6
mpg-C ₃ N ₄ -1-LHS40	0.690	0.57	4.92	243	258	11.4	11.0	8.60
mpg-C ₃ N ₄ -1.6-LHS40	1.010	0.66	3.56	388	433	10.4	10.2	6.20

Table 4.5: SAXS results from the different mpg-C₃N₄-LHS40 powders with increasing silica/cyanamide ratio.

4.1.5 Characterisation of mesoporous graphitic carbon nitride with 23nm pores (mpg-C₃N₄-LTMA)

Following the same synthesis procedure as described for the mesoporous C₃N₄ powders with 11 nm pores (mpg-C₃N₄-LHS40), Ludox TMA from Aldrich (LTMA) was used as template, instead of Ludox HS-40 (LHS-40) to generate bigger pores in the C₃N₄ network. It is a 35% in weight silica colloidal suspension, with silica colloids of a mean diameter of 23 nm, as can be seen in the TEM picture of the LTMA template in **Figure 4.2**. The composition of the different mpg-C₃N₄-LTMA powders is given in **Table 4.6**.

Sample	mp-C ₃ N ₄ -0.5-LTMA	mp-C ₃ N ₄ -0.8-LTMA	mp-C ₃ N ₄ -1.1-LTMA	mp-C ₃ N ₄ -1.4-LTMA
Ludox TMA (LTMA) (g)	1.5	2.3	3.2	4.1
Cyanamide (g)	1	1	1	1

Table 4.6: Mass composition in cyanamide and silica template LTMA of different mpg-C₃N₄-LTMA powders.

After the removal of the template, the mpg-C₃N₄-LTMA powders were characterised concerning their crystallinity and their chemical composition. As only the size of the template was modified, no significant change in the crystallinity was observed from the mpg-C₃N₄-LHS40 samples. All powders presented the typical features of g-C₃N₄. The mean C/N ratio determined from elemental analysis was about 0.7, which is comparable to the values obtained both for the bulk and the mpg-C₃N₄-LHS40 materials. Finally the nanostructure of the obtained powders was investigated via TEM, nitrogen sorption and SAXS measurements. As for mpg-C₃N₄-LHS40 samples, the isotherms are of type IV and characteristic for mesoporous materials (**Figure 4.12**), and high surface areas are obtained (**Table 4.7**). The surface area of the obtained samples goes through a maximum for a LTMA/cyanamide ratio of 1.1. This speaks for a partial collapse of the porous network in the mpg-C₃N₄-1.4-LTMA powder and is confirmed by the observed drop in the pore volume. This is furthermore supported by the change observed in the hysteresis loop of the mpg-C₃N₄-LTMA-1.4 sample, which is less defined than for the other samples. The observed rise of the isotherms at $p/p_o > 0.95$ indicates the presence of additional macroporosity in the sample. This rise becomes more and more pronounced with increasing LTMA content, suggesting that the increasing of the porogen amount affects not only the mesoporosity but also the macroporosity. The mpg-C₃N₄-LTMA powders exhibit a mean pore size of 23 nm [BJH] (**Table 4.7**) which is in good agreement with the size of the LTMA template. From TEM measurements a well defined porous network of spherical pores could be observed. The mean pore diameter was determined to be around 23.5 nm, but pores with diameters ranging from 20 to 28 nm were found. This is not surprising, since it just reflects the polydispersity of the used LTMA template, as can be seen in **Figure 4.2**.

Sample	Surface area (BET) [m ² /g]	Total Pore vol. Pores < 350 nm [cc/g]	Pore diameter (BJH) [nm]
mpg-C ₃ N ₄ -0.5-LTMA	105	0.529	23.3
mpg-C ₃ N ₄ -0.8-LTMA	133	0.755	23.8
mpg-C ₃ N ₄ -1.1-LTMA	183	1.142	23.4
mpg-C ₃ N ₄ -1.4-LTMA	167	1.083	23.1

Table 4.7: Surface area, total pore volume and pore size of different mpg-C₃N₄-LTMA powders with increasing silica/cyanamide ratios.

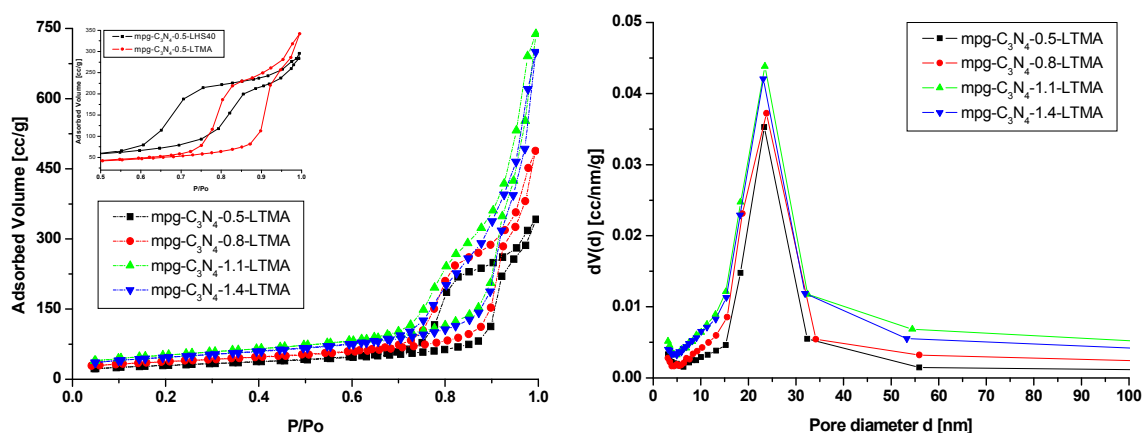


Figure 4.12: Nitrogen adsorption and desorption isotherms for LTMA templated $\text{mpg-C}_3\text{N}_4$ powders. The inset presents a zoom of the isotherms of the $\text{mpg-C}_3\text{N}_4\text{-0.5-LHS40}$ and $\text{mpg-C}_3\text{N}_4\text{-0.5-LTMA}$ powders.

Figure 4.13: Pore size distribution determined with the BJH model for the adsorption branch for LTMA templated $\text{mpg-C}_3\text{N}_4$ powders.

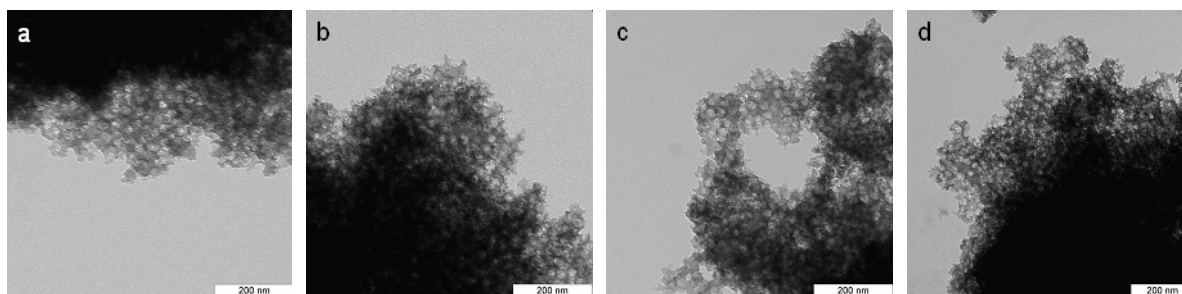


Figure 4.14: TEM measurements of a) $\text{mpg-C}_3\text{N}_4\text{-0.5-LTMA}$ b) $\text{mpg-C}_3\text{N}_4\text{-0.8-LTMA}$ c) $\text{mpg-C}_3\text{N}_4\text{-1.1-LTMA}$ d) $\text{mpg-C}_3\text{N}_4\text{-1.4-LTMA}$.

As for the $\text{mpg-C}_3\text{N}_4\text{-LHS40}$ powders, the values for the pore diameters obtained from the BJH analysis and from TEM measurements are in good agreement. Supplementary SAXS measurements were also performed. The SAXS curves (**Figure 4.15**) both before and after the removal of the LTMA template exhibit the typical feature of a “spherical” form factor. No significant change is observed before and after the removal of the template, indicating that the imprinted colloidal nanostructure is perfectly replicated and kept after the etching treatment. All curves show a typical *Porod* behaviour for high s values, since the intensity decreases with s^{-4} . The surface areas obtained by SAXS (**Table 4.8**) are in good agreement with the values obtained from the nitrogen sorption measurements. The drop of the surface area for the $\text{mpg-C}_3\text{N}_4\text{-1.4-LTMA}$ sample is confirmed. Concerning the pore sizes, the *Porod* SAXS analysis gives smaller pore sizes (18.1-19.9 nm) than determined by TEM or BJH (23 nm), while the

fitting of the curves with a sphere model gives pore sizes between 22.3 and 23.2 nm with a polydispersity close to 2. This deviance observed for the *Porod* analysis indicates the presence of some smaller “pores” in the pore wall, which are not accessible by nitrogen sorption. Those pores result probably from stacking defects between the sheets. Since the walls are thicker in the case of the LTMA powders, it is not surprising that this effect is enhanced in the case of the LTMA powders, compared to the LHS40 powders.

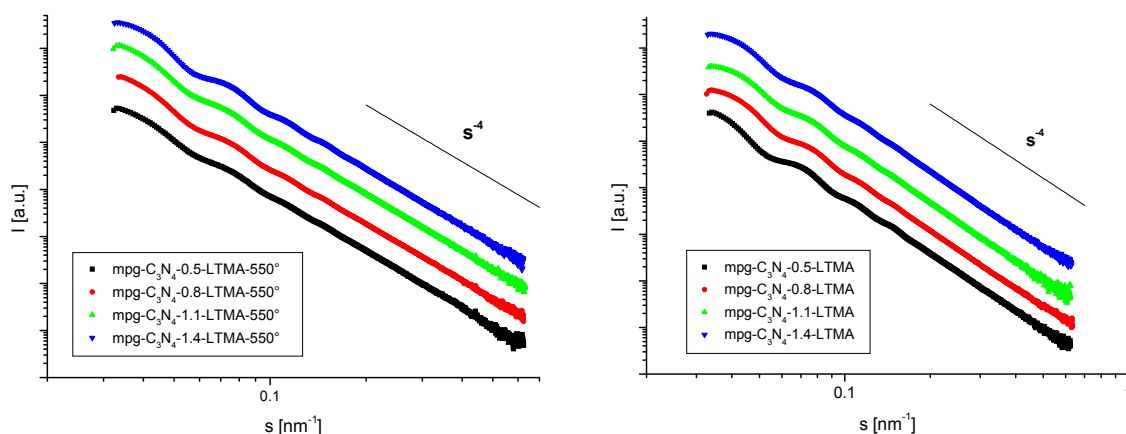


Figure 4.15: SAXS data from mpg-C₃N₄-LTMA powders before (left side) and after the removal of the template (right side).

Sample	Pore.Vol ($\Phi < 40$ nm) [cc/g]	Φ	I_p	S/V (SAXS) [m ² /g]	Surf. area (BET) [m ² /g]	D_{pore} SAXS [nm]	D_{pore} BET [nm]	D_{wall} [nm]
mpg-C ₃ N ₄ -0.5-LTMA	0.44	0.46	9.92	97	105	19.9	23.3	13.7
mpg-C ₃ N ₄ -0.8-LTMA	0.6	0.53	8.55	130	133	19.9	23.8	12.2
mpg-C ₃ N ₄ -1.1-LTMA	0.85	0.62	7.56	172	183	18.1	23.4	16.2
mpg-C ₃ N ₄ -1.4-LTMA	0.76	0.59	8.12	154	166.5	18.3	23.1	21.7

Table 4.8: SAXS results from the different mp-C₃N₄-LTMA powders after the removal of the template with increasing LTMA/cyanamide ratio.

4.1.6 Mesoporous g-C₃N₄ as metal free catalyst for benzene activation in Friedel-Crafts type reactions

The field of mesoporous materials was for a long time restricted to inorganic solids^[62] and led to numerous applications especially as catalysts and catalytic supports.^[63] Due to its unique electronic properties combined with its large surface area, mpg-C₃N₄ materials were expected to be potential materials for catalytic applications. According to Kroke *et al.*^[21] the basic motives of a g-C₃N₄ sheets are melem rings linked together by planarized nitrogen bridges (**Figure 4.16**). DFT calculations were performed using the Gaussian 03 package with the B3PW91 functional on a model melem unit to gain insight into the local electronic behavior of g-C₃N₄. The optimized geometry is shown in **Figure 4.17**. It is worth noticing that even in the uncondensed form the amino groups are planar, indicating a sp² hybridization of the corresponding nitrogen atoms. In this case the lone pair of those atoms participates to π system. The three highest occupied molecular orbitals feature π -symmetry, whereas HOMO-3 is an antibonding combination of the atomic orbitals describing the lone pairs of the “aromatic” nitrogen atoms. These results are in good qualitative agreement with the electronic structures of tri-s-triazine calculated by Le Breton *et al.* as early as 1984.^[64] The HOMO consists exclusively in an antibonding combination of the p_z-orbitals of the heterocyclic nitrogens. This is exactly the symmetry of the highest unoccupied π type orbital in the *Hückel* model of benzene. It should thus be possible for the melem units to transfer electron density to aromatic rings through overlapping of those orbitals, resulting in a very unusual activation of the aromatic rings. A perfect infinite g-C₃N₄ sheet, however, is likely to feature an electronic band structure and thus limited electron localization. The above mentioned activation path might therefore only be possible on defects and terminations of the sheet, promoting electron relocalization. In the case of graphite it is well known that defects such as edges,^[65] curvature,^[66] or doping atoms^[67] can induce electron relocalization. In addition, such defects have recently been demonstrated to be catalytically active sites in the oxidative dehydrogenation of ethylbenzene.^[68, 69] Due to its structure, mpg-C₃N₄ features almost all the above mentioned sources of relocalization combined with a high surface area, i.e. offering large areas of catalytic sites. This stimulated the investigation of the activity of mpg-C₃N₄ as catalyst for the activation of aromatic compounds. This work was realized in collaboration with Dr. Frederic Goettmann.

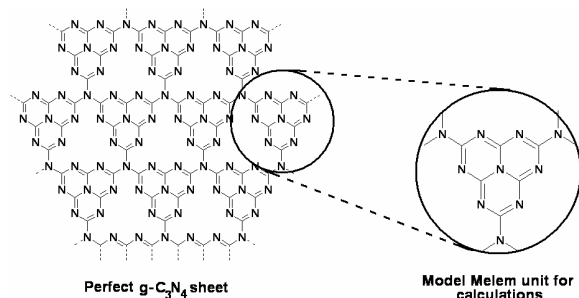


Figure 4.16: Representation of a perfect graphitic C_3N_4 and of the melem unit used for modelling purposes.

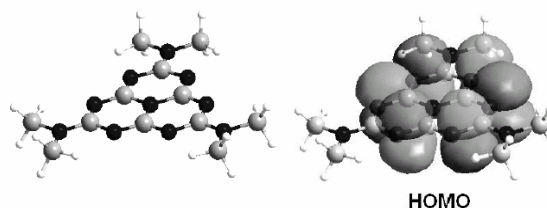


Figure 4.17: Optimized geometry of the model melem ring (left) and isodensity surface of the corresponding highest occupied molecular orbital (right).

The Friedel Crafts (FC) acylation in a classical way is a typical aromatic C-H activation process where a Lewis acid such as $AlCl_3$ is used to activate the electrophile which will then attack the aromatic compound. However if one thinks of the potential activation of the nucleophile, i.e. the aromatic compound instead of the electrophile, in principle the same outcome should be expected. In fact, graphite particles have already been used to promote Friedel-Crafts reactions using this idea.^[32, 70]

Here three mesoporous samples of $g-C_3N_4$ with 11 nm pores, namely $mp-C_3N_4-0.5-LHS40$, $mp-C_3N_4-1-LHS40$ and $mp-C_3N_4-1.6-LHS40$, described previously (section 4.1.4), with increasing surface area (amount of template). **Table 4.4** (section 4.1.4) were tested as Friedel-Crafts acylation catalysts.

Firstly the influence of various solvents (benzene, heptane and anisole) on the acylation of benzene with hexanoyl chloride to form n-hexanophenone by using $mp-C_3N_4-1-LHS40$ as a catalyst was investigated. **Table 4.9** shows the corresponding conversion rates in the presence of each solvent.

Solvent	Benzene	Heptane	Anisole
Temperature [°C]	80	90	150
Conversion rate [%]	16	80	60

Table 4.9: Catalytic activity of $mp-C_3N_4-1-LHS40$ in the Friedel-Crafts acylation of benzene with hexanoyl chloride in different solvents.

In all cases, a medium to high conversion is obtained, indicating that $mpg-C_3N_4-1-LHS40$ indeed acts as an activation catalyst. The observed difference between benzene and heptane is likely to result from a passivation of the surface of $mpg-C_3N_4$ by a large excess of benzene. The choice of anisole as a solvent might be surprising as it is well known to be a much more reactive Friedel-Crafts substrate than benzene. However in the presence of $mpg-C_3N_4$, the only formed product in mixtures of benzene and anisole is n-hexanophenone, ascertaining that anisole does not react as long as benzene is present. As the catalysis is supposed to originate

from electron donation from melem units to the aromatic substrate, substrates having lower lying molecular orbitals interact stronger with the C_3N_4 surface. On the other hand, it has to be considered that substitutions on the aromatic ring alter the symmetry of the molecular orbitals, resulting in an inferior overlap with the “HOMO” of localized melem units. These two effects, donor-acceptor interaction and change of symmetry, together with steric effects, make the prediction of a reactivity sequence rather difficult. Current work is devoted to separate those geometric from electronic contributions.

Heptane as a suitable solvent was then used in a set of reactions to analyse the catalytic activities of the powders as a function of their surface area. The acylations were performed with hexanoyl chloride (50 mg) and benzene (150 mg) in heptane (5 g) for 20 h at 90°C using 25 mg of the corresponding carbon nitride as a catalyst. The products of the reactions were analyzed via GC with an internal probe for quantification. Some results are summarized in **Table 4.10**.

Sample	bulk- C_3N_4	Graphite	mpg- C_3N_4 -0.5-LHS40	mpg- C_3N_4 -1-LHS40	mpg- C_3N_4 -1.6-LHS40
Conversion rate [%]	0	1	52	80	52

Table 4.10: Catalytic behaviour of diverse mpg- C_3N_4 -LHS40 samples in the Friedel-Crafts acylation of benzene with hexanoyl chloride in heptane at 90°C for 20 hours.

As can be seen in **Table 4.10**, most of the mesoporous carbon nitrides used are indeed active Friedel-Crafts acylation catalysts whereas the bulk carbon nitride failed to prove any activity. Graphite (1 μ m spheres) was used under the same conditions as a control and was by far less active.

No clear correlation could be found between the specific surface area and the catalytic activity within probes that were submitted to the same heat treatment, etching treatment, washing and drying steps with activity going through a maximum. As can be seen from the SAXS measurements in section 4.1.4, **Table 4.5**, the pore walls become thinner with increasing template amount. So the maximum in activity observed for the mpg- C_3N_4 -1 powder likely results from a compromise between a high surface area and acceptable wall dimensions. Since the mpg- C_3N_4 -1 powder was determined to be the most active one, all following catalytic studies were performed using the mpg- C_3N_4 -1-LHS40 as a catalyst.

Although the actual active centres, which could be the isolated tri-s-triazine units, are not known yet, the catalysis most probably relies on the activation of the aromatics rather than the activation of the electrophile, as shown in **Figure 4.18**.

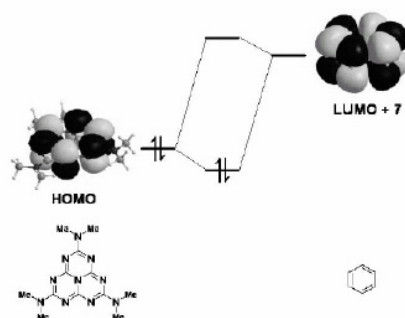


Figure 4.18: Schematic representation of one proposed activation mechanism of benzene on a model melem unit.

Therefore it was assumed that the Lewis base solid mpg-C₃N₄-1-LHS40 catalyst could also enable the use of less active electrophiles, such as alcohols, formic acid but also ammoniums or even urea, in Friedel-Crafts type reactions to activate benzene. For the catalytic experiments three alcohols, methanol, ethanol and isopropanol, as well as formic acid, urea and tetramethylammonium bromide were used. In each case the same reaction conditions were applied. 50 mg of mpg-C₃N₄-1-LHS40 were placed in a 40 mL autoclave, fitted with a Teflon cup, to avoid any metal contamination. Since the previous experiments concerning the Friedel-Crafts acylation of benzene with hexanoyl chloride have shown that the solvent could dramatically affect the efficiency of the catalyst, two series of catalytic tests were performed. In the first one, the solution added to the catalyst in the autoclave contained 5 mL of the electrophile and 200 mg of benzene. This was the case when the used electrophile is an alcohol. In the second one, the solution consisted in 5 mL of benzene and 200 mg of the desired electrophile (formic acid, urea, tetra methyl ammonium bromide). The sealed autoclave was heated to 150°C for 24 hours. The products of the reaction were analysed and quantified by GC and the products attribution was ascertained by ¹H NMR. The conversion rates were calculated on the amount of obtained product compared to the initial amount of limiting reactant. **Table 4.11** summarises the obtained results. Concerning the reactions with an alcohol as electrophile, isopropanol yielded 13 % of cumene under relatively mild conditions. The current industrial procedure relies on the alkylation of benzene with propene. In this sense it is important to note, that no side products could be observed in addition to cumene. Further optimization of the reaction conditions could probably lead to higher conversions. The reaction with ethanol yielded 16 % of p-diethyl benzene after 24 hours. In the case of methanol, depending on whether methanol is the solvent or not, it is possible to tune the products toward mesitylene or p-xylene, with good selectivities (100 % and 80 % respectively). The same reaction without catalyst did not provide any detectable amount of alkylation product, confirming that the observed products are related to the catalytic activity of the mpg-C₃N₄-

LHS40. The reaction of formic acid with benzene resulted in the formation of benzaldehyde in quantitative yield. The same reaction without catalyst leads to the decomposition of formic acid without the formation of any alkylation product. The attempts with molecules bearing nitrogen atoms afforded unpredicted results. Tetramethylammonium bromide yielded 100 % of toluene, corresponding to the transfer of one methyl group per ammonium molecule. This result is instructive from a mechanistic point of view, because tetramethylammonium is not a Lewis base (and thus cannot be activated in a standard Friedel Crafts way) and a moderate electrophile (the formal positive charge on nitrogen is in fact distributed on the four methyl groups). A reference test without catalyst yielded only 15 % of toluene. This supports the assumption that the catalysis proceeds via the activation of benzene.

Electrophile	Nucleophile	mpg-C ₃ N ₄ -1-LHS40	Conversion rate (%)	Products
Methanol 200 mg	Benzene 5 mL	50 mg	10	Toluene (20%) p-Xylene (80%)
Methanol 5 mL	Benzene 200 mg	50 mg	20	Mesitylene (100%)
Methanol 5 mL	Benzene 200 mg	-	< 0.5	-
Ethanol 5 mL	Benzene 200 mg	50 mg	18	p-Diethylbenzene (100%)
Isopropanol 5 mL	Benzene 200 mg	50 mg	13	Cumene (100%)
Formic acid 200 mg	Benzene 200 mg	50 mg	100	Benzaldehyde (100%)
Formic acid 200 mg	Benzene 200 mg	-	100	Decomposition products
Tetra methyl ammonium bromide 200 mg	Benzene 5 mL	50 mg	100	Toluene (100%)
Tetra methyl ammonium bromide 200 mg	Benzene 5 mL	-	15	Toluene (100%)

Table 4.11: Friedel-Crafts type reactions of benzene with various electrophiles catalysed by mpg-C₃N₄-1-LHS40.

In this section it was shown that mpg-C₃N₄ are interesting Lewis base type materials for the activation of aromatic compounds in Friedel- Crafts type reactions. They were suitable “metal free” catalysts for the acylation of benzene with acetyl chlorides and even for the alkylation of benzene with alcohols. These catalytic properties more likely result from a direct activation of the aromatic compound through electron donation from the mpg-C₃N₄ to the benzene rather than an activation of the electrophile.

4.2 Synthesis of macroporous graphitic carbon nitride

A macroporous graphitic carbon nitride with 60 to 70 nm pores was synthesised using hard templating by following the synthetic procedure of Johnson *et al.*,^[57] developed for ordered mesoporous polymers. Spherical silica colloids of 60-70 nm in size were prepared by using a microemulsion sol-gel synthesis (see section 3.1.2.1). The resulting silica colloids were pressed into a pellet, sintered at 800°C and subsequently used as hard template. The pressing was hoped to induce a close packing of the monodispersed particles, which should yield in an ordered porous g-C₃N₄ network. The template pellet once infiltrated with molten cyanamide was annealed at 550°C. The removal of the template with NH₄HF₂ (see section 4.1.3) yielded a yellow graphitic carbon nitride powder (CN-60). The complete removal of the silica template was confirmed by TGA (residual mass < 0.2 %) and FT-IR spectroscopy (disappearance of the Si-O-Si stretching band at 1050 cm⁻¹). The CN-60 powder exhibits the characteristic crystalline features of g-C₃N₄, as shown in **Figure 4.19** (intensive graphitic peak at $2\theta = 27.23^\circ$ { $d = 0.327$ nm}, broad in plane peak at $2\theta = 12.9^\circ$ { $d = 0.68$ nm}). As can be seen from SEM and TEM measurements, the CN-60 graphitic carbon nitride powder is a perfect replica of the silica template and exhibits a well defined homogeneous network of spherical pores of ~65 nm in size with a wall thickness of approximately 20-30 nm (**Figure 4.20**). Only a fraction of the sample exhibited ordered pores, while the here presented TEM reflects the structure of the main part of the sample, implying that inducing order by pressing of the colloids was only partially successful.

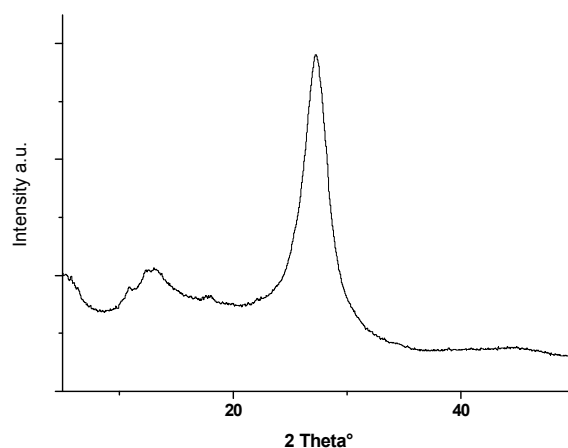


Figure 4.19: X Ray diffractogram of the macroporous porous carbon nitride CN-60 after the removal of the silica nanoparticle template.

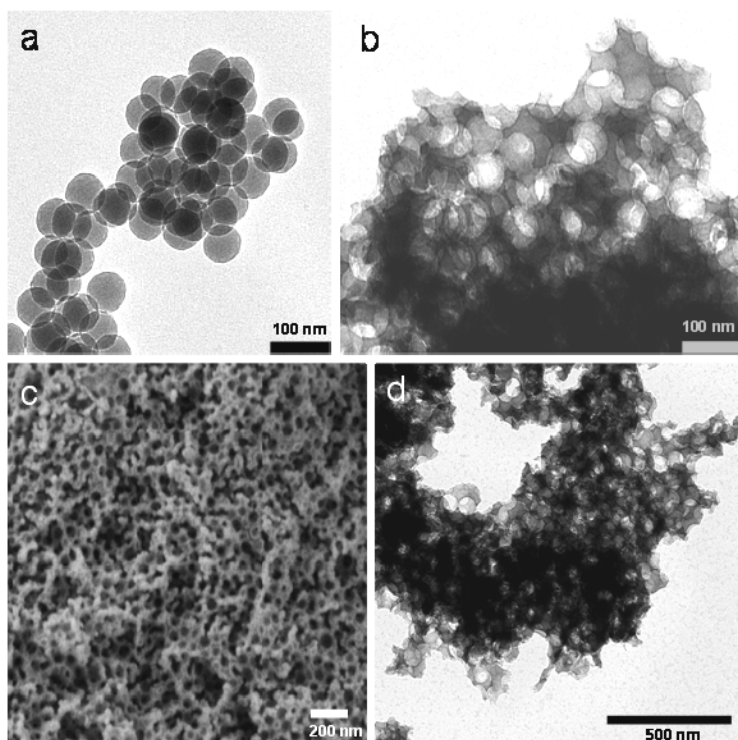


Figure 4.20: TEM and SEM images of the silica nanoparticles ST-60 (a) and of the porous graphitic carbon nitride (b,c,d) (CN-60) after the removal of the template.

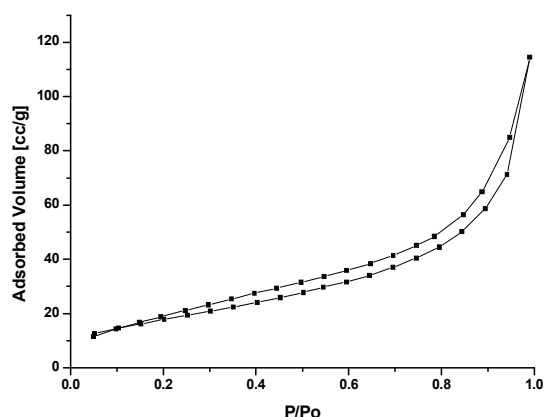


Figure 4.21: Nitrogen sorption adsorption and desorption isotherm of the macroporous carbon nitride CN-60 with 65 nm spherical pores. Surface area: 65 m²/g and meso-porosity: 23% in volume.

From nitrogen sorption (**Figure 4.21**), the surface area and the mesoporous pore volume were determined. The powder has a low specific surface area of 65 m²/g [BET], due to the large pore size, and an “apparent” pore volume of 0.165 cm³/g. The macropore volume can not be accessed by nitrogen sorption.

With a slightly modified approach, it was possible to synthesize a macroporous graphitic carbon nitride with 500 nm pores (CN-500), by changing the size of the silica template.

500 nm silica spheres provided by Merck were used (Monospheres M500). The silica powder was not pressed into a pellet but directly dispersed in molten cyanamide by using a sonication microtip. After annealing and removal of the template, a highly porous graphitic carbon nitride

was obtained, which features the same crystallinity and composition than the bulk material. SEM and TEM measurements (**Figure 4.22**) revealed a well defined spherical pore network with pore diameters of 480 nm, which are in good agreement with the size (~500 nm) of the used silica template particles. The pore walls of the resulting carbon nitride are extremely thin (10-50 nm), compared to the pore dimension. **Figure 4.23** shows the adsorption and desorption isotherms which are of type II and characteristic for macroporous adsorbents. The surface area of CN-500 is 16 m²/g and the apparent mesopore volume is only 0.06 cm³/g.

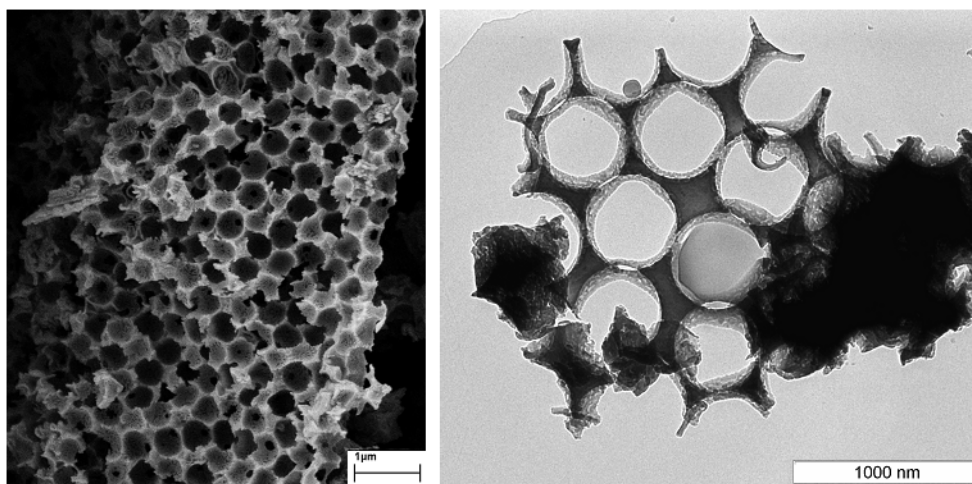


Figure 4.22: SEM (left) and TEM (right) micrographs of the macroporous CN-500 carbon nitride with 500 nm spherical pores.

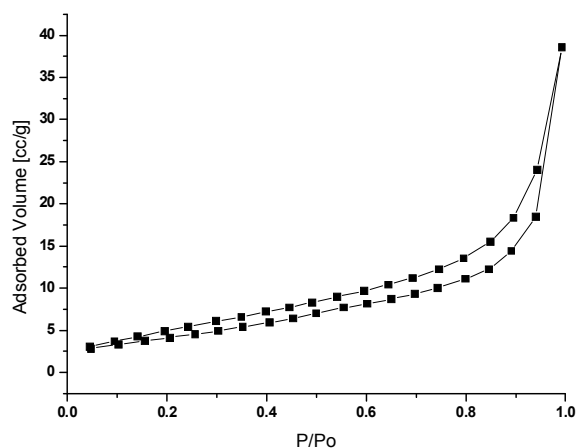


Figure 4.23: Nitrogen adsorption and desorption isotherm of a macroporous carbon nitride with 500 nm pores (CN-500).

4.3 Synthesis and characterisation of bimodal graphitic carbon nitride

In order to create a bimodal porosity in the graphitic carbon nitride matrix, two types of silica templates were used. On the one hand macroporosity was induced by using 500 nm silica spheres (M500), provided by Merck, and on the other hand mesoporosity was induced by the use of 12 nm silica colloids (LHS40). The ratio of cyanamide/M500 was fixed and only the amount of LHS-40 template was varied (**Table 4.12**). After the condensation at 550°C of the g-C₃N₄ network, the templates were etched away with NH₄HF₂ following the procedure described for the mesoporous powders. The complete removal of the templates was confirmed by TGA and FT-IR measurements. From elemental analysis the composition of the powders was close to 0.7.

Sample	CA/M500/LHS40 [g]	Surface area [m ² /g]	Pore volume [cc/g]	Pore size ads BJH [nm]
BM-CN-1-3	5/1/3	80	0.28	11.7
BM-CN-1-1	5/1/1	48	0.2	11.7
CN-500	5/1/0	16	0.06	-

Table 4.12: Material composition (CA: cyanamide), surface area and pore volume of different bimodal carbon nitride powders.

The macroporosity of the resulting samples was investigated by SEM and TEM. As it can be seen in the SEM images (**Figure 4.24**), ~ 500 nm pores are present in both samples. When the LHS40 content is increased, the macroporous structure is less defined, in the sense that the walls look more granular, resulting from the introduction of mesopores in the walls. From SAXS measurements (**Figure 4.25**, right) the typical features of ~ 11 nm spherical mesopores created through LHS-40 silica particles are evidenced (see section 4.1). The scattering curves show, as for the pure mesoporous systems (mpg-C₃N₄-LHS40) a *Porod* behaviour with a decrease in intensity with s^{-4} , for high s values. The contribution of a spherical form factor is responsible for the oscillations at small scattering vectors. A form factor minimum is observed at $s = 0,094 \text{ nm}^{-1}$, corresponding to entities of 10.6 nm in size, which could be attributed to the mesopores generated from the LSH40 template particle. TEM confirms the presence of mesopores within the macropore walls (**Figure 4.24**). It is seen that the density of mesopores in the macropore walls increases with increasing proportion of LHS40 in the carbon nitride powder. This is also supported by nitrogen sorption measurements, shown in **Figure 4.25**. In the case of both bimodal (BM) carbon nitride powders, an isotherm of type IV is observed as for the pure mesoporous samples (mpg-C₃N₄-LHS40), with an opening of a hysteresis in the range of $0.6 < p/p_0 < 0.9$ (see section 4.1.4), while no hysteresis is observed for the purely macroporous sample CN-500. The pore size [BJH] of the mesopores in the samples was

determined to be around 11.7 nm, which is in a good agreement with the size of the LHS40 silica template particles. As expected, the surface area of the samples increases as well as the pore volume, when the LHS40 content increases. Further rise of the LHS-40 content induced a drop to nearly zero of the surface area and the pore volume. This is due to the collapse of both macro- and mesopores. Indeed one can imagine that once the density of mesopores within the macropore walls overcomes a critical value, the macropore walls lose mechanical stability, and the pores will collapse.

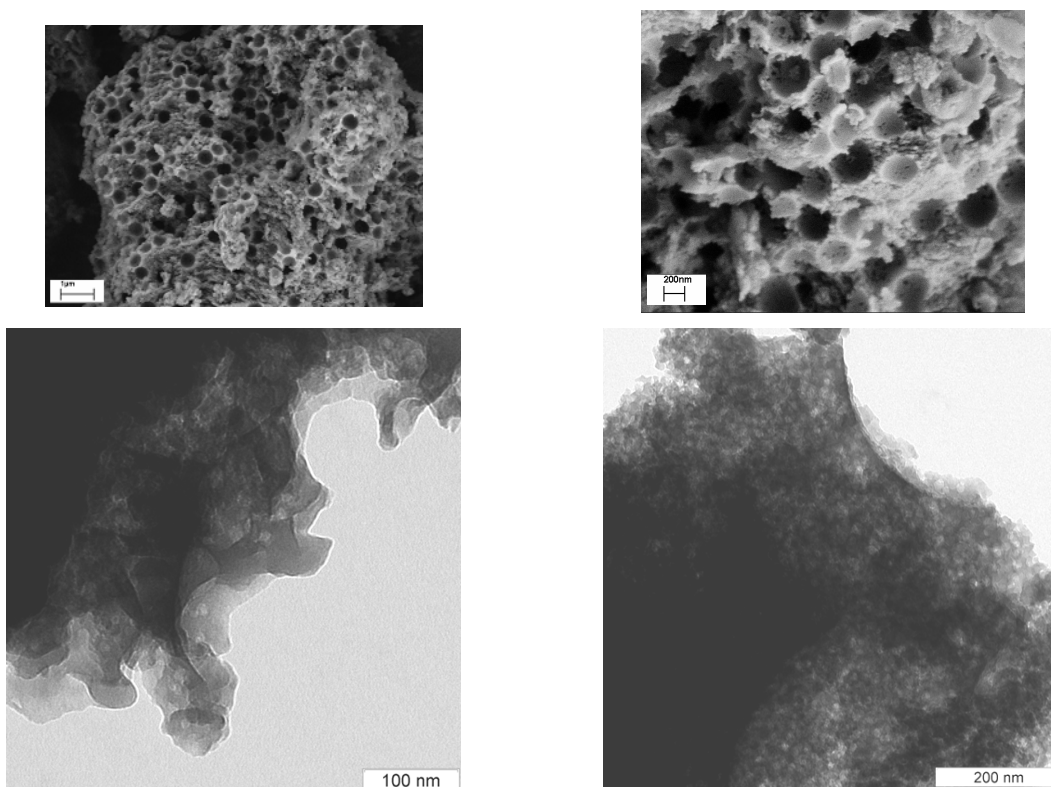


Figure 4.24: SEM and TEM pictures of bimodal g-carbon nitride powders with a fixed Si-500 content and different LHS40 contents.

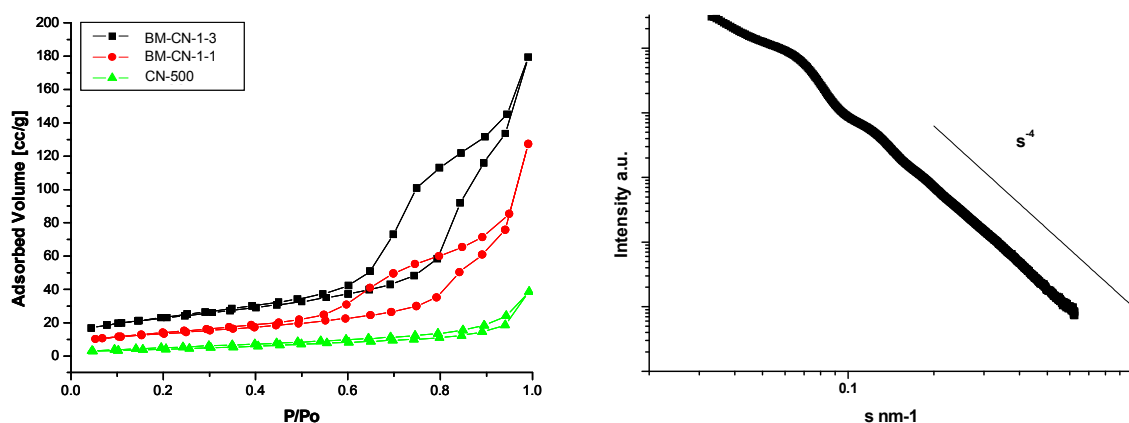


Figure 4.25: Left → Nitrogen adsorption and desorption isotherm of the bimodal carbon nitrides with increasing LSH40 content (red and black curve). The green curve corresponds to a pure macroporous carbon nitride without any add of LHS40. Right → SAXS pattern of the sample BM-CN-1-3.

4.4 Synthesis and characterisation of carbon nitride coatings on mesoporous silica structures

The previous sections have already shown that it is possible to synthesise nanostructured carbon nitrides by nanocasting using hard templates. In the literature several carbon coatings on silica surfaces are reported.^[1, 15] For example CMK-5^[71] materials are synthesised by infiltrating acetylene or furfuryl alcohol as carbon precursors, inside mesoporous silicas such SBA15 respectively, followed by a carbonisation or graphitisation heat-treatment. The resulting hybrid materials are actually carbon coatings on the silica walls, which is evidenced in the final nanopipe material after the removal of the template. The resulting CMK materials are interconnected carbon tubes, with an outer diameter fitting with the pore sizes of the starting silica material, and with inner diameters depending on the concentration of the precursor solution. This section investigates the possibility of synthesising well-defined graphitic carbon nitride coatings on high surface area silica supports, by following the synthetic strategy used for silica-supported carbon materials.

4.4.1 Synthesis of carbon nitride coatings on silica microspheres

Silica LiChospheres Si 100 (provided by Merck) with a diameter of 5 μm were used as support material. The Si100 particles are porous and exhibit a high surface area and a narrow pore size distribution with a maximum around 10.5 nm. As for the carbon related CMK materials, the Si100 particles were infiltrated with precursor (cyanamide) solutions with increasing concentrations and pyrolysed at 550° under nitrogen flow. The obtained powders vary from light to dark yellow with increasing cyanamide concentration. The graphitic carbon nitride loading on the silica support was measured using TGA and elemental analysis. As a general trend, the resulting amount of carbon nitride in the final material increased with increasing cyanamide concentration in the precursor solution (**Table 4.13**). No clear crystalline features of g-C₃N₄ could be observed in the X-ray diffraction pattern, indicating that only low quantity of g-carbon nitride is deposited on or in the silica support material. The condensation of the g-carbon nitride was confirmed by FT-IR spectroscopy and by elemental analysis. The characteristic vibration bands of condensed carbon nitride compounds could be observed (1200-1600 cm⁻¹: stretching modes of C=N heterocycles; 800 cm⁻¹: breathing modes of tri-s-triazine units; no band at 2160 cm⁻¹, corresponding to the -C \equiv N stretching modes). The organic part of the powders exhibits a C/N ratio from 0.72 to 0.70, values which are in a good agreement with the value of 0.71 found for bulk g-carbon nitride (**Table 4.13**). The weight amount in hydrogen of all the samples was lower than 1%.

Sample	CA/H ₂ O	CN wt%	C/N ratio	BET surface area	BET theo. surface area	Pore volume	Pore theo. volume
Si100	0.00	0.0	0	370	370	1.30	1.30
S1	1.00	40.5	0.72	103	222	0.45	0.77
S2	0.50	31.2	0.70	174	255	0.65	0.89
S3	0.25	17.2	0.70	251	306	0.93	1.08
Si100-N	0.00	0.0	-	304	-	1.18	-
C1	1.00	32.0	0.75	125	207	0.47	0.80
C2	0.50	27.0	0.75	154	222	0.60	0.86
C3	0.33	19.7	0.77	229	244	0.84	0.95

Table 4.13: Characteristics of g-carbon nitride loaded mesoporous silica samples. Si100 and Si100-N are the non-functionalised and respectively amine functionalised mesoporous silica supports. The theoretical BET surface area and pore volume would be expected for perfectly coated samples, were the loss in surface area and pore volume would only be related to the increase in mass induced by the coating.

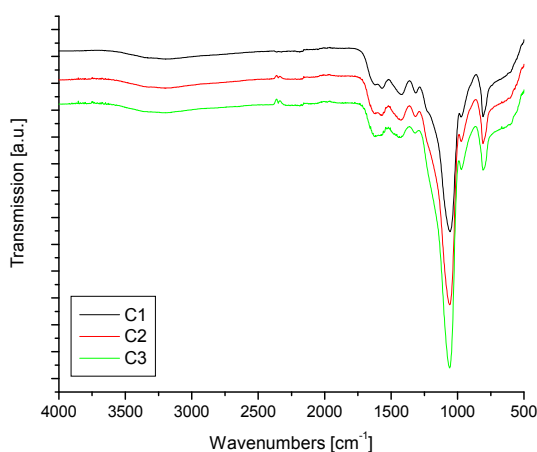


Figure 4.26: FT-IR spectrograms of the g-carbon nitride coated functionalised mesoporous silica powders.

The morphology of the samples was investigated by SEM. **Figure 4.28** shows the Si100 Merck particles before and after the coating procedure. No change in size or shape is observed. To evidence the formation of a coating, the samples were treated with NH_4HF_2 to etch away the silica support. As it can be seen, carbon nitride structures related in shape and size to the silica support were obtained. It is remarkable that the obtained “spheres” seem to have extremely thin walls and are nearly collapsed, looking like “deflated” footballs. This observation indicates that the coating formation was successful, yielding a thin (thus flexible) deposited carbon nitride layer. To confirm this hypothesis, the porosity of the coated samples was investigated by nitrogen sorption and compared with the porosity of the starting Si100 powder. As can be seen in **Table 4.13** and **Figure 4.29**, when the amount of carbon nitride is increased in the sample the surface area of the powders decreases as well as the total pore volume, as it is expected in a coating formation. For a coated material the decrease of the surface area and the

pore volume is mainly related to two factors. First, the specific surface area expressed in m^2/g and the pore volume expressed in cm^3/g of the coated material drop since the weight of the coated material is increased compared to the uncoated support. Thus a drop of the surface area and the pore volume proportional to the coating weight loading of the support is expected for the formation of very thin coatings. Second, the drop of the surface area and the pore volume depends also from the thickness of the formed coating layer. Indeed thin coatings, which are almost unchanging the pore geometry should not affect further the surface area and the pore volume, while thick coatings, which reduce considerably the pore radius, should induce a supplementary decrease of the surface area and the pore volume. The theoretical BET surface area in **Table 4.13** is only a point of comparison and corresponds to the surface area of a coated silica sample, where only the weight drop of the surface area and the pore volume is considered. As can be seen in **Table 4.13**, the measured surface area and pore volume for the coated samples differs from the theoretical expected ones, in the case of a perfect very thinly coated material. This deviation could firstly originate from a lowering of the pore size by the coating layer, as depicted schematically in **Figure 4.27** or secondly by a partial pore blocking of the micro- and mesopores through the graphitic carbon nitride. In the first case, a decrease in the pore size should be observed. This is only observed (with a significant decrease of almost 2 nm in diameter) for the sample S2. For the other samples no significant change is observed for the pore sizes with increasing graphitic carbon nitride loading, indicating that partial pore blocking is more probable. The disappearance of the small mesopores [$\text{Ø} \sim 6 \text{ nm}$] (**Figure 4.29**) with increasing carbon nitride loading seems to confirm the hypothesis of a partial pore blocking in the powders rather than the formation of a defined coating on the silica walls of the support

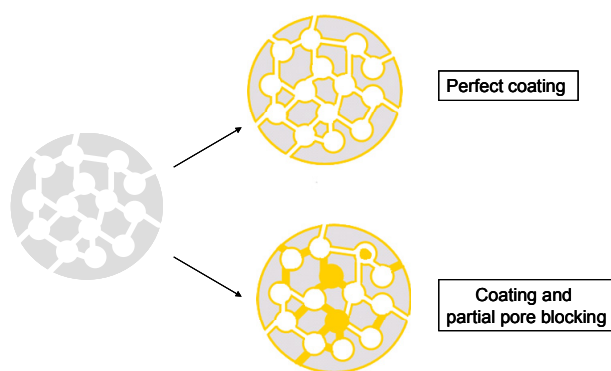


Figure 4.27: Schematic description of a perfect coating situation and a partial pore blocking of the pores of the mesoporous silica support.

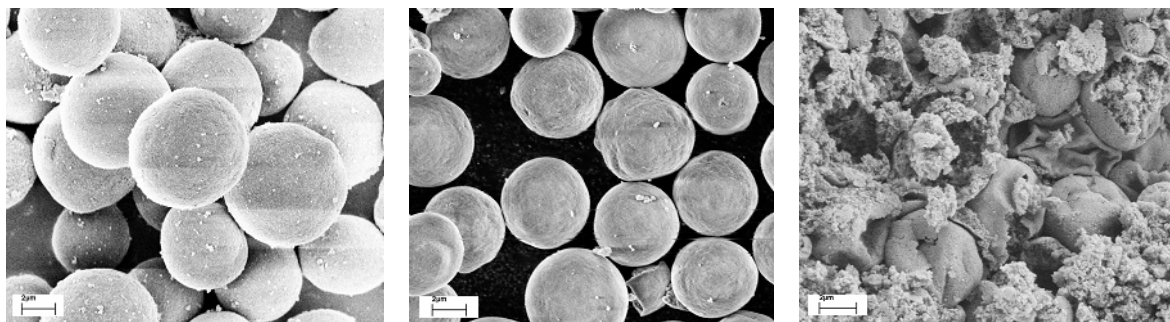


Figure 4.28: SEM images from the left to the right side of Si100, S2 and S2 after the NH_4HF_2 treatment.

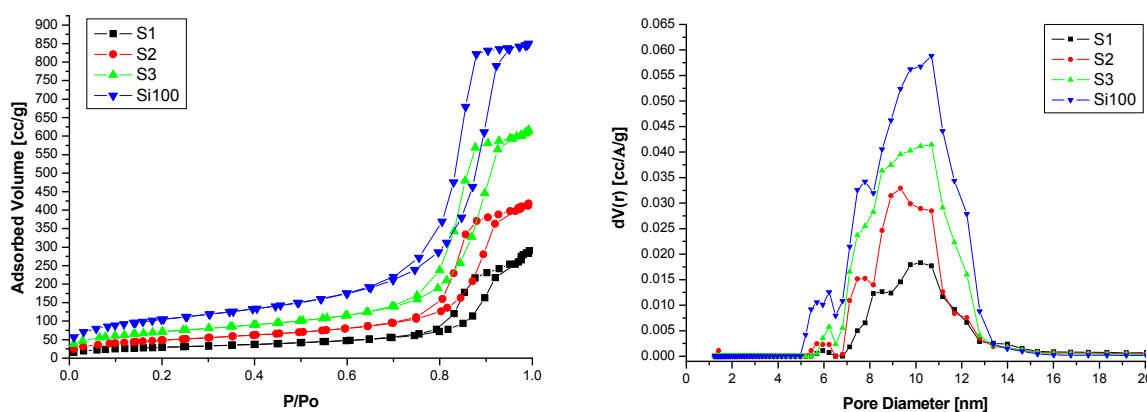


Figure 4.29: Nitrogen adsorption isotherms Cyanamid infiltrated Si-100 mesoporous silica powders, with decreasing carbon nitride loading ($\text{S3} > \text{S2} > \text{S1} > \text{Si100}$) and the corresponding pore size distribution (DFT model).

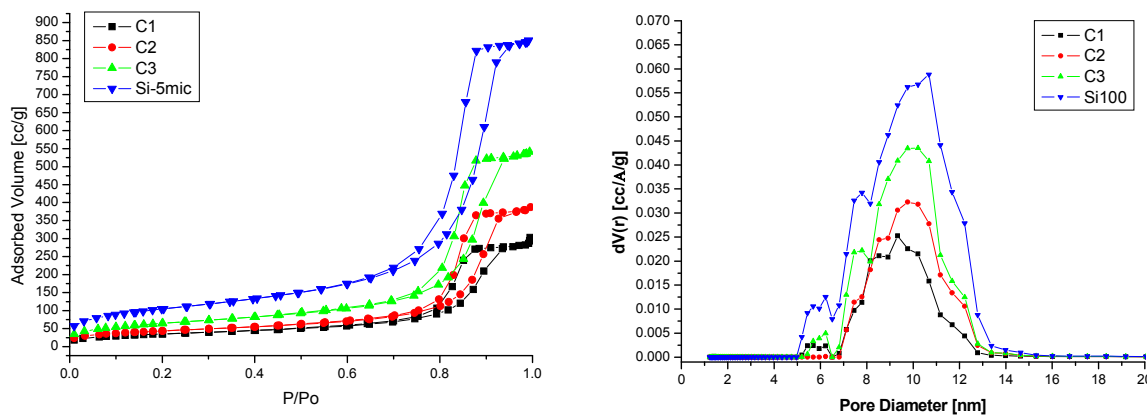


Figure 4.30: Nitrogen adsorption isotherms of amine functionalized cyanamide infiltrated Si-100 mesoporous silica powders, with decreasing carbon nitride loading ($\text{C3} > \text{C2} > \text{C1} > \text{Si100-N}$) and the corresponding pore size distribution (DFT model).

In order to ensure a better penetration of the cyanamide inside the porous silica network, the silica Licospheres Si100 were functionalised with 3- Aminopropyltriethoxysilan (APTES) in order to cover the silica surface with amine functions and to assure a better affinity with cyanamide.^[72]

After the condensation of the cyanamide at 550°C, the powders were red-brown coloured, instead of yellow as for the direct infiltrated samples. From the elemental analysis, it turned out that the graphitic carbon nitride is more carbon rich, most likely due to the excess of carbon introduced by the APTES. The C/N ratios of the resulting powders are around 0.75. Concerning the surface area and the pore volume of the samples, the same behaviour as for the non-functionalised ones is observed with increasing carbon nitride loading. A non proportional decrease to the carbon nitride weight loading in the surface area and the pore volume is observed. This is firstly related to partial pore blocking, as the pores < 6 nm disappear progressively with increasing carbon nitride loading. However, in this case a progressive decrease in the pore size of the bigger mesopores is observed (from 10.7 nm to 9.1 nm), with increasing carbon nitride loading, indicating at least a successful coating formation, facilitated by the amine functionalisation of the pore walls.

4.5 Synthesis of graphitic carbon nitride nanorods and nanotubes

In this section the synthesis of g-C₃N₄ nanorods and nanotubes in porous aluminium oxide membranes as exotemplates is presented. For the rod-like shaping, commercially available aluminium oxide membranes (Anodisc 47), with cylindrical pores and a pore diameter of 200 nm were used. To synthesise the graphitic carbon nitride rods, the Anodisc membrane was infiltrated with molten cyanamide (45°C) and annealed at 550° to induce the thermal condensation into the g-C₃N₄ network.

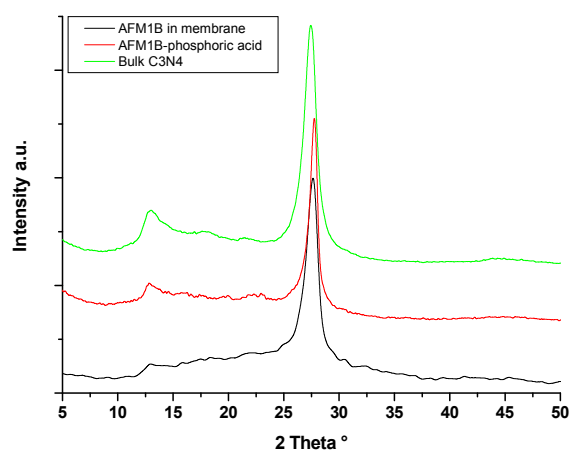


Figure 4.31: X-Ray diffraction pattern of the cyanamide infiltrated membrane calcined at 550°C before and after the removal of the template and of bulk C₃N₄ calcined at 550°C.

Figure 4.31 shows the X-Ray diffraction pattern of the infiltrated calcined membrane before (black curve) and after the removal of the alumina membrane with phosphoric acid (red curve). Before the removal of the template, a broad amorphous background between $10 < 2\theta < 35^\circ$ is observed, corresponding to the contribution of the amorphous alumina membrane. The

graphitic stacking of the carbon nitride network is well developed (peak at $2\theta = 27.6^\circ$, $d = 0.323$ nm). In comparison with the bulk carbon nitride, the graphitic peak is slightly shifted to higher angles (from 27.44° to 27.6°), indicating that the carbon nitride sheets are closer packed in the rod shaped material ($d_{\text{rod}} = 0.323$ nm $<$ $d_{\text{bulk}} = 0.334$ nm) than in the bulk one. The in-plane peak at 13° is less pronounced than in the bulk material, indicating a partial loss of the in-plane order or a smaller extension of the ordered domains. As can be seen in **Figure 4.31**, there is no significant change before and after the removal of the template concerning the crystallinity of the sample, except the fact that the peak at 13° is more developed after the removal of the membrane, due to the disappearance of the scattering background of the alumina membrane. This amorphous background disappears after the etching with phosphoric acid, indicating the successful remove of the template, which was confirmed by TGA (residual mass $<$ 0.2 wt %). In terms of elemental analysis, the composition of the obtained rods, are close to the bulk material, with a C/N ratio of 0.72. SEM measurements (**Figure 4.32**), revealed the rod like shape of the g-C₃N₄ synthesised in the membrane, showing once more that the shape imprinting through the template was successful. The sample is constituted of 200 nm diameter rod like structures of several microns in length. The diameter of the obtained rods is in good agreement with the pore size of the template membrane. From TEM the rod like shape was confirmed. Moreover it was revealed that the rods seem to be constituted of a stacking of plate like structures of around 30 nm in thickness. These plates are not stacked perpendicularly to the rod axis but are tilted by $\sim 20^\circ$. This is confirmed by the SAED measured on isolated rods. The SAED revealed two pairs of large diffraction spots (**Figure 4.32**), indicating that the structure is orientated and which could be attributed to the graphitic and the in-plane peak observed in the X-ray diffractogram.

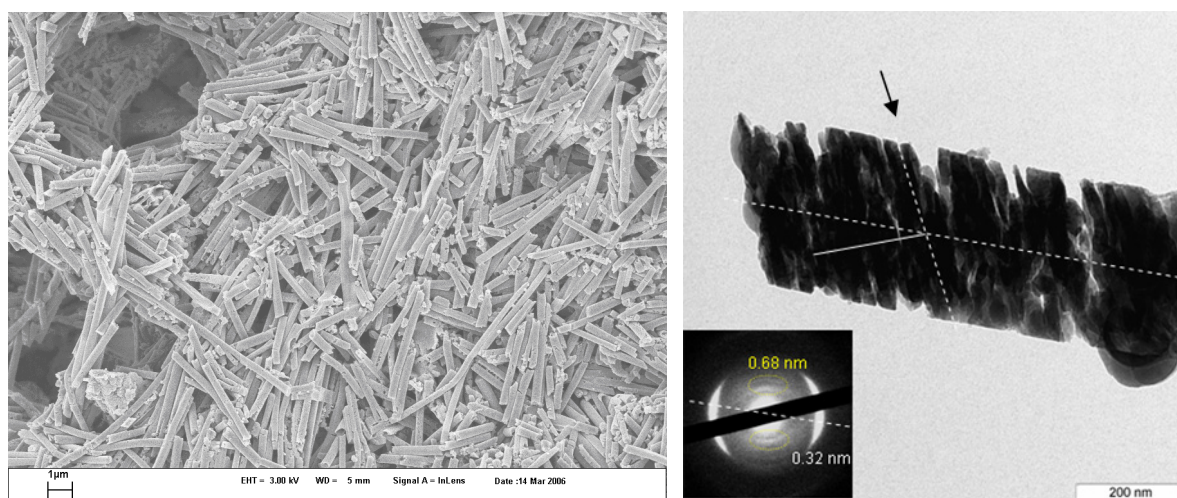


Figure 4.32: SEM and TEM pictures of g-C₃N₄ rods. The inset in the TEM picture represents the diffraction pattern obtained from SAED done on the represented rod.

From the orientation of the diffraction spots at a distance of 0.32 nm, it can be deduced that the graphitic carbon nitride sheets stack parallel to the arrow marked plane, while the in-plane order at 0.68 nm is perpendicular to this stacking direction, which means within the planes.

By following the same synthesis strategy it should be possible, by nanocoating, to synthesise g-C₃N₄ tubes by replacing the molten cyanamide with a dilute aqueous cyanamide solution. From the XRD pattern of the obtained samples (**Figure 4.33**, right) the most important observable change compared with the g-C₃N₄ rods, is the quasi absence of in-plane structure, as depicted by the absence of the peak at $2\theta = 13^\circ$, while the graphitic stacking is perfectly maintained.

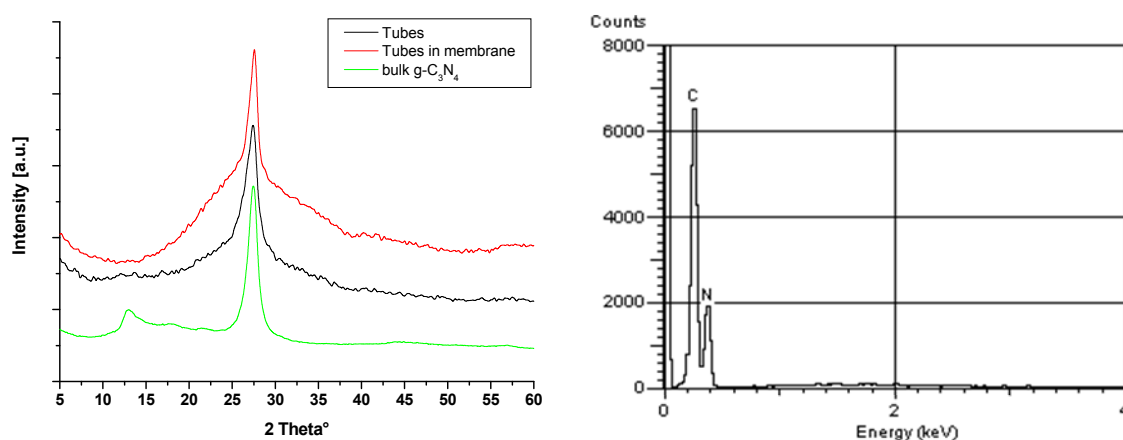


Figure 4.33: Left: XRD diffractograms of g-C₃N₄ tubes in the aluminium oxide membrane and after the removal of the membrane. As a reference the diffractogram of bulk g-C₃N₄ is shown as well. Right: EDX measurements of the tubes after the removal of the aluminium oxide membrane.

From SEM measurements (**Figure 4.34**) tubular structures of 200-250 nm in diameter and several microns in length could be observed, hinting the successful formation of g-C₃N₄ tubes. The dimensions of the obtained tubes correlate well with the pore sizes and the length of the channels in the Anodisc 47 membrane. The removal of the template membrane was confirmed by EDX measurements (**Figure 4.33**, left), since no traces of aluminium or oxygen could be found. The tubes are only composed of C and N with a C/N ratio of 0.74 which is close to the bulk composition and confirms that the tubes are made of g-C₃N₄ related material. From TEM measurements (**Figure 4.34**), it is seen that the tubes have an inner diameter of around 160 nm and a wall thickness of 30 nm. What is remarkable is the smooth surface of the tubes, compared to the rods. SAED (inlet **Figure 4.34**) revealed one pair of large diffraction spots at $d=0.32$ nm corresponding to the graphitic reflex of the carbon nitride network observed in XRD. The structure is oriented and the graphitic periodicity is comparable to the rods, tilted of an angle of $\sim 30^\circ$. The red stripes in **Figure 4.34** show the supposed orientation of the

stacking. There is probably no pronounced in-plane order because the lateral expansion of the stacking sheets is too small to show any periodicity. Complementary HRTEM would have been useful, but unfortunately the tubes were too sensitive to electron beam damage. In conclusion, by using Anodisc membranes as the host template it was possible to synthesis well defined graphitic carbon nitride nano-pipes, proving that graphitic carbon nitride is a versatile material which can sustain a large variety of shape imprinting, while conserving a relative high crystallinity compared to the bulk material.

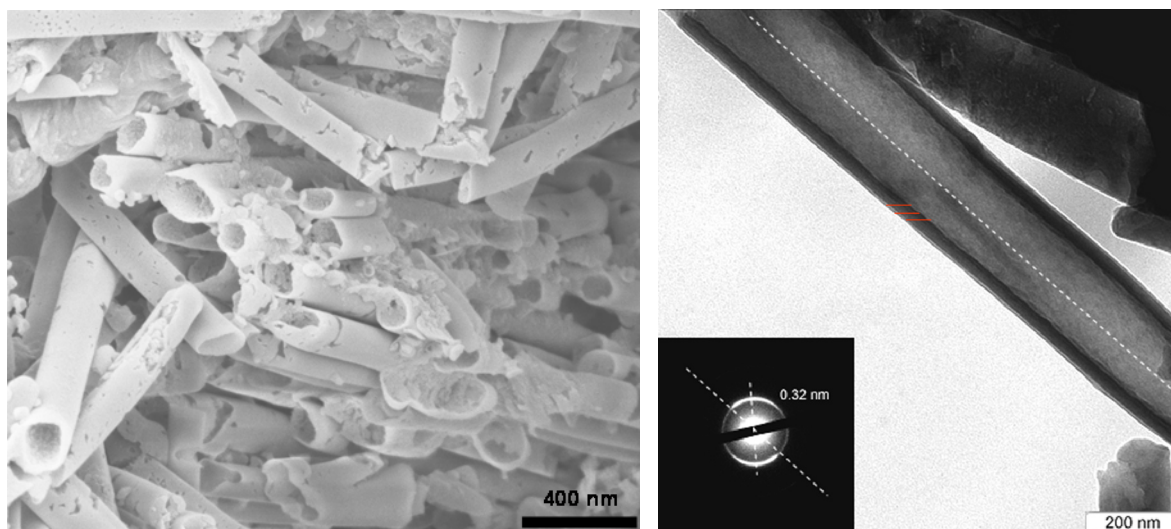


Figure 4.34: SEM (left) and TEM (right) images of graphitic carbon nitride tubes after the removal of the aluminium oxide template membrane.

5 Metal nitride nanostructures through reactive hard templating with graphitic carbon nitrides

5.1 Synthesis of binary metal nitride nanoparticles in a mesoporous graphitic carbon nitride nanoreactor

The synthesis of materials in nano-sized confinements, or “nanoreactors”, is a suitable method for the preparation of nanoparticles. Nanoparticles have been shown to be synthesised in “soft” organic nanoreactors i.e. micelles formed from surfactants^[73] and block copolymers^[74-78], emulsions^[79-81] and gels^[82]. Soft nanoreactors often allow simple purification procedures, as the resulting nanoparticles can be separated from the self-assembled confinement in a non-destructive fashion. On the other hand, the softness of the reactor walls sometimes leads to unpredicted forms and shapes of the resulting nanoparticles. Such a process may also be inapplicable for desirable nanoparticle compositions, due to the complex reactant mixtures present during synthesis, which is especially true for metal nitrides.

Other approaches to the synthesis of nanoparticles used the confinement provided by the pore system of porous solids, mainly silica or alumina. These “hard” nanoreactors or exotemplates^[15, 83] inevitably result in 1:1 replication into nanoparticles, nanowires or even fully replicated mesoporous frameworks, depending on the structure and pore size of the confinement. Using this nanocasting approach nanoparticles of metals^[84], metal oxides^[85-87], sulfides^[88] and nitrides^[89] furthermore carbon nanostructures^[90] and nanoparticles made of high temperature engineering plastics^[91] have been produced. A severe disadvantage of the hard template approach is that isolation of the wanted materials is accompanied by the destruction of the confinement, often by using harmful etching reagents such as hydrofluoric acid. Furthermore, the incorporation of precursors into the confinement has to be ensured, while an adequate pore filling and, if necessary, adequate mixing and stoichiometry of the starting components inside the nanopores is hardly controlled and obeys the statistics of small numbers.

This chapter describes the synthesis of metal nitride nanoparticles in a new type of nano-confined environment, namely the mesoporous graphitic carbon nitride material (mpg-C₃N₄) described in detail in **section 4.1**.^[92] The idea of this approach is to add two significant improvements to reported nanostructure synthesis by exotemplates: First, the reaction-confining matrix is thermally decomposed during synthesis, making an additional removal step of the template obsolete. As shown in **section 1.3.1**, mpg-C₃N₄ is decomposed at temperatures higher than 650°C even under nitrogen. Second the mpg-C₃N₄ template serves as a reagent in

the nanoparticle synthesis by donating an excess of nitrogen during thermal decomposition. Appropriate metal sources in the pores of the carbon nitride are so converted into metal nitride nanoparticles with defined nanoparticle size. Such metal nitride nanoparticles are interesting because of their potential application for example as abrasive materials,^[93] catalysts^[3, 5, 6, 94] or as optoelectronic compounds.^[95] Metal nitrides in general can be produced by the conversion of metals or metal oxides into the corresponding nitride using nitrogen sources, such as ammonia^[8] or hydrazine^[10, 11] at high temperatures. Also the use of carbon nitride as nitrogen source was described^[13, 14, 96, 97] which was achieved by mixing metal oxides or metals together with carbon nitride and subsequent heating in a sealed vacuum to observe the corresponding metal nitrides. Several attempts to nanostructured metal nitrides are also found in the literature. The conversion of metal^[98] and metal oxide nanoparticles^[14, 98-100] or solvothermal synthesis^[101-103] has been shown to generate various nanostructures of metal nitrides with various compositions.

The synthesis of metal nitrides in the pores of mpg-C₃N₄ from corresponding sol-gel oxide precursors represents an effective combination of the described nanoreactor approaches for the generation of nanostructures and nitride synthesis from oxides by nitrogen sources. The synthesis of different crystalline metal nitride nanoparticles is presented in the following, namely titanium nitride (TiN), vanadium nitride (VN) and gallium nitride (GaN). In addition, it will be shown that the described pathway is, due to its simplicity, also applicable for ternary metal nitrides. The nanoreactor, mpg-C₃N₄-1-LHS40, a mesoporous graphitic carbon nitride with 12 nm pores and exhibiting graphitic order in the pore walls was produced as described in **section 4.1**^[92]. A TEM-micrograph of the mpg-C₃N₄-1-LHS40 and its idealised chemical structure is shown in **Figure 5.1**. It is important to note that the observed pore sizes (~12 nm) reflect the diameter of the used silica nanoparticles and is therefore, as shown in **section 4**, easily adjusted just by changing the size of the silica template. If one uses the mesoporous carbon nitride as a reactive exotemplate for the synthesis of metal nitride nanoparticle, one would expect that the resulting morphology, in sense of shape and size, is closely related to the morphology of the used porous network template. The size and polydispersity of the finally observed nitride nanoparticles is therefore closely coupled to the initially used silica particles.

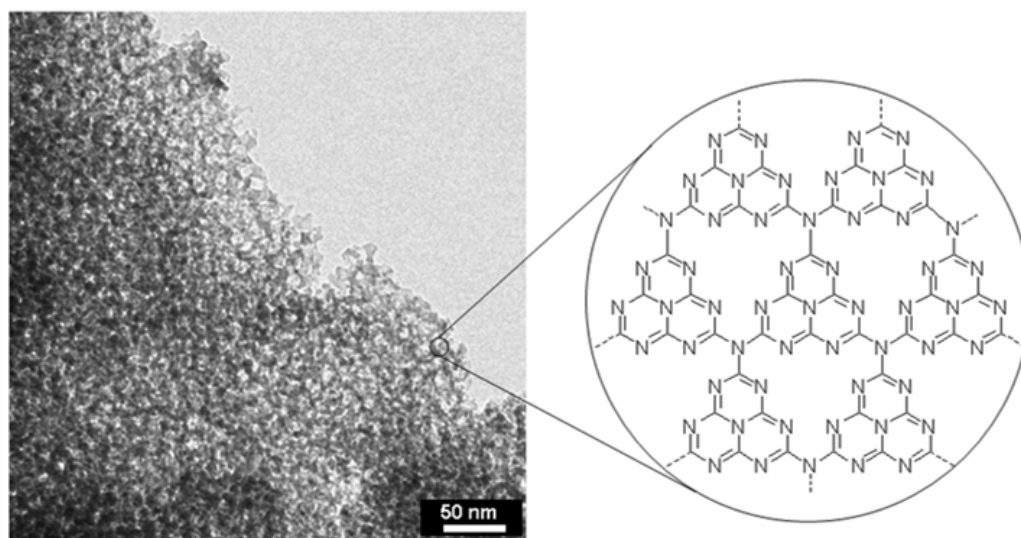


Figure 5.1: TEM micrograph (left side) and idealised chemical structure of the pore walls (right side) of a mesoporous carbon nitride $\text{mpg-C}_3\text{N}_4$ (Silica Ludox HS40/cyanamide mass ratio=1:1; $\text{mpg-C}_3\text{N}_4$ -1-LHS40) used as nanoreactor for the synthesis of metal nitride nanoparticle.

For the synthesis of metal nitride particles, a wet infiltration technique was used. The pores of $\text{mpg-C}_3\text{N}_4$ -1-LHS40 were filled with a solution of the respective sol-gel precursors, by stirring the mesoporous carbon nitride powder in the corresponding precursor solution. After a drying step at 100°C , the resulting composite was annealed under nitrogen atmosphere at 800°C for 3 hours (heating ramp: $3.2^\circ\text{C}/\text{min}$). This annealing procedure was applied for most of the synthesised metal nitrides discussed in this chapter.

5.1.1 Synthesis of titanium nitride nanoparticles

For the synthesis of titanium nitride nanoparticles the pores of $\text{mpg-C}_3\text{N}_4$ 1-LHS40 were filled with a solution of titanium tetrachloride (TiCl_4) in different concentrations in ethanol and dried at 100°C . After the decomposition of the carbon nitride template matrix at 800°C a nanocrystalline TiN powder is obtained (**Figure 5.2**, grey curve). Temperature dependent XRD measurements were carried out for a closer observation of the conversion and crystallization processes involved during the temperature treatment (**Figure 5.2**). The red curve in **Figure 5.2** represents the diffraction pattern of the mesoporous carbon nitride, which displays the typical graphitic and in-plane features of $\text{g-C}_3\text{N}_4$. Incorporation of the metal precursor into the pores of $\text{mpg-C}_3\text{N}_4$ (denoted as “composite”) and subsequent drying leads to a very broad peak at lower angles (around 14°) and to a broad shoulder in the region between 25° and 35° , which is partially overlapping with the graphitic peak of the carbon nitride matrix (black curve, **Figure 5.2**), attributed to an amorphous titania gel confined in the pores.

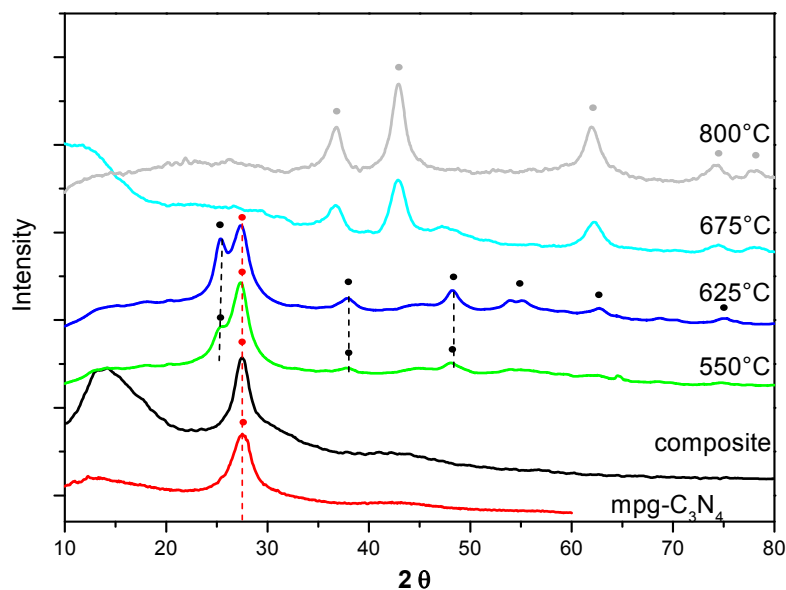


Figure 5.2: Temperature dependent XRD measurements of the titania precursor / mpg-C₃N₄ composites

At 550°C (green curve, **Figure 5.2**), the structural features of the carbon nitride confinement are still intact while the peaks denoted with black spots can be attributed to the diffraction peaks of anatase, indicating the onset of crystallization of titania. At 625°C (blue curve, **Figure 5.2**) the anatase further crystallizes in the pores. The obtained anatase crystallites are very small, indicated by the broadening of the diffraction peaks. The XRD determined crystallite size is around 6 nm. This proves the incorporation of anatase inside the pores, as without confinement sintering would have already occurred at such temperatures, leading to bigger crystallites [104, 105]. At 675°C (turquoise curve, **Figure 5.2**) the graphitic carbon nitride confinement has for the most part decomposed, so that the crystalline structure of the confinement has vanished. This supports the results obtained from TGA measurements, where a decomposition temperature of mpg-C₃N₄ of approx 650°C is noted. The remaining peaks in the diffraction pattern can be attributed to the generation of a cubic titanium nitride, namely osbornite, while the diffraction peaks of anatase have almost disappeared. This shows that the conversion of the titanium oxide into titanium nitride is promoted by the donation of nitrogen to the metal through the decomposition of the carbon nitride template. However at 675°C a broad amorphous peak at low angles indicates the presence of an organic residue. Finally at 800°C (grey curve, **Figure 5.2**) the reaction seems complete, and a pure titanium nitride in terms of phase purity is obtained. The formed TiN is a cubic allotrope of TiN and crystallizes in the space group $Fm\bar{3}m$ with the following cell parameters: $a = b = c = 4.233 \text{ \AA}$ and $\alpha = \beta = \gamma = 90^\circ$, which are in good agreement with the data reported in the literature.[106, 107] The composition of the powder was determined by combustion elemental analysis. It has to be noticed that even if the reactivity of the as synthesised TiN toward oxygen is enhanced due to

its nanoparticulate structure (see below) an incomplete combustion cannot be totally excluded, so that the nitrogen amount of the samples is probably slightly underestimated. The composition of the powder was determined to be $\text{TiN}_{0.95}$. Beside nitrogen, up to 30 weight % of residual carbon could be detected in the sample. However it was assumed that the carbon is not incorporated in the inorganic phase, in form of TiC or $\text{Ti}(\text{CN})$, but present as amorphous carbon in the sample, since it is known from literature that TiN is formed from the reaction in similar conditions between anatase nanoparticles and carbon nitride nitrogen donors, such as melamine^[108] or cyanamide,^[109] This is supported by the XRD results. First TiC and TiC_xN_y have bigger cell parameters than TiN ($\text{TiC}_{0.981}$, $Fm\bar{3}m$, $a = 4.327 \text{ \AA}$ ^[110], $\text{TiC}_{0.5}\text{N}_{0.5}$, $Fm\bar{3}m$, $a = 4.286 \text{ \AA}$ ^[111]) and second no peaks related to any crystalline carbon could be detected in XRD. Moreover the preferred formation of TiN rather than TiC is additionally supported by the fact that TiN is thermodynamically more stable than TiC ($\Delta fG_{\text{solid}(\text{TiC})}^0 = -191.29 \text{ kJ/mol} < \Delta fG_{\text{solid}(\text{TiN})}^0 = -346.65 \text{ kJ/mol}$ ^[112]). However minor carbon incorporation in the structure can not be completely excluded. The broadness of the peaks in the XRD pattern of the obtained TiN powder indicates that the powder is nanocrystalline, which was confirmed by HRTEM. As can be seen in **Figure 5.3**, highly crystalline nanoparticles of appreciatively 5 nm are observed. The Fast Fourier transform (FFT) of the marked area exhibits two diffraction spots at a distance of 0.211 nm, which is in a good agreement with the (200) lattice distance of TiN . To rule out the nitrogen from the gas flow as nitrogen source, the same annealing treatment was carried out in a evacuated and sealed quartz ampoule yielding the same nanocrystalline TiN powder, proving that the nitrogen source is indeed the carbon nitride matrix.

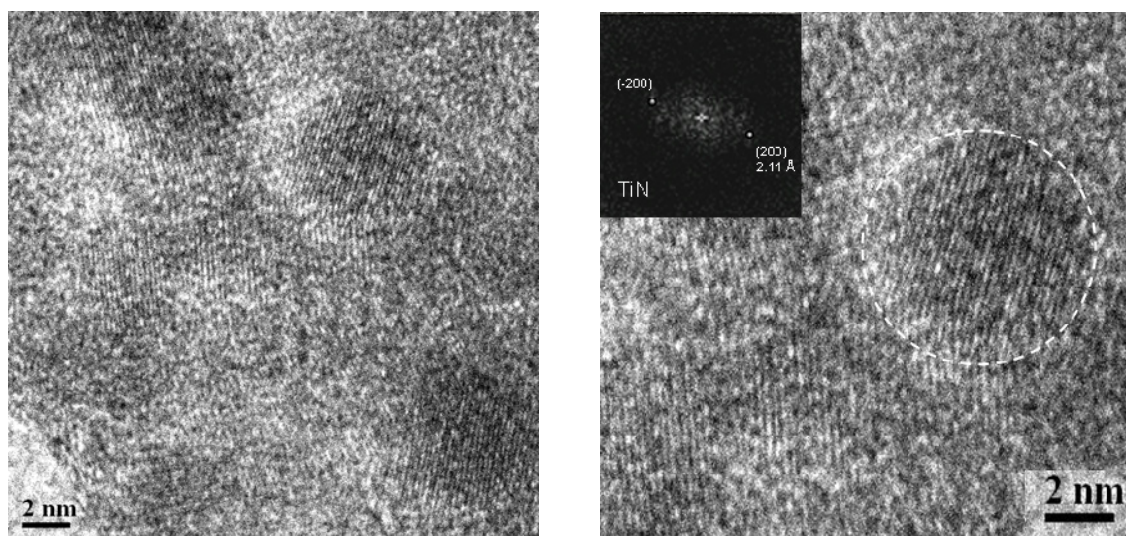


Figure 5.3: HRTEM micrographs of TiN nanoparticles made in $\text{mpg-C}_3\text{N}_4\text{-1-LHS40}$ at 800°C .

The mpg- C_3N_4 nanoreactor approach conceptually implies the possibility of being able to confine different amount of metal precursor molecules in the pores, which should yield in different particle sizes. Thus precursor solutions with different concentrations were used to infiltrate the mpg- C_3N_4 . **Figure 5.4** and **Figure 5.5** show the X-ray diffraction pattern and the TEM micrographs with the corresponding SAED of two samples infiltrated with titania precursor solutions of different concentrations. It can be seen that in both cases nanoparticles with narrow dispersity are formed, while the diffraction patterns indicate the formation of titanium nitride. For the higher concentration (2.5 g $TiCl_4$ in 2.0 g ethanol) the average particle size obtained from TEM micrographs and XRD measurements are 7.1 nm and 6.9 nm, respectively. For more diluted precursor solutions (1.5 g $TiCl_4$ in 2.0 g ethanol), smaller TiN particles of 5.6 nm (TEM) and 4.8 nm (XRD) are observed. This proves that the nanoreactor approach allows a “fine tuning” of the nanoparticle size, by simply using differently concentrated precursor solutions, resulting in different filling rates of the nanoreactor.

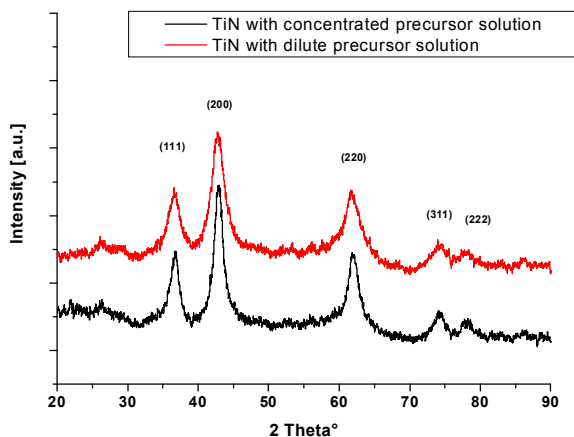


Figure 5.4: XRD powder diffraction pattern of TiN nanoparticles synthesized in mpg- C_3N_4 -1-LHS40 infiltrated with a dilute (---) and a concentrated (---) titanium precursor solution.

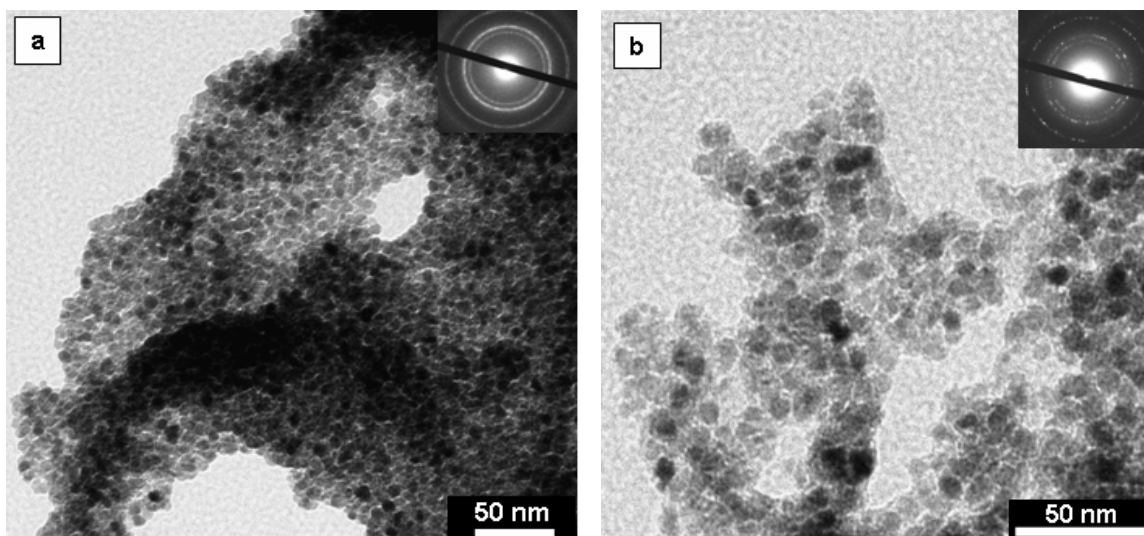


Figure 5.5: TEM micrographs of TiN nanoparticles synthesized in mpg- C_3N_4 -1-LHS40 with (a) dilute and (b) concentrated titanium precursor solution.

Beside the concentration of the precursor solution, it was shown that the synthesis temperature has an influence on the crystallite size. Three samples infiltrated with the same precursor solution of fixed concentration (1.5 g TiCl_4 in 2.0 g ethanol) were annealed at different temperatures, namely 700°C, 800°C and 900°C. For all the samples, the heating rate was fixed at 3.2 °C/min and they were annealed for 3 hours at the given temperature. As can be seen from the XRD diffractograms in **Figure 5.6**, the broadness of the diffraction peaks is decreasing with increasing annealing temperature, due to an enhanced crystallinity. The size of the TiN crystallites estimated by XRD (Scherrer equation **Equ. 2.12**) increases from 3.4 nm (700 °C), to 4.8 nm (800 °C) to reach a crystallite size of 5.7 nm at 900°C. This behaviour of crystallite growing is known for TiN nanoparticles synthesised at high temperature.^[113]

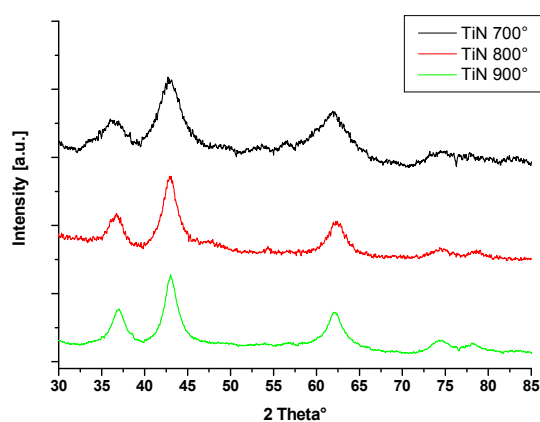


Figure 5.6: XRD pattern of TiN synthesised in mpg- C_3N_4 -1-LHS40 annealed at 700°C (---), 800°C (---) and 900°C (---).

Finally the size of the nanoreactor should certainly influence the size of the resulting particles in this reactive templating approach. Therefore two mesoporous graphitic carbon nitrides with different pore sizes were used as nanoreactors. A mpg- C_3N_4 -1-LHS40 powder with 12 nm pores and a mpg- C_3N_4 -1.1-LTMA powder with 23 nm pores (see chapter 3) were infiltrated with a concentrated titanium precursor solution ($\text{TiCl}_4/\text{EtOH}$: 2.5g/2g). After annealing at 800°C the resulting black powders were investigated concerning their crystallinity. Both samples (**Figure 5.7**) are composed of TiN. The difference in broadness of the diffraction peaks between the XRD diffractograms of the TiN powder synthesised in the mesoporous C_3N_4 with small and big pores already indicates the successful synthesis of different particle sizes. In fact the crystallite size, determined from XRD (Scherrer equation) and from TEM (**Figure 5.8**) of the TiN-LHS40 powder was determined to be around 6.9 nm and 7.1 nm respectively, as already mentioned above, whereas the crystallite size of the TiN-LTMA powder was estimated to 13.5 nm and 15 nm respectively. Those results suggest that the TiN particle size and shape is indeed imprinted by the C_3N_4 nano-confinement, allowing the control of the particle size of the resulting TiN through the control of the pore size of the C_3N_4 nanoreactor.

It can be concluded that mpg- C_3N_4 is a suitable exotemplate for the synthesis of highly crystalline TiN nanoparticles through nanocasting. First it is a suitable nitrogen source allowing through its thermal decomposition the conversion of a titanium oxide precursor sol into highly crystalline cubic TiN. Second it acts as a template for the formation of well defined and highly crystalline nanoparticles. The particle size can be controlled by the precursor concentration and the annealing temperature as well as by the size of the pores of the mpg- C_3N_4 material.

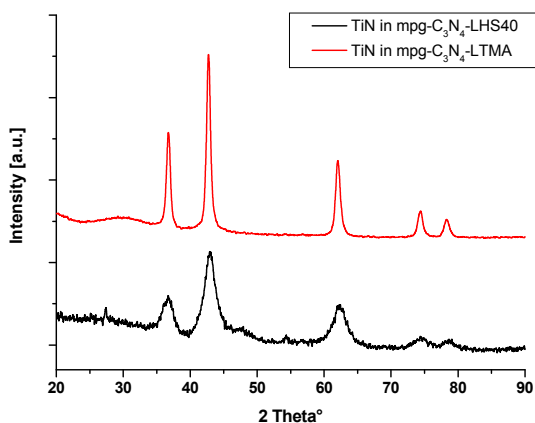


Figure 5.7: X-Ray diffraction pattern of a TiN powder synthesised in a mesoporous C_3N_4 with 12 nm pores (---) and of a TiN powder synthesized in a mesoporous C_3N_4 with 24 nm pores (---). Both C_3N_4 powders were infiltrated with the same precursor solution.

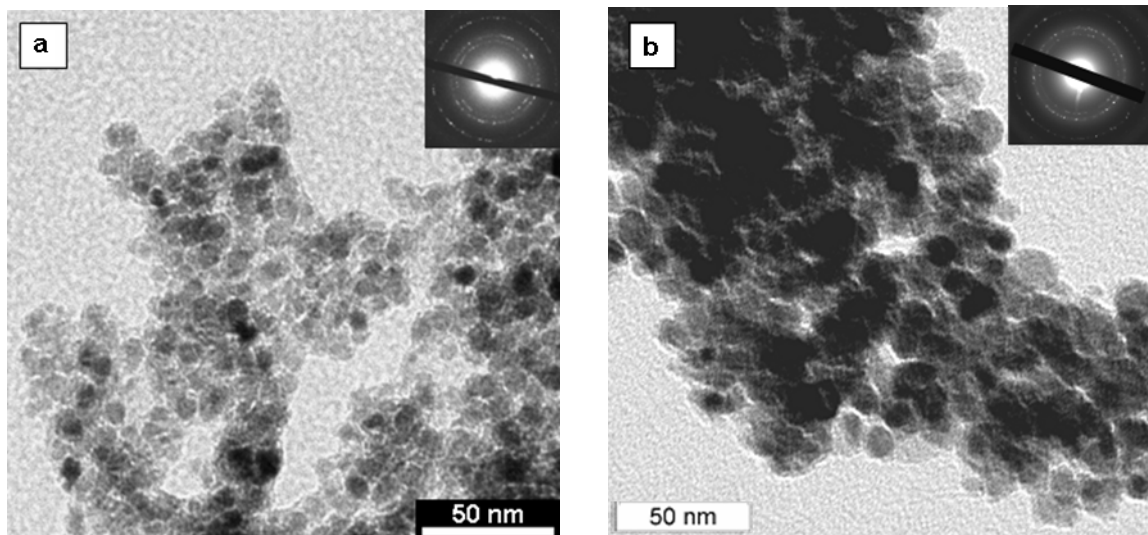


Figure 5.8: TEM micrographs and SAED of TiN nanoparticles made in mpg- C_3N_4 -LHS40 with small pores (a) and in mpg- C_3N_4 -LTMA big pores(b).

5.1.2 Synthesis of vanadium and gallium nitride nanoparticles

In order to show that the synthesis strategy based on the use of graphitic carbon nitride nanoreactors is a quite general route toward the synthesis of binary metal nitride nanoparticle, other metal precursors were used. VOCl_3 and GaCl_3 were utilised as precursor for the synthesis of vanadium nitride and gallium nitride nanoparticles respectively. For both systems, the mesoporous mpg- C_3N_4 -1-LHS40 powder with 12 nm pores, as in the case of titanium nitride, was infiltrated with a dilute precursor solution [$\text{MCl}_n/\text{EtOH} : 1.5\text{g}/2\text{g}$] and a concentrated precursor solution [$\text{MCl}_n/\text{EtOH} : 2.5\text{g}/2\text{g}$]. In both cases, as proved by XRD, the corresponding metal nitride was obtained.

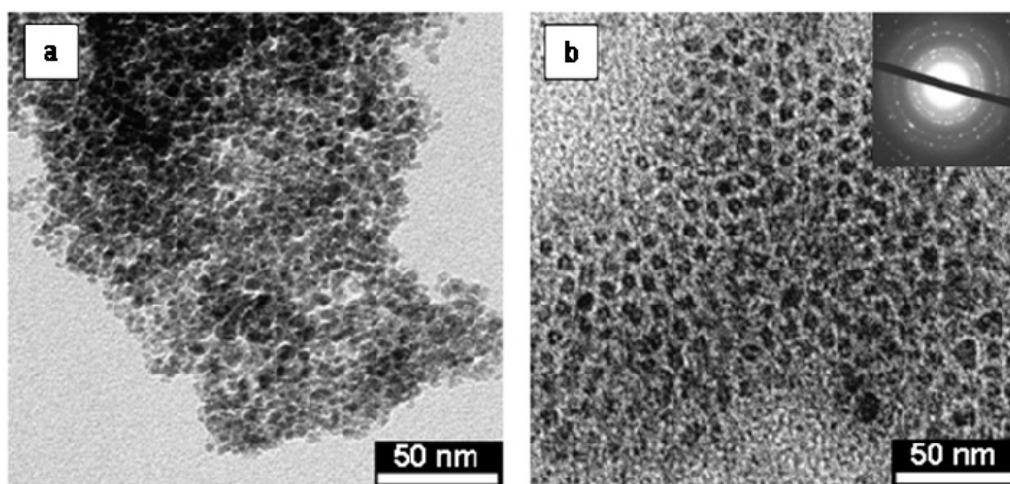


Figure 5.9: TEM micrographs of vanadium nitride nanoparticles obtained from (a) diluted and (b) concentrated precursor solutions.

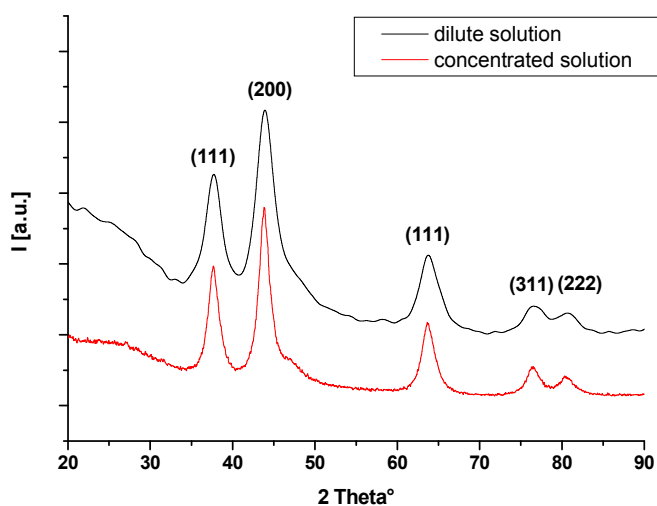


Figure 5.10: X Ray diffraction pattern of vanadium nitride nanoparticles obtained from diluted (---) and concentrated (---) precursor solutions.

Figure 5.9 and **Figure 5.10** shows the TEM micrographs and the X-ray diffraction patterns respectively of vanadium nitride nanoparticles obtained from mesoporous g-C₃N₄-1-LHS40 S powders infiltrated with precursor solution of different concentration and annealed at 800°C under nitrogen atmosphere. The XRD pattern could be indexed according to a cubic vanadium nitride crystallizing in the space group $Fm\bar{3}m$, with the following cell parameters:

$a = b = c = 4.130 \text{ \AA}$ and $\alpha = \beta = \gamma = 90^\circ$, which are in good agreement with the data reported in literature [114, 115]. As for the case of titanium nitride, the formation of a carbide or a carbon rich carbo-nitride phase was excluded, since the reported cell parameters for cubic vanadium carbide and carbo-nitride phases with the same crystal structure are around 4.17 \AA and even higher values are reported [116, 117]. Moreover Zhao *et al.* reported the synthesis of VN nanoparticles through the transformation of vanadium oxide nanoparticles in the presence of g-C₃N₄ at high temperature [96]. The nitrogen content of the samples was determined by elemental analysis. An average value of 12 weight % was measured. Similar to the titanium nitride samples, amorphous carbon (around 34 weight %) a side product of the reaction could be detected, forming a sort of matrix around the particles. The composition of the vanadium nitride phase was estimated to be around VN_{0.85}. Again, the incorporation of some carbon impurities in the crystal structure can not be totally excluded. Concerning the particle size, as already observed for titanium nitride, more concentrated precursor solutions yielded bigger nanoparticles of 6.9 nm in diameter, while lower concentration again reduced the particle size to 5.5 nm (sizes determined by TEM). The vanadium nitride nanoparticles are highly crystalline, as evidenced by the SAED in **Figure 5.10** and by the HRTEM micrograph shown in **Figure 5.11**.

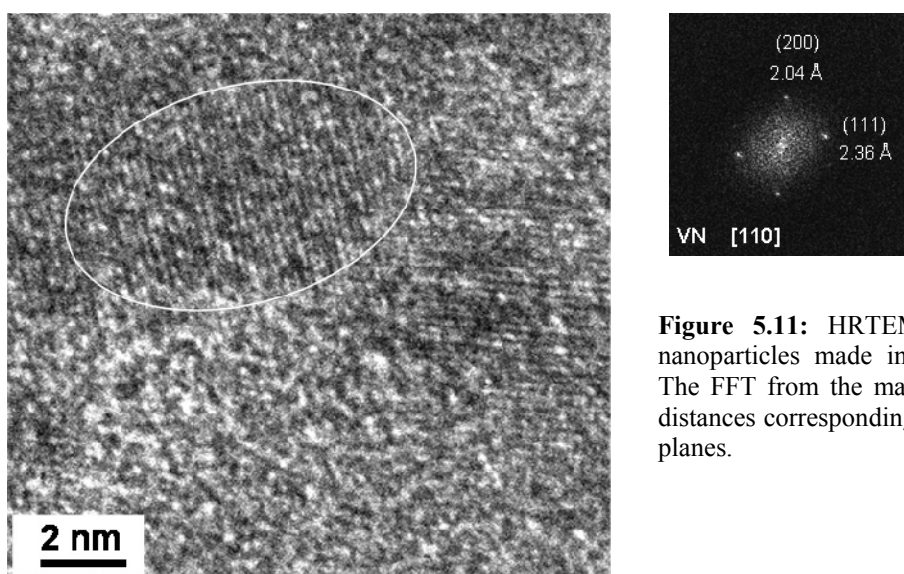


Figure 5.11: HRTEM micrograph of VN nanoparticles made in the dilute conditions. The FFT from the marked area shows lattice distances corresponding to the (111) and (200) planes.

The diffraction rings observed in the SAED could be fully indexed in good agreement with the powder diffraction pattern. Well developed lattice fringes are observed in the HRTEM. The FFT from the marked area reveals two lattice distances $d = 2.36 \text{ \AA}$ corresponding to the lattice distance between the (111) planes and $d = 2.04 \text{ \AA}$ corresponding to the lattice distance between the (200) planes of cubic vanadium nitride. The crystallite sizes determined with the Scherrer equation applied to the (111) peak were in good agreement with the particle sizes determined by TEM (concentrated: TEM:6.9 nm / XRD: 6.1 nm; dilute: TEM:5.5 nm / XRD: 4.9 nm).

Similar results were obtained in the case of gallium nitride nanoparticles. The obtained powders were highly crystalline and only gallium nitride could be detected in the XRD pattern, as shown in **Figure 5.12**. The diffraction pattern could be indexed according to GaN with hexagonal symmetry (wurtzite structure), crystallizing in the space group $P63mc$ with the following cell parameters: $a = b = 3.189 \text{ \AA}$, $c = 5.184 \text{ \AA}$ and $\alpha = \beta = 90^\circ$, $\gamma = 120^\circ$.^[118, 119] The composition of the powder was determined to be $\text{GaN}_{0.85}$. However in contrast to the TiN and VN systems described above no carbon residue could be detected in the samples. As already observed in the case of TiN and VN, the control of the particle/crystallite size was achieved by the concentration of the precursor solution, as shown by the broadening of the X-Ray diffraction peaks in **Figure 5.12** and by TEM measurements, shown in **Figure 5.13**. For the concentrated solution, particles of 9.1 nm, whereas particles of 6.7 nm were obtained for the dilute solutions. This was confirmed both by XRD and TEM. The crystallinity of the obtained particles was confirmed by HRTEM, as shown in **Figure 5.14**. The measured lattice distance $d = 2.74 \text{ \AA}$ was in good agreement with the expected lattice distance $d_{100} = 2.75 \text{ \AA}$ of hexagonal GaN. As a result, highly crystalline pure GaN nanoparticles in terms of phase and chemical purity could be obtained, by using this synthetic strategy.

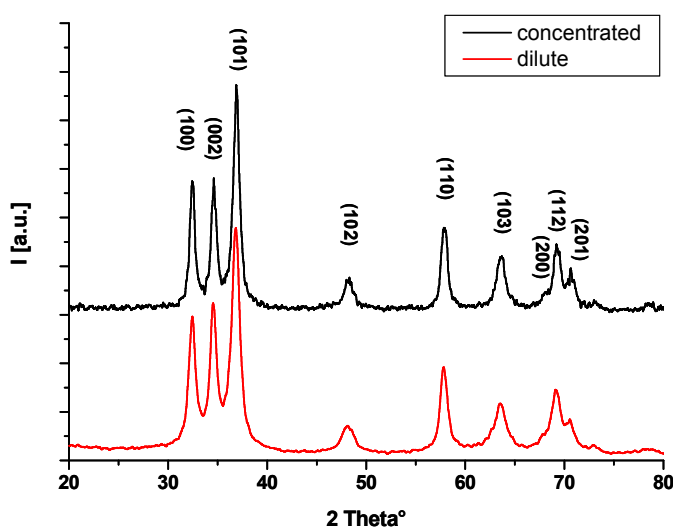


Figure 5.12: X Ray diffraction pattern from gallium nitride nanoparticles obtained from diluted (---) and concentrated (---) precursor solutions.

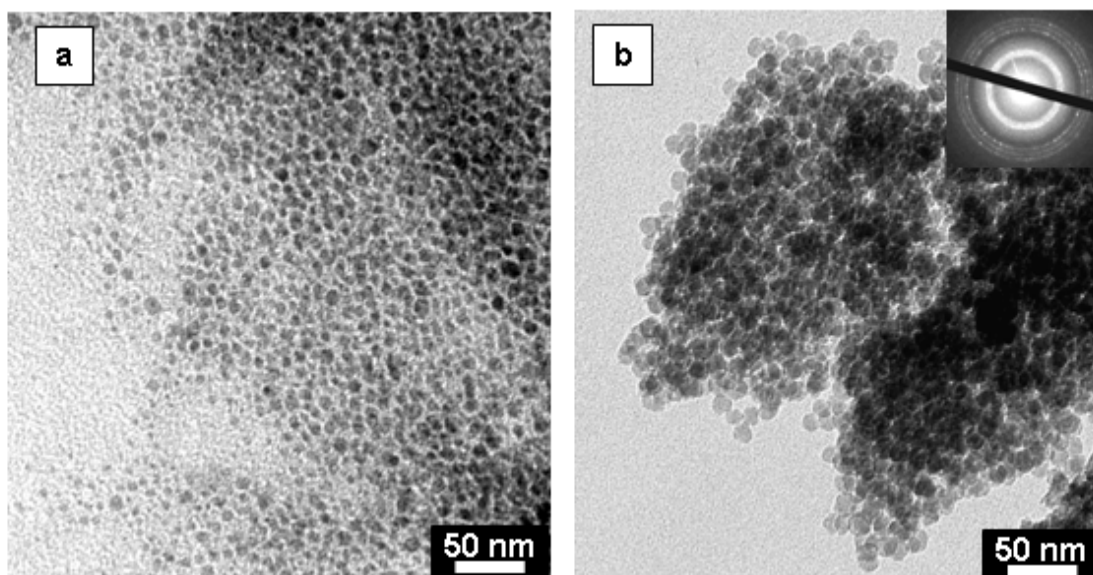


Figure 5.13: TEM micrographs from gallium nitride nanoparticles obtained from (a) diluted and (b) concentrated precursor solutions. The inset represents the SAED which could be indexed according to the powder X-ray diffraction pattern.

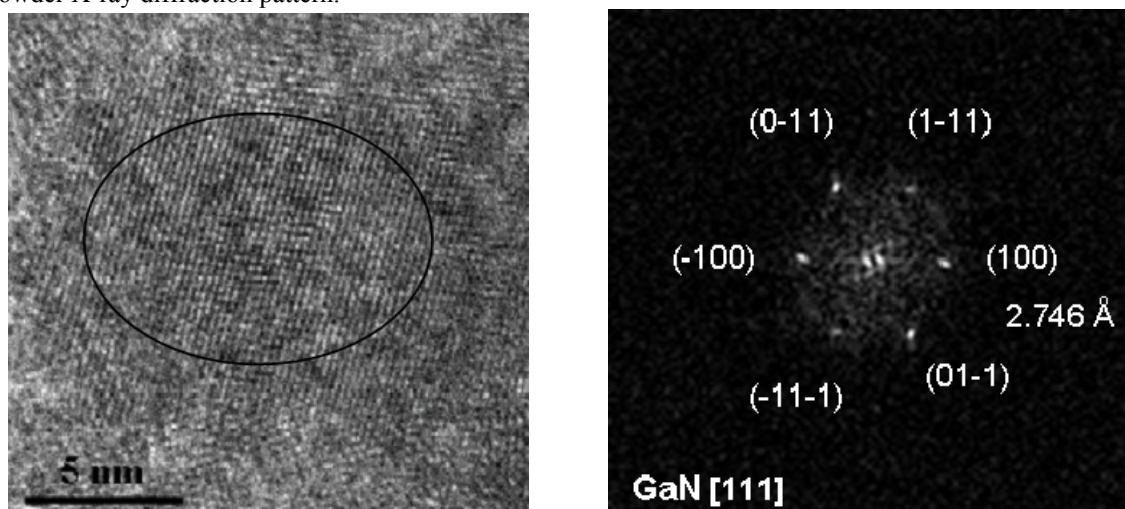


Figure 5.14: HRTEM micrograph of GaN nanoparticles made in the concentrated conditions. The FFT from the marked area shows lattice distances corresponding to the (100) planes. The observed particle is oriented along the [111] zone axis.

To conclude, it was shown that in addition to its ability to act as confinement for the synthesis of nearly spherical metal nitride nanoparticles, acting both as exotemplate and nitrogen donor reagent, mesoporous $g\text{-C}_3\text{N}_4$ is a powerful “nanoreactor” for the synthesis of a multitude of metal nitrides, illustrated by the fact that TiN, VN and also GaN nanoparticles could be synthesised.

5.1.3 Synthesis of ternary metal nitride nanoparticles in a mesoporous graphitic carbon nitride nanoreactor

The previous section has demonstrated that it is possible to use mpg-C₃N₄-LHS40 powders as a “nanoreactor” for the synthesis of a large variety of binary metal nitride nanoparticles, such as TiN, VN and GaN. Nowadays for a lot of applications ternary nitrides are also needed. For example for the fabrication of the light emitting diodes operating in the blue to ultraviolet region, or for blue semiconductor lasers, ternary metal nitride alloys such as Al_xGa_{1-x}N are of high interest.^[120, 121] By changing the content of aluminum in the alloy, the band gap can be adjusted between 3.4 eV for pure GaN and 6.2 eV for pure AlN.^[122] The major part of the synthetic approaches toward such nitride alloys is based on metalorganic vapor phase epitaxy (MOVPE) or molecular beam epitaxy (MBE), resulting mainly in the formation of thin films.^[122] On the other hand for mechanical hardness properties,^[123] for potential application in catalysis and as electrode material for super capacitors,^[113] V_xTi_{1-x}N alloys represent another system of high interest. Conceptually, it was shown previously that mpg-C₃N₄-LHS40 is an appropriate nanoreactor for the synthesis of binary metal nitride nanoparticles, through an easy infiltration technique. It was thus an interesting point to investigate if by taking advantage of the induced nanoconfinement, the synthesis of ternary metal nitrides nanoparticles, in the here presented case of AlGa_xN and TiVN, is possible by a simple infiltration of precursor solutions, containing the two corresponding metal sources.

5.1.3.1 Synthesis of AlGa_xN nanoparticles in mesoporous graphitic carbon nitride.

The first investigated system was the synthesis and characterization of AlGa_xN nanoparticles. The synthetic approach is similar to this described for the binary metal nitrides, with the only difference that mixed precursor solutions containing the respective metals were used. Accordingly, in the case of AlGa_xN nanoparticles, AlCl₃ and GaCl₃ were used as precursors. Different solutions with variable Al/Ga molar ratios were used to infiltrate the mpg-C₃N₄-LHS40 which should principally yield in (AlGa)_xN alloy nanoparticles with different compositions. The exact composition of the used precursor solution is given in **Table 5.1**.

Sample	AlCl ₃ [mg]	GaCl ₃ [mg]	EtOH [g]	Al/Ga mol ratio
AF117-0.16	110	730	2	0.20
AF117-0.35	290	530	2	0.72
AF117-0.59	397	360	2	1.46

Table 5.1: Composition of the infiltrating solutions for the synthesis of AlGa_xN nanoparticles in mpg-C₃N₄-LHS40

The infiltrated mpg-C₃N₄-1-LHS40 powders were heated to 800°C under nitrogen flow, as described for the synthesis of pure GaN nanoparticle. After the samples were completely cooled down to room temperature in the oven under nitrogen atmosphere, three powders were obtained, from yellow grey to light grey in color. The composition of the powders was determined with EDX, EA and ICP (inductively coupled plasma atomic spectroscopy) measurements. The EDX measurements in **Figure 5.15** illustrate the increasing Al content of the resulting powders, as the Al concentration is increased in the precursor solution. To have a quantitative estimation of the aluminum and gallium content in the samples, complementary ICP measurements, which are more precise than EDX measurements, especially on powders, were performed. **Table 5.2** gives the composition of the obtained powders. The carbon and nitrogen content of the powders was determined with elemental analysis and compared with the EDX results. The trend of increasing aluminum content in the samples as measured by EDX, was confirmed by ICP. The powders exhibit comparable Al/Ga molar ratios than the corresponding precursor solution. From EDX measurements only traces of oxygen could be detected, indicating that only minor surface oxidation occurs. Remarkably no carbon contamination is found in the powders as confirmed both by EA and EDX. Interestingly, the more aluminum is incorporated in the sample, the less nitrogen rich they are.

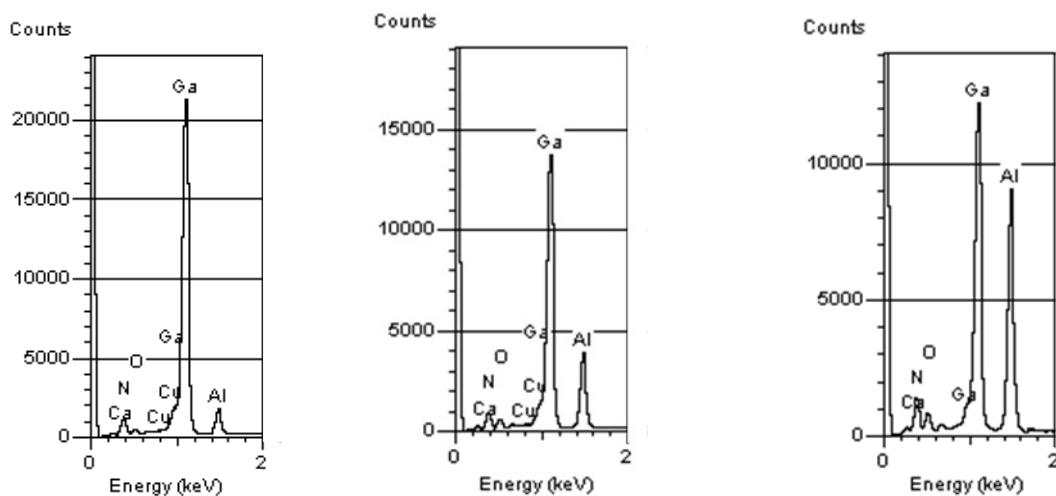


Figure 5.15: EDX measurements from the AlGa_xN nanoparticles. From the left to the right: sample AF117-0.16, AF117-0.35 and AF117-0.59 respectively.

Sample	Al wt%	Ga wt%	N Wt%	C wt%	O wt%	Al/Ga mol. ratio powder	Al/Ga mol ratio solution	Al _x Ga _y N _z O _m
AF117-0.16	6.41	72.81	15.28	0	0.76	0.22	0.20	Al _{0.18} Ga _{0.82} N _{0.84} O _{0.04}
AF117-0.35	14.33	67.47	15.17	0	1.2	0.79	0.72	Al _{0.44} Ga _{0.56} N _{0.55} O _{0.08}
AF117-0.59	28.68	52.03	15.02	0	0.88	1.42	1.43	Al _{0.67} Ga _{0.41} N _{0.6} O _{0.03}

Table 5.2: Composition of the different AlGa_xN nano crystalline powders with increasing Al content.

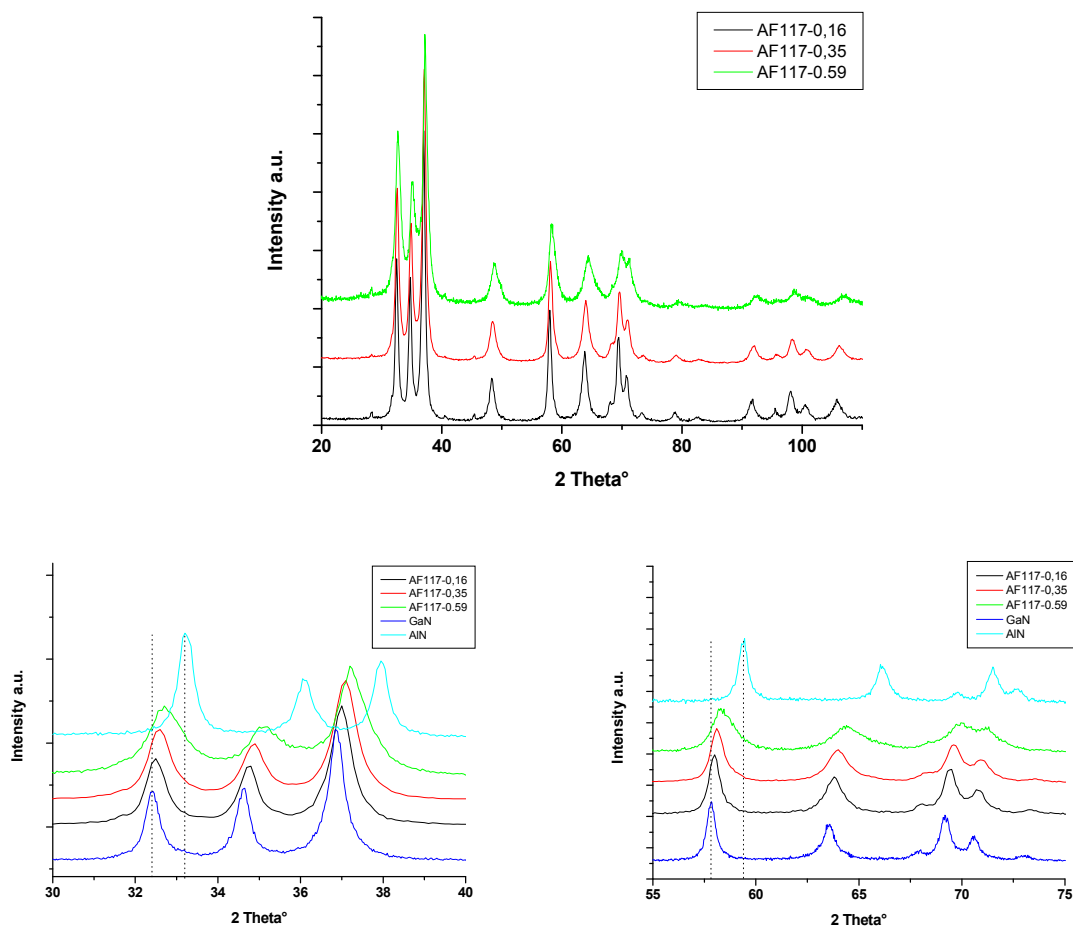


Figure 5.16: a) Powder X-ray diffraction pattern of the AlGaN nano crystalline powders with increasing aluminium content. As a reference the pattern of pure GaN and AlN synthesised in the same conditions are presented in the zooms b) and c).

The crystallinity of the samples was investigated with X-ray diffraction. The diffraction patterns are shown in **Figure 5.16**. Remarkable is the fact that the X-ray patterns shift from lower angles, e.g. from the pattern of pure GaN, to higher angles, e.g. toward the pattern of pure AlN, when the aluminum content increases in the powders. This indicates the formation of a solid solution, where aluminum atoms progressively substitute gallium atoms in the crystal cell. All three samples exhibit diffraction pattern with hexagonal symmetry and crystallize in the space group $P63mc$. The cell parameters for each sample and those of pure GaN and AlN are listed in **Table 5.3**. The Scherrer equation was applied to the (102) and the (110) peaks to determine an average crystal size for each sample. The most intensive peak, namely the (101) could not be used to determine the crystallite size, since it overlaps with the adjacent (002) peak. The calculated crystal size decreases from approximately 10 nm to 6 nm with increasing aluminum content.

Sample	Peak position 2 θ [°]						Cell parameter [Å] P63mc		Cryst. size XRD	Particle size TEM
	(100)	(002)	(101)	(102)	(110)	(103)	a	c		
GaN	32.42	34.60	36.88	48.14	57.83	63.51	3.189	5.184	9.1	9.0
	2.76 Å									
AF117-0.16	32.51	34.77	37.00	48.35	58.02	63.80	3.179	5.16	9.6	9.2
	2.75 Å									
AF117-0.35	32.58	34.92	37.1	48.5	58.14	64.06	3.173	5.138	7.5	7.4
	2.74 Å									
AF117-0.59	32.71	35.12	37.23	48.75	58.31	64.45	3.165	5.105	5.9	4.2
	2.73 Å									
AlN	33.22	36.08	37.94	49.85	59.36	66.1	3.112	4.975	9.5	-
	2.70 Å									

Table 5.3: Exact diffraction peak positions, cell parameters and crystallite size of $(\text{Al}_x\text{Ga}_y)\text{N}_z$ nanocrystalline samples with increasing aluminium content.

However although the broadness of the reflection peaks is related to the crystal size, it is also determined by the quality of the crystal structure. This means that a progressive peak broadening could also reflect a loss in crystallinity due to an increasing number of defects when the aluminum content is increased. The size and shape of the particles was investigated by TEM. To obtain a good dispersion of the particles and avoid aggregation, the powder was mortared and dispersed in THF. One drop of oleic acid was added and the dispersion was sonicated for several minutes with a high power ultra sonication tip. One drop of the dispersion was deposited on a carbon coated copper grid and left to dry. The TEM images in **Figure 5.17**, illustrate that the powders consist of small nanoparticles, confirming the results obtained from the X-Ray diffraction. A mean particle size could also be determined for each sample from the TEM measurements. The particle size determined by TEM correlates with the crystallite size determined with the Scherrer equation, as shown in **Table 5.3**.

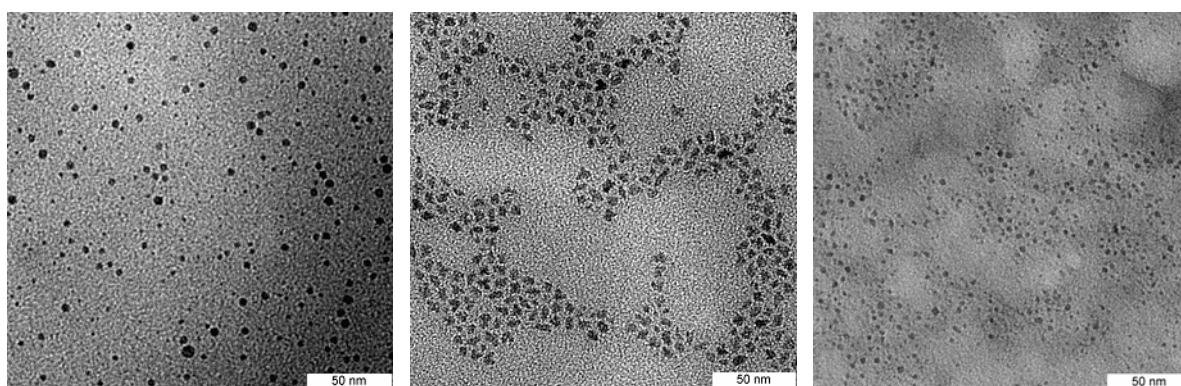


Figure 5.17: TEM micrographs of the sample AF117-0.16, AF117-0.35 and AF117-0.59 with increasing aluminium content from the left to the right respectively.

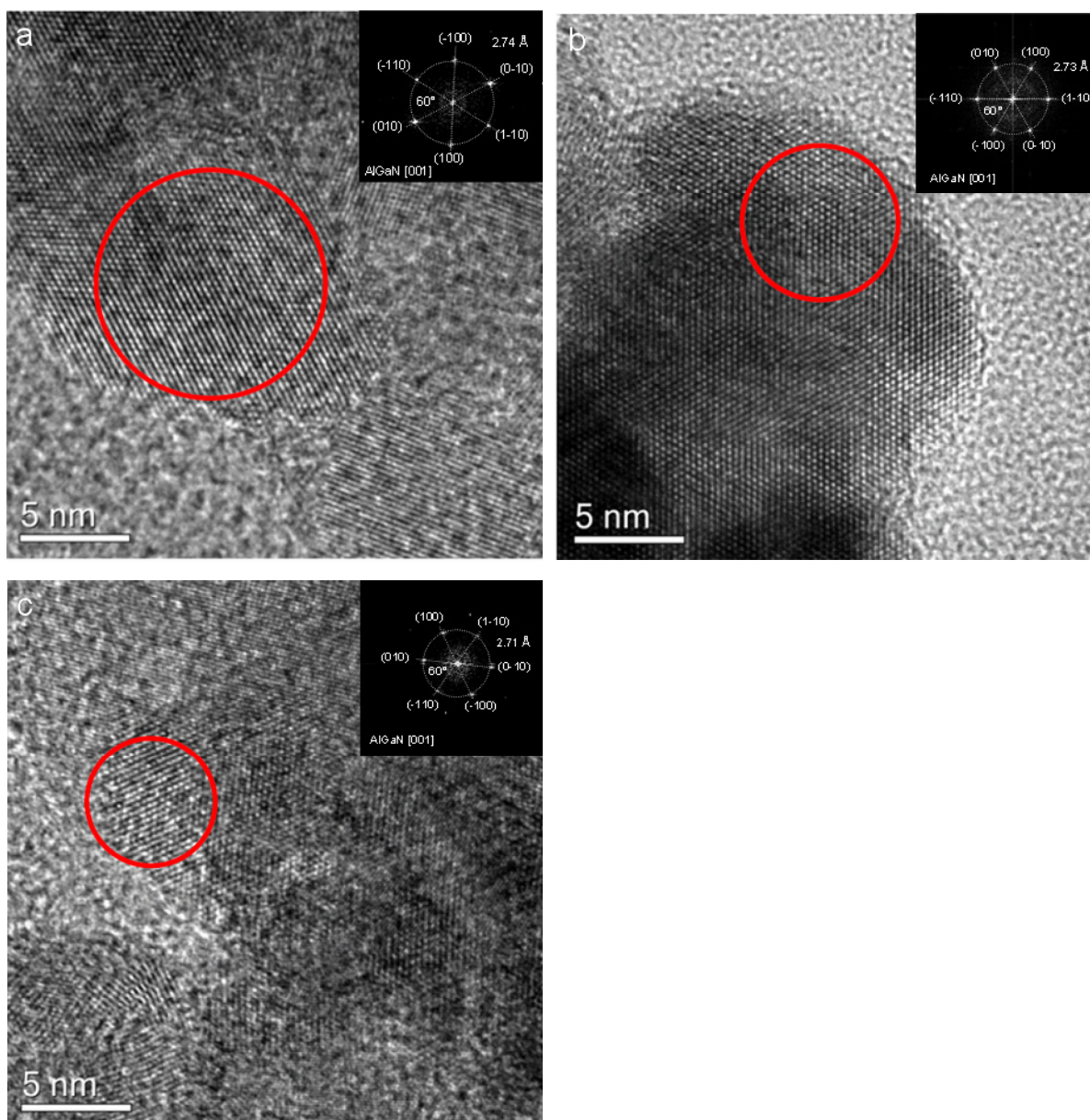


Figure 5.18: HRTEM micrographs of the AlGaIn samples a) AF117-0.16 b) AF117-0.35 c) AF117-0.59 with increasing aluminium content. The insets represent the indexed FFT of the areas delimited with red circles.

In order to investigate the crystallinity on the nanometre scale, complementary HRTEM measurements were performed by Dr Jens-Oliver Müller from the Inorganic Department of the Fritz-Haber Institute (Berlin). As can be seen in **Figure 5.18**, all the samples exhibit highly crystalline nanoparticles, as highlighted by the presence of well defined lattice fringes. To ensure an accurate comparison between the lattice distances in the three samples, care was taken to measure the lattice distances on particles which are oriented in the same way. Here particles oriented along the [001] zone axis were chosen. The measured lattice distances for the samples AF117-0.16, AF117-0.35 and AF117-0.59 were 2.74 Å, 2.73 Å and 2.71 Å respectively. These distances do not perfectly fit with the d_{100} lattice distances as measured by

XRD (**Table 5.3**), but follow at least the observed trend, namely that the lattice distances become shorter with increasing aluminium content. This confirms on the nanometre scale the formation of an AlGa₃N solid solution in the form of nanoparticles, enabled by the confining carbon nitride matrix. When the aluminium content is further increased, phase separation occurs, as can be seen from the diffraction pattern in **Figure 5.19**. It appears that the phase separation does not take place in pure AlN and GaN but two mixed phases are formed, where one seems to be an Al doped GaN phase and the other a Ga doped AlN phase. So it seems that the confinement is not able to overcome above a critical aluminium content the phenomenon of spinodal demixing.

To conclude, it was shown that mesoporous carbon nitride is a suitable nanoreactor for the synthesis of pure AlGa₃N nanoparticles with dimensions less than 10 nm. Furthermore it was shown that in a certain concentration range, the composition of the alloy nanoparticles could be adjusted by simply changing the Al/Ga ratio in the precursor solution.

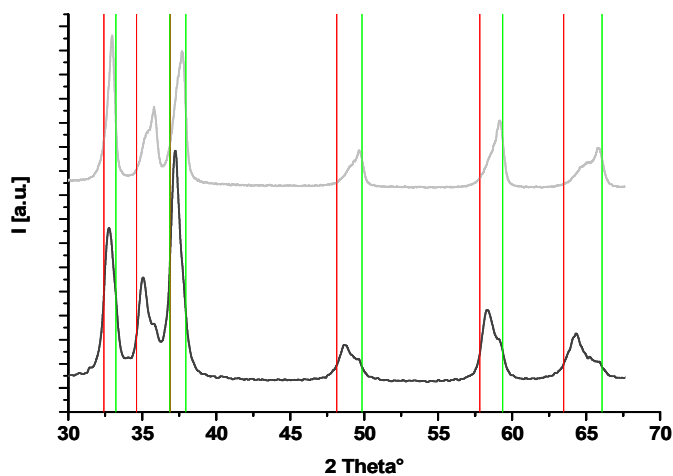


Figure 5.19: Powder X-Ray diffraction pattern of sample AF117-0.65 (---) and sample AF117-0.8 (—) with higher aluminium content. A phase separation into two mixed alloy phases is observed. The red and green lines represent the peak position of pure GaN and pure AlN respectively.

5.1.4 Synthesis of TiVN nanoparticles in mesoporous graphitic carbon nitride

The second ternary metal nitride system which was synthesised in mesoporous graphitic carbon nitride with 12 nm pores (mpg-C₃N₄-1-LHS40), following the same procedure as for the AlGaN system, is TiVN. TiCl₄ and VOCl₃ were chosen as precursors for the infiltration of the mesoporous C₃N₄ nanoreactor. As in the case of the AlGaN system three solutions with different Ti/V molar ratios (**Table 5.4**) were used.

Sample	VOCl ₃ [mg]	TiCl ₄ [mg]	EtOH [g]	V/Ti mol ratio
AF154-0.16	170	1000	2	0.19
AF154-0.35	400	800	2	0.55
AF154-0.59	800	600	2	1.46

Table 5.4: Composition of the infiltrating solutions for the synthesis of (TiV)N nanoparticles in mpg-C₃N₄-LHS40.

After the annealing treatment at 800°C under nitrogen atmosphere three black powders were obtained. The composition of the powders was investigated with EA, EDX and ICP measurements. To determine the exact composition of the powders was difficult, because an important difference between values obtained from EA, EDX and ICP was observed, whereas repeated measurements with the same technique gave consistent values. Since the amount of carbon is very high in the samples and EDX is a surface sensitive technique, EDX probably overestimate the amount of carbon coating the particles. Nevertheless it is possible to give a qualitative estimation. As in the case of the AlGaN nanoparticles, the EDX (**Figure 5.20**) and ICP (**Table 5.5**) measurements of the TiVN nanoparticles reveal that, as expected the vanadium content in the powders increases with increasing vanadium concentration in the precursor solution. Furthermore the V/Ti molar ratio of the precursor solution corresponds with the V/Ti molar ratio found in the annealed powders, which is expected.

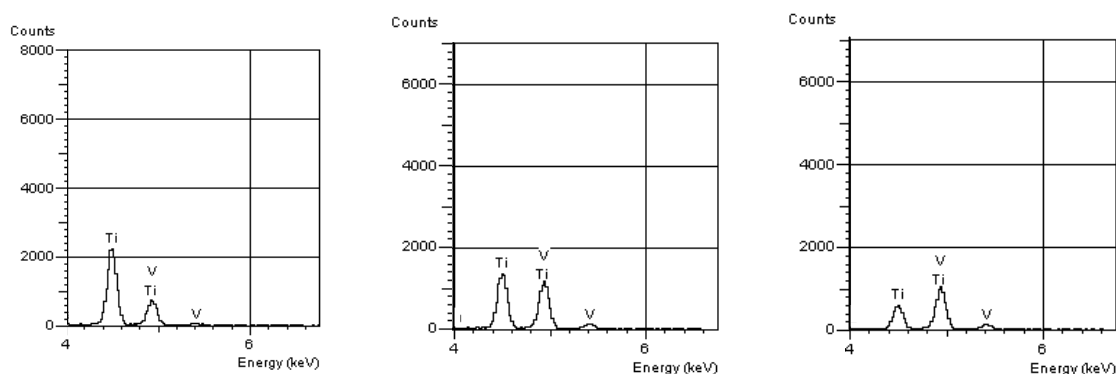


Figure 5.20: EDX measurements from the TiVN nanoparticles. From the left to the right respectively samples AF154-0.16, AF154-0.35 and AF154-0.59.

Sample	V wt%	Ti wt%	N wt%	C wt%	O wt%	V/Ti mol. ratio powder	V/Ti mol ratio solution
AF154-0.16	4.5	22	11.19	51.78	6.02	0.192	0.19
AF154-0.35	8.5	15	11.6	53.14	6.03	0.563	0.55
AF154-0.59	14.3	8.9	9.6	55.61	2.44	1.478	1.46

Table 5.5: Composition (from ICP, from EDX) of the different TiVN nano crystalline powders with increasing V content. The nitrogen content determined by EA was in good agreement with the EDX value, whereas the carbon content determined by EA was only about 30 wt% like in the TiN and VN samples.

Contrary to the AlGa₃N system, which was almost carbon free, a large amount of amorphous carbon is found in the “TiVN” samples (see **Table 5.5**). This is not surprising, since it was already noticed that in the case of the synthesis of binary GaN nanoparticles, no carbon was detected, whereas in the case of the synthesis of VN and TiN nanoparticles carbon residues up to 30 wt% have been detected. Furthermore, the amount of oxygen found in the samples is higher than in the case of the AlGa₃N system. This amount of oxygen is too high to be only correlated to surface oxidation. Nevertheless the presence of pure titanium oxide or vanadium oxide in the samples can be excluded as shown by the absence in the XRD pattern of peaks belonging to any corresponding oxide. Therefore, since the sample was not stored under protective atmosphere, the oxygen contamination can come from physisorbed water on the samples surface or from oxidised carbon functions on the amorphous carbon residue. However incorporation of oxygen inside the crystal structure is not excludable, since both Ti(ON) and V(ON) species are known. The crystallinity of the samples was investigated by using XRD. The diffraction patterns are shown in **Figure 5.21**. As in the case of the AlGa₃N nanoparticle system, the X-ray diffraction patterns of the samples shift to higher angles toward the pattern of pure VN, with increasing vanadium content in the powder. This again indicates the formation of a (TiV)N solid solution. All three samples exhibits diffraction patterns with cubic symmetry and crystallise in the space group Fm3m. The exact peak positions as well as the cell parameters are listed in **Table 5.6**. From the *Scherrer* equation applied to the (200) and the (111) peak an average crystallite size was determined for each sample. The crystallite size range from 5 nm to 3.7 nm when the vanadium content increases, indicated by a progressive broadening of the diffraction peaks with increasing vanadium content. This broadening is probably due the reduction in size of the crystallites but could as well result from a lower crystallinity of the samples due to crystallisation defects.

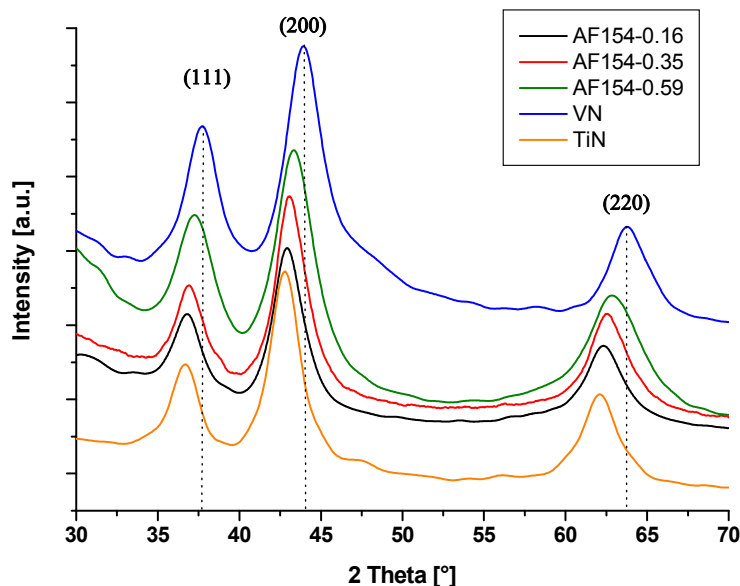


Figure 5.21: X-ray diffraction pattern of the TiVN nano crystalline powders with increasing vanadium content. As a reference the pattern of pure TiN and VN synthesised in the same conditions are presented.

Sample	Peak position 2θ [°]					Cell parameter [Å] Fm-3m a=b=c	Crystallite size XRD	Particle size TEM
	(111)	(200)	(220)	(311)	(222)			
TiN	36.77 2.444	42.72	62.01	74.32	78.23	4.233	-	-
AF154-0.16	36.89 2.436	42.86	62.22	74.58	78.52	4.220	5	5
AF154-0.35	37.03 2.428	43.02	62.47	74.89	78.85	4.205	4.6	5
AF154-0.59	37.44 2.402	43.50	63.22	75.85	79.87	4.160	3.7	4
VN	37.73 2.384	43.84	63.73	76.50	80.57	4.130	-	-

Table 5.6: Exact diffraction peak positions, cell parameters and crystallite size of (AlGa)N nanocrystalline samples with increasing aluminium content.

The shape and size of the particles was investigated using TEM. Again the particles were dispersed in THF with a drop of oleic acid and treated for several minutes with a high power sonication tip. For these specimens the sample preparation was especially important due to the high amount of amorphous carbon side product which appeared to glue the particles together as can be seen in the STEM overview in **Figure 5.22**. **Figure 5.23** illustrates that small particles with an average size of 5 nm are obtained in all the cases and SAED confirms the crystallinity of the observed particles.

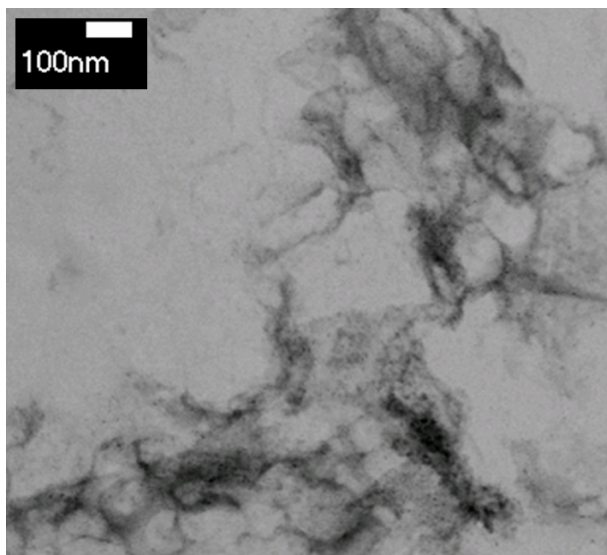


Figure 5.22: STEM overview of sample AF154-0.16. The particles are embedded in a carbon matrix.

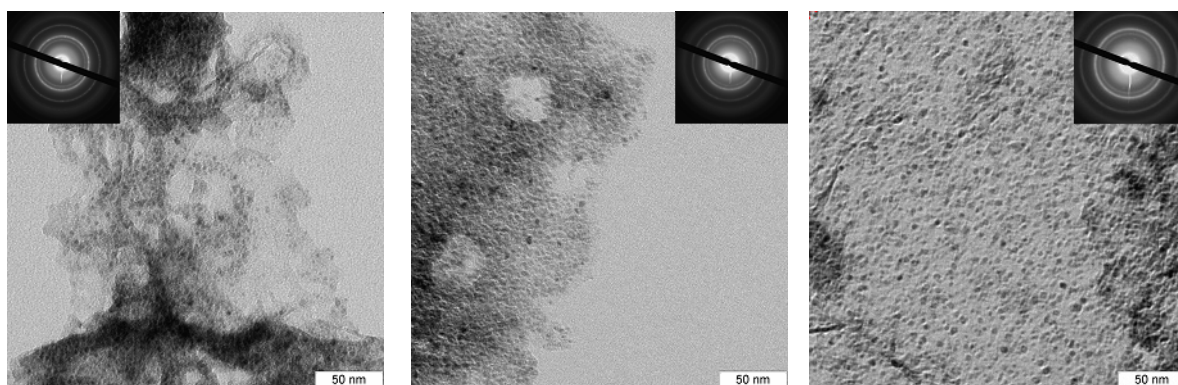


Figure 5.23: TEM micrographs and SAED of the sample AF154-0.16, AF154-0.35 and AF154-0.59 with increasing vanadium content from the left to the right respectively. The camera length for sample AF154-0.16 and AF154-0.35 is 290 mm and 360 mm for sample AF154-0.59

In order to investigate the correlation between the particle size and the crystallite size, complementary HRTEM measurements were performed. All the samples exhibit highly crystalline nanoparticles, as highlighted by the presence of well developed lattice fringes in **Figure 5.24**. The area delimited by the lattice fringes is in a good agreement with the crystallite size determined from XRD and from the TEM measurements, so that the observed nanoparticles are in fact small nanocrystals. From the corresponding FFT the lattice distances were determined. It was very difficult to find particles with the same orientation, so that an accurate comparison of the lattice distances was difficult. Moreover the presence of residual carbon was responsible for a lot of background noise in the FFT. However a trend toward smaller lattice distances with increasing vanadium content was observed. This observation was in good agreement with the complementary EELS measurements (**Figure 5.24**). Care was taken to illuminate only single particles, in the sense that the spot size was adjusted to the size of one nanocrystal in order to be sure to detect only elements in or at the surface of one single nanocrystal. As a consequence, only a qualitative analysis could be performed, since a

quantitative elemental analysis would have required a precise knowledge of the convergence semi-angle and the collection semi-angle, which are spot size dependent. The EELS measurements in **Figure 5.24** show the presence of nitrogen, titanium and vanadium in all the cases. A carbon signal is also present, which comes firstly as the nanoparticles appear to be embedded in a carbon matrix and secondly from the carbon coat of the grid. This thus proves the formation of a TiVN alloy on the nanometre scale. Small amounts of carbon impurities incorporated in the crystal structure can however not be completely excluded. From the semi-quantitative integration on the different edges, the increasing amount of vanadium from sample AF154-0.16 to sample AF154-0.59 was verified, illustrating thus that the described synthesis approach allows synthesising TiVN nanocrystals with tunable composition.

As a conclusion, mesoporous $g\text{-C}_3\text{N}_4$ is not only a powerful “nanoreactor” for the synthesis of binary metal nitride nanoparticles, but has revealed to be suitable for the controlled synthesis of ternary metal nitride alloys nanoparticles with tuneable compositions. The composition of the final product being simply dependent on the ratio of the precursor metals in the solution. As in the case of binary nitrides, this synthetic approach has shown to be quite general since it permitted to synthesize hexagonal systems such as AlGaN alloys on a nanometre scale and also cubic nanocrystalline TiVN powders.

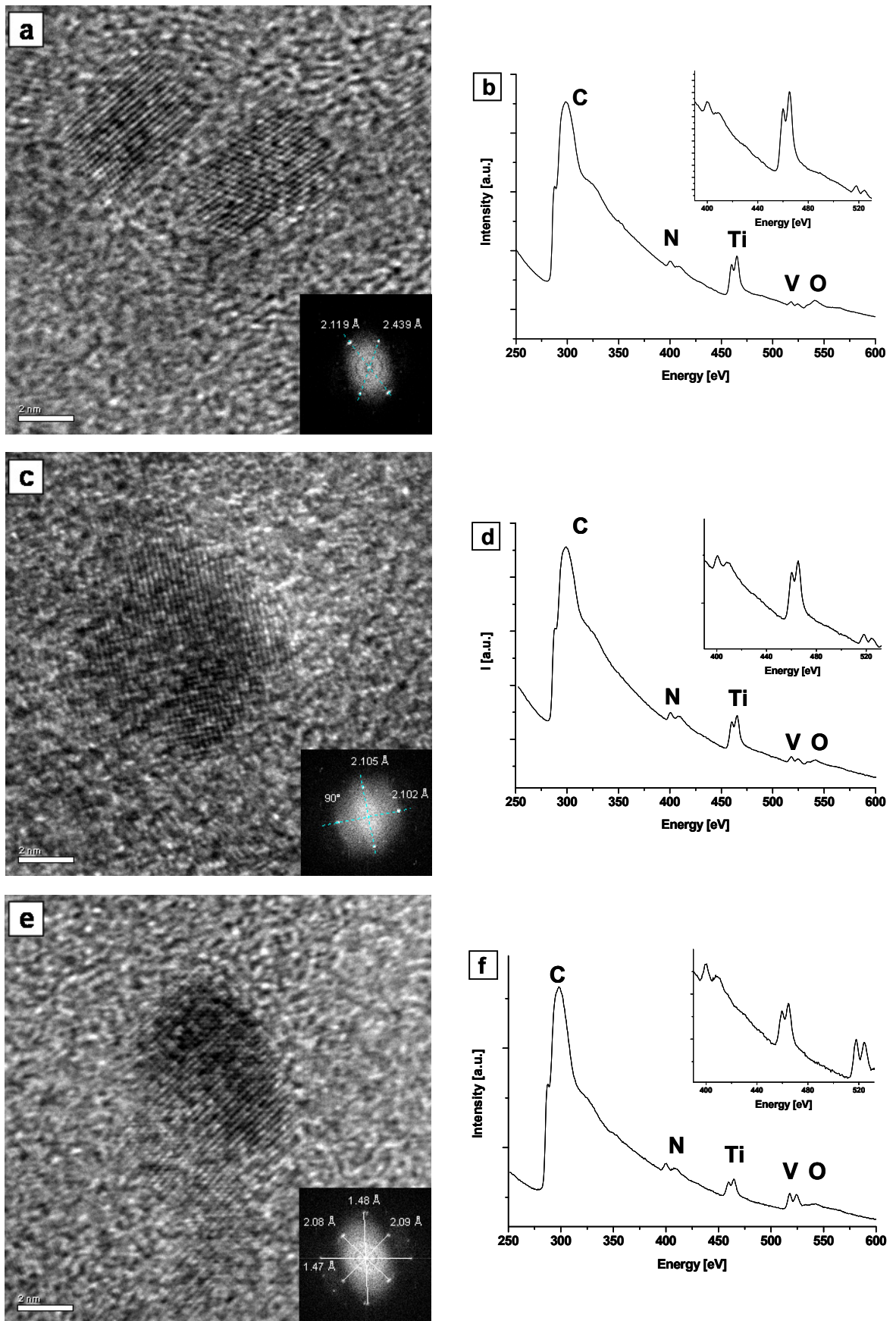


Figure 5.24: a) c) e) HRTEM micrographs and FFT and b) d) f) the corresponding EELS spectrum of the samples and AF154-0.16, AF154-0.35 and AF154-0.59 respectively.

5.2 Synthesis of a macroporous titanium nitride/carbon foam

The previous chapter illustrates that the structure and morphology on a nanometre scale of graphitic carbon nitride can be controlled through hard templating. In addition the nanostructured carbon nitride can in turn be used as hard template itself for the synthesis of other nanostructured crystalline materials. Since graphitic carbon nitrides can act as nitrogen source, releasing nitrogen in the form of ammonia and hydrogen cyanide during their thermal decomposition, they can also be used as templates for the synthesis of nanostructured metal nitrides, as illustrated in the previous section for the synthesis of metal nitride nanoparticles in and through the thermal decomposition of mesoporous graphitic carbon nitride.^[124]

This section will focus on the synthesis of a macroporous TiN/carbon foam by using a macroporous graphitic carbon nitride as nitrogen donor template. While the synthesis of the metal nitride nanoparticles was based on nanocasting it will be shown that in this case the resulting TiN/carbon foam results from a nanocoating on the carbon nitride support. The used graphitic carbon nitride template is a macroporous graphitic carbon nitride (CN-60) described in detail in chapter 4 with a pore size of 60-65 nm, a surface area of 65 m²/g and an apparent pore volume [nitrogen sorption] of 0.165 cm³/g. In contrast to the nanoparticle metal nitride synthesis, the macroporous metal nitride was produced using much more dilute metal precursor solutions, with larger pores in the carbon nitride template, thus ensuring that the pores were only partially filled. Due to the chemical affinity of titanium for amine functions, we can assume that the titanium atoms are bound to the surface of the carbon nitride pores through their amine functions. The infiltrated powder was aged for one night at 100°C, first of all to evaporate the ethanol and secondly to induce a partial condensation of the TiCl₄ in the presence of the air moisture inside the pores. A black powder was obtained after a heat treatment at 800°C under nitrogen, during which time the porous carbon nitride is decomposed into NH₃ and CN_x gases, as verified by TGA-mass spectroscopy. The XRD pattern in **Figure 5.25** of the resulting powder TiN-60 could be indexed in agreement with the diffraction peaks observed for osbornite (TiN, space group: $Fm\bar{3}m$, cell parameter: $a = b = c = 4.235 \text{ \AA}$, $\alpha = \beta = \gamma = 90^\circ$ ^[106]), as it was already observed in the case of the synthesis of TiN nanoparticle in mpg-C₃N₄-LHS40. The observed diffraction peaks are rather broad, indicating that the TiN-60 powder is composed of osbornite nanocrystals. From the Scherrer equation applied to the most intensive diffraction peak (200), the crystallite size was determined to be around 7 nm. Concerning the chemical composition of the TiN-60, beside the presence of osbornite, 30 wt% of residual carbon could be detected with elemental analysis. Thus the material is probably better described as TiN/carbon nanocomposite.

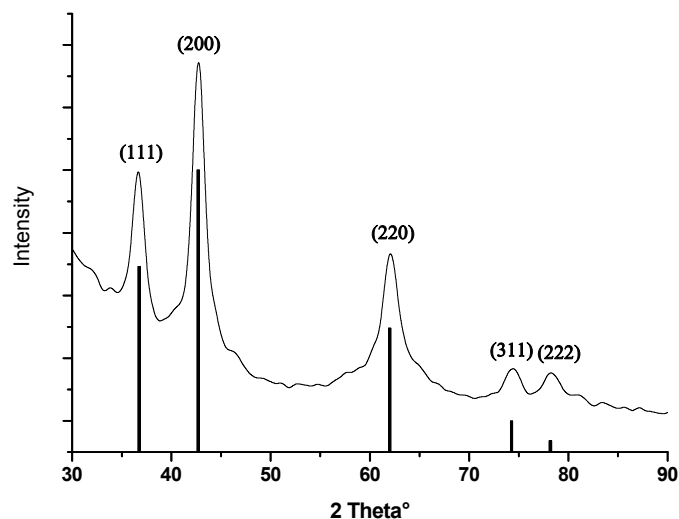


Figure 5.25: X-Ray diffraction pattern of the macroporous TiN/carbon composite resulting from the calcination under nitrogen flow of the $\text{TiCl}_4/\text{EtOH}$ infiltrated macroporous carbon nitride. The black lines represent the peak positions from the ICSD database for the osbornite phase.

The porosity of the sample was investigated by SEM and TEM measurements. **Figure 5.26** and **Figure 5.27** shows the SEM and TEM images of the starting macroporous graphitic carbon nitride (CN-60) and the resulting titanium nitride/carbon powder (TiN-60). The TiN-60 powder is highly porous, as was the CN-60 powder, and constituted of a well defined pore system consisting of 47-55 nm diameter spherical pores. However, even if the CN-60 and TiN-60 materials looks quite similar regarding their porous structure, the pores observed in the TiN-60 sample [\varnothing ~47-55 nm] are about 10 nm smaller than the pores observed in the starting carbon nitride CN-60 [\varnothing ~60-65 nm]. This observation, correlated with the determined crystallite size by XRD (7 nm), leads to the conclusion, that the titanium oxide precursor during the aging step at 100°C was not filling the pores to replicate them in the form of 60 nm nanospheres, as in the case of the nanoparticle synthesis in mpg- C_3N_4 -LHS40, but rather covered the pore walls to form a coating on the macroporous carbon nitride template. The fact that the pore walls of the TiN-60 sample are much thinner than those of the CN-60 sample, as can be seen from the TEM images (**Figure 5.27**), is a supplementary argument confirming the hypothesis of a coating formation on the pore walls.

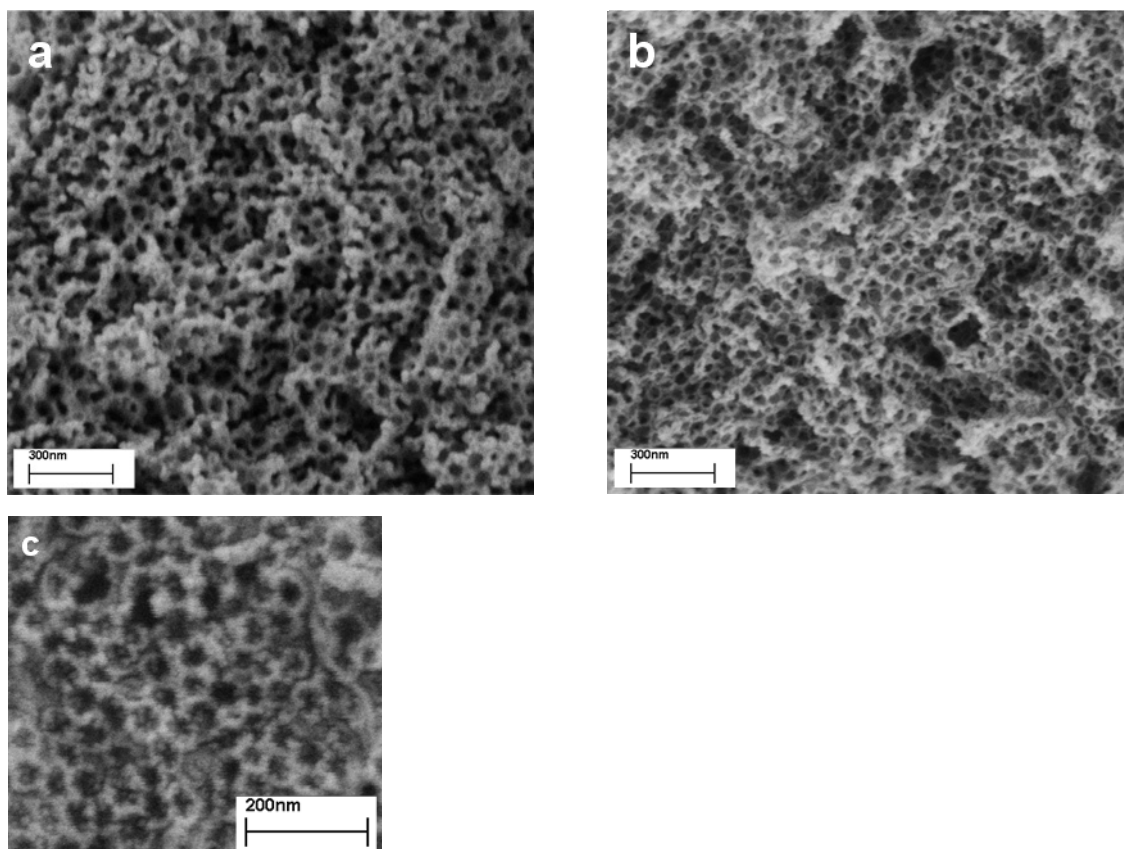


Figure 5.26: SEM images of the starting macroporous carbon nitride CN-60 (a) and of the resulting macroporous TiN/Carbon composite TiN-60 (b,c).

Selected area electron diffraction (SAED) (inset in **Figure 5.27**) confirms that the observed porous structure is composed of crystalline osbornite, as the observed diffraction rings corresponds to the expected lattice spacing of the osbornite crystal phase. At higher magnification in SEM (**Figure 5.26**), it seems that the pore walls of the titanium nitride are not a continuous crystalline system but are composed of TiN nano crystallites, which is in good agreement with the results obtained from XRD and confirmed by HRTEM measurements. As can be seen from **Figure 5.28**, the pore walls are composed of 5-7 nm crystallites, with well developed lattice fringes. The Fast Fourier Transformation of the selected area in **Figure 5.28**, gives a measured distance of 2.119 Å, which compares well with the database reported lattice distance $d_{(200)} = 2.117$ Å of the TiN osbornite phase. Moreover HRTEM shows that TiN nanocrystals are embedded in an amorphous carbon matrix. EDX measurements on the pore walls, were confirming the presence of titanium in the walls (peak at 4550 eV and at 4950 eV).

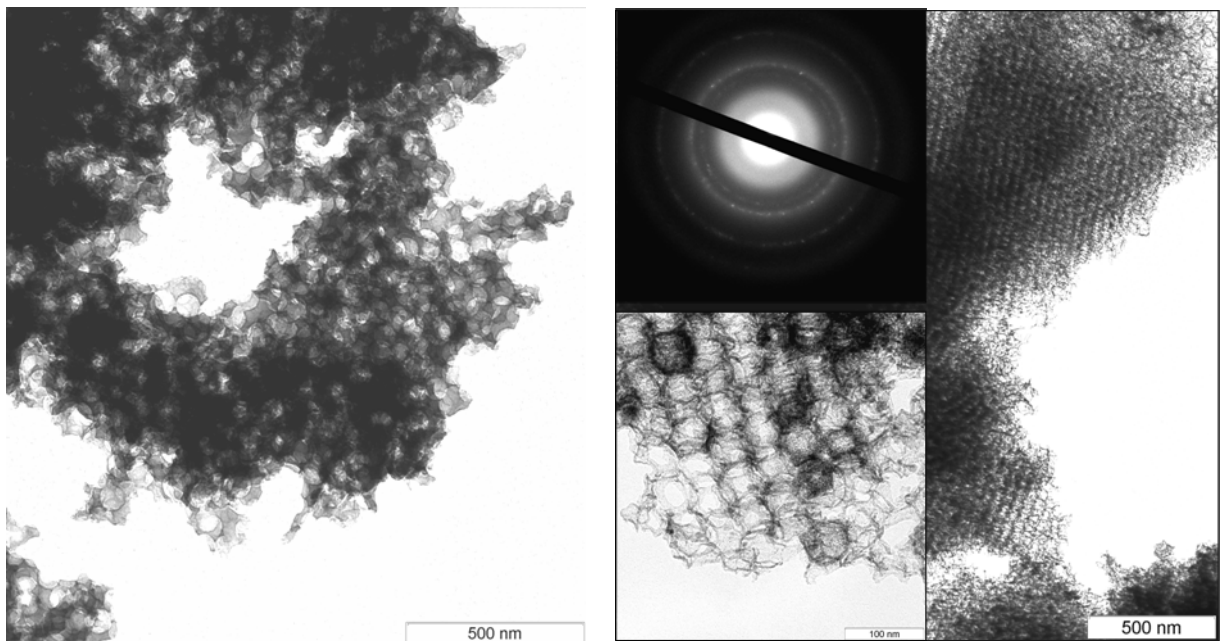


Figure 5.27: TEM images of the macroporous graphitic carbon nitride CN-60 (left) and the TiN/carbon composite TiN-60 (right) with selected area electron diffraction (SAED)

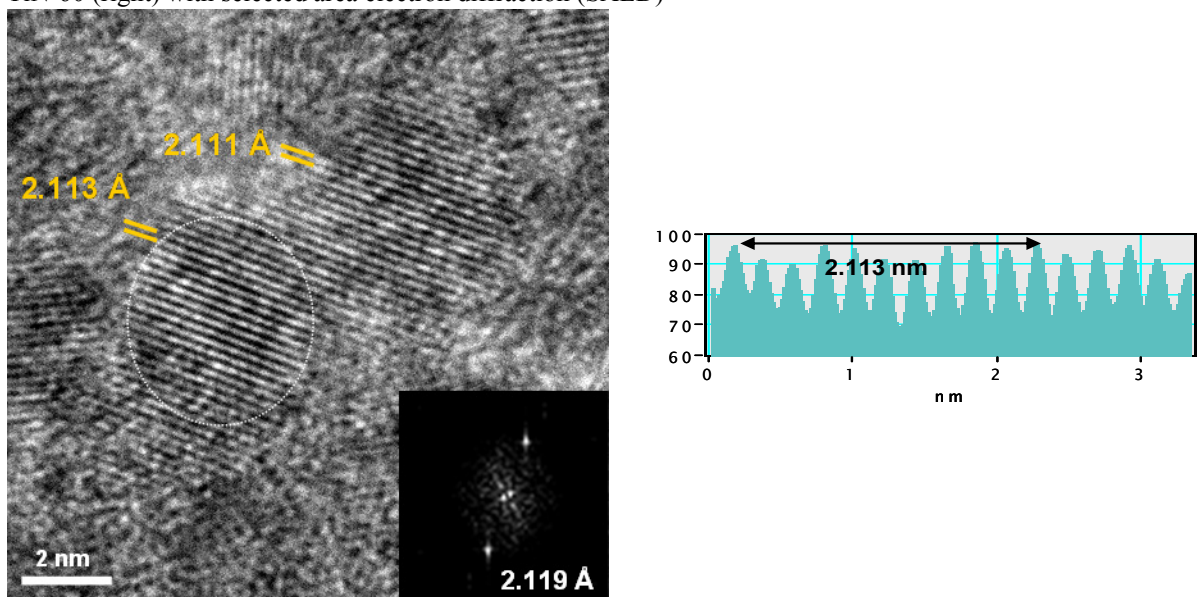


Figure 5.28: HRTEM pictures from the macroporous TiN/carbon composite TiN-60. The inset inset represents the reduced FFT of the delimited area. A lattice distance of 2.11 Å, corresponding to the lattice distances d_{200} of the osbornite phase, could be determined.

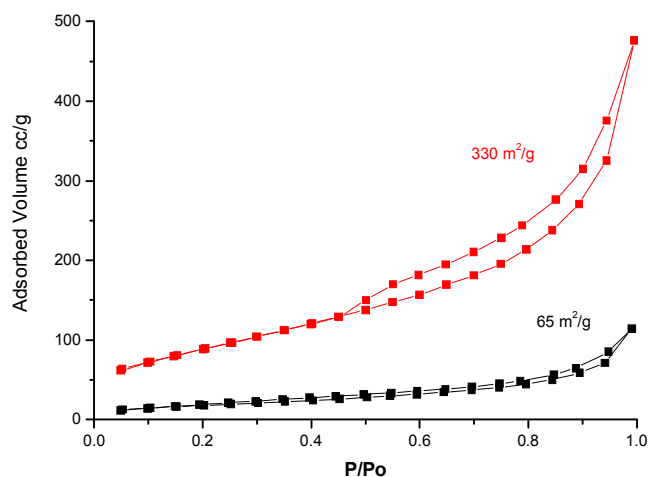


Figure 5.29: Nitrogen sorption isotherm adsorption and desorption branch of the starting carbon nitride template/nitriding agent CN-60 (---) and the resulting titanium nitride/carbon composite TiN-60 (---).

The combination of these observations with the results from the elemental analysis implies that the observed structures are TiN nano crystals embedded in an amorphous carbon membrane forming a macroporous TiN/carbon composite. The surface area and the apparent pore volume of the TiN-60 sample were investigated by nitrogen sorption measurements.

Figure 5.29 shows the nitrogen sorption isotherm measurements for the macroporous TiN-60 and for the macroporous CN-60 samples. While the isotherm for the CN-60 points to a pure macroporous material, the isotherm of the TiN-60 sample points to a macro- and mesoporous material as there is an opening of a hysteresis in the partial pressure range $0.43 < p/p_o < 1$. Remarkable in the comparison of the two samples, is the big difference in the measured surface area and apparent pore volume. The TiN-60 powder exhibits a high surface area of $330 \text{ m}^2/\text{g}$ and an apparent pore volume of $0.76 \text{ cm}^3/\text{g}$, which is almost five times bigger than the obtained values for the starting CN-60 carbon nitride template, which had a surface area and an apparent pore volume of $65 \text{ m}^2/\text{g}$ and $0.167 \text{ cm}^3/\text{g}$ respectively. This gives a clear indication of additional porosity present in the TiN/ carbon composite. Indeed, as schematically depicted in **Figure 5.30**, when the carbon nitride walls of the macroporous CN-60 are decomposed during the thermal treatment, while releasing nitrogen rich gases to the “titanium oxide” coating and transforming it in TiN, an additional porosity is created. This means that the final system can be seen as interconnected TiN/Carbon composite 50 nm hollow spheres. Moreover, the nanoparticulate structure of the pore walls in the TiN-60 sample contributes as well to the high surface area, through the creation of supplementary interface. And finally considering the extreme thinness of the TiN-60 pore walls, the ratio of surface area to bulk mass of the material decreases.

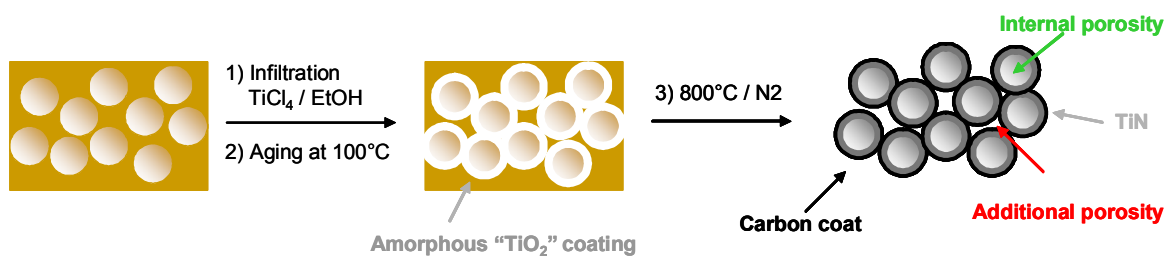


Figure 5.30: Schematic representation of the formation of the macroporous titanium nitride/carbon composite TiN-60 starting from the macroporous carbon nitride CN-60.

To conclude, it was shown that despite a nanocasting synthetic approach in mesoporous graphitic carbon nitrides, such as for the metal nitride nanoparticles, macroporous graphitic carbon nitride can be used to synthesize high surface area titanium nitride/ carbon nanofoams via a nanocoating approach. The resulting foam is similar in morphology to the starting carbon nitride, but due to the nanocrystalline structure of the resulting porewalls, their thinness and the additional outer surface creation through the decomposition of the carbon nitride, it was possible to increase the specific surface area of the resulting TiN/carbon composite by a factor 5.

5.3 Synthesis of titanium nitride/carbon hollow spheres

Using the same synthetic strategy as for the TiN/C foam described above, a macroporous carbon nitride with 500 nm pores in diameter, CN-500 was used to synthesize by nanocoating hollow spherical structures. A SEM micrograph of the porous carbon nitride CN-500 is shown in **Figure 5.31**. As for the CN-60 sample, a well defined and homogeneous pore network of 500 nm spherical pores was obtained after the removal of the silica template and is thus highly appropriate to be used as the nitrogen donor template in this study. One remarkable point here is the thinness of the pore walls compared to the pore size. Indeed, the thinness of the walls is related to the available quantity of nitrogen in the system and the pore dimension is related to the quantity of titanium infiltrated into the system for one given precursor solution concentration.

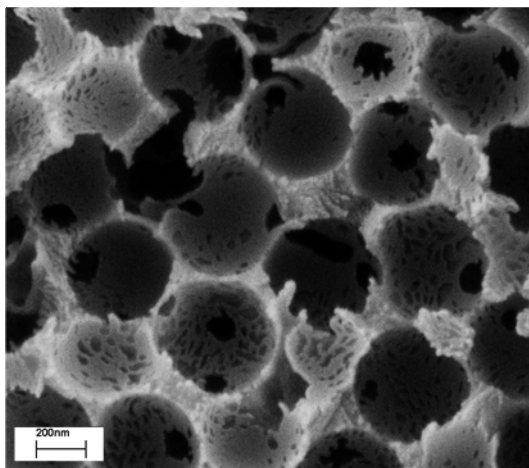


Figure 5.31: SEM image the macroporous carbon nitride template with 500 nm pores (CN-500).

The CN-500 powder was then infiltrated with a titanium precursor solution (1 g TiCl_4 in 5g ethanol) as for the synthesis of the TiN-60 material. After filtration, the powder was dried and aged for one night at 100°C and finally annealed at 800°C under nitrogen atmosphere. The obtained powder was composed of cubic crystalline TiN, as shown by the XRD pattern (**Figure 5.32**). The peaks are broad and indicate once more the presence of TiN nanocrystallites. From the *Scherrer* equation, applied to the most intense peak, the (200), the crystallite size is about 7 nm in size. Interestingly, elemental analysis indicates that there is no residual carbon left in this sample. So it seems that the wall thickness had just the right dimension in thickness, to ensure a stoichiometric reaction between the metal precursor and the nitrogen donor matrix thus avoiding the formation of carbon side product. This is an important point, proving that carbon nitrides are indeed good nitrogen donor systems for the synthesis of pure metal nitrides, in the sense of phase purity and carbon contamination. The microstructure of the sample was investigated by SEM (**Figure 5.34**). The obtained TiN powder TiN-500 is composed of 450-470 nm spheres. Higher magnification illustrates that the spheres are hollow and apparently composed of nanocrystallites. The hollow structure of the spheres was additionally confirmed by TEM, as depicted in **Figure 5.35**. Moreover the nanoparticulate structure of the hollow sphere walls is clearly seen in **Figure 5.35**. HRTEM evidenced that the nano particles, the building blocks of the walls, are highly crystalline, as shown by the presence of well developed lattice fringes. From the FFT of the crystallite marked by an arrow in **Figure 5.35** a lattice distance of 2.1 Å could be measured, corresponding to the lattice distance $d_{200}=2.11$ Å of cubic TiN (osbornite). As in the case of the TiN-60 sample, the morphology of the resulting TiN powder is a result of the morphology of the starting carbon nitride template. A comparison of the starting macroporous network of the carbon nitride with

the final hollow spheres, in terms of shape and size, clearly indicates that the morphology of the TiN hollow spheres was imprinted by the shape and size of the carbon nitride pores.

The porosity of the obtained TiN-500 hollow sphere powder was investigated via nitrogen sorption measurements. The adsorption and desorption isotherms of the TiN powder are shown in **Figure 5.33**, as well as the adsorption and desorption isotherms of the starting carbon nitride powder CN-500. Both materials exhibit isotherms of type II, characteristic for macroporous materials. The TiN powder has a surface area of $143 \text{ m}^2/\text{g}$ and an apparent pore volume of $0.66 \text{ cm}^3/\text{g}$, whereas the starting carbon nitride CN-500 has only $16 \text{ m}^2/\text{g}$ surface areas and an apparent pore volume of $0.06 \text{ cm}^3/\text{g}$. This difference in surface area and porosity can first be explained, as for the TiN-60 sample, by the formation of a titanium oxide coating on the pore walls of the CN-500 starting carbon nitride, which is then during the thermal decomposition of the carbon nitride converted into TiN, resulting in the observed TiN hollow spheres. Moreover, as already mentioned the walls of the TiN hollow spheres are composed of nanoparticles, whereas the starting CN-500 material has very compact walls. So the increase in surface area and porosity is not surprising since it results from nanoparticle inter grain porosity.

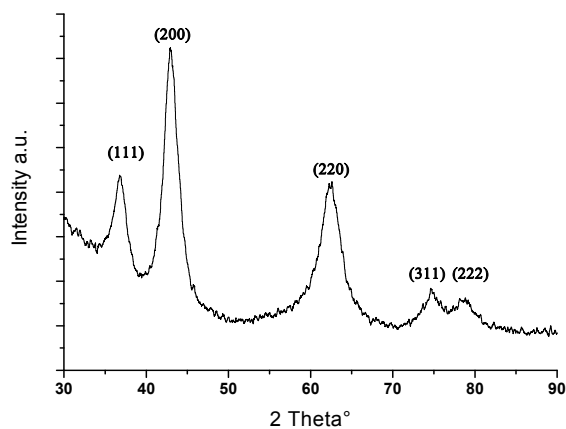


Figure 5.32: X-ray diffraction pattern of the resulting TiN-500 obtained from the macroporous carbon nitride CN-500, with 500 nm pores.

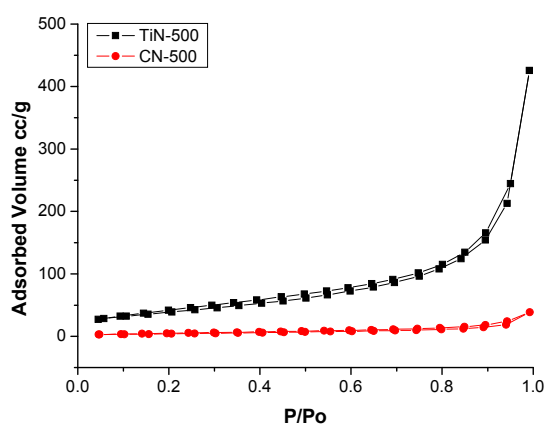


Figure 5.33: Nitrogen adsorption and desorption isotherms of the starting macroporous carbon nitride CN-500 (--) and of the resulting TiN-500 (--).

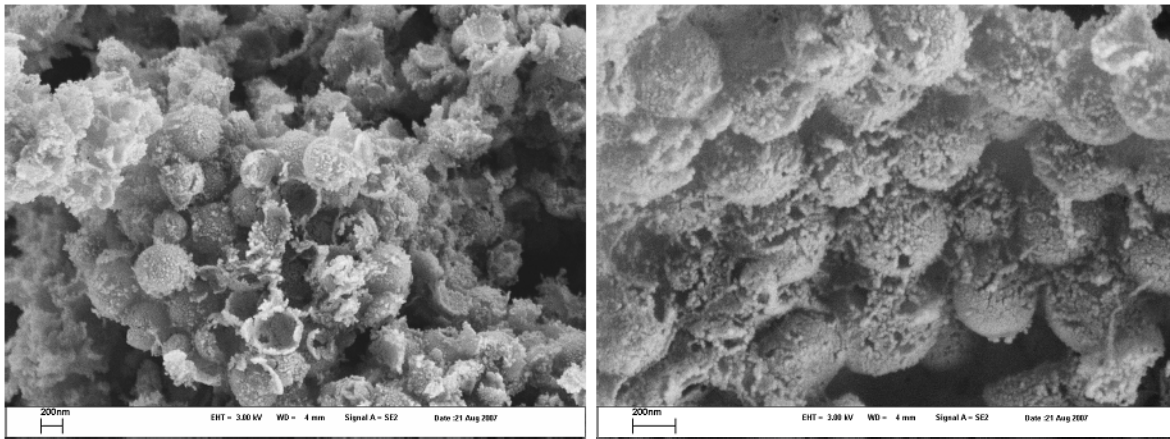


Figure 5.34: SEM images of the obtained 500 nm TiN hollow spheres TiN-500. The left image shows nicely the nanoparticulate structure of the sphere walls.

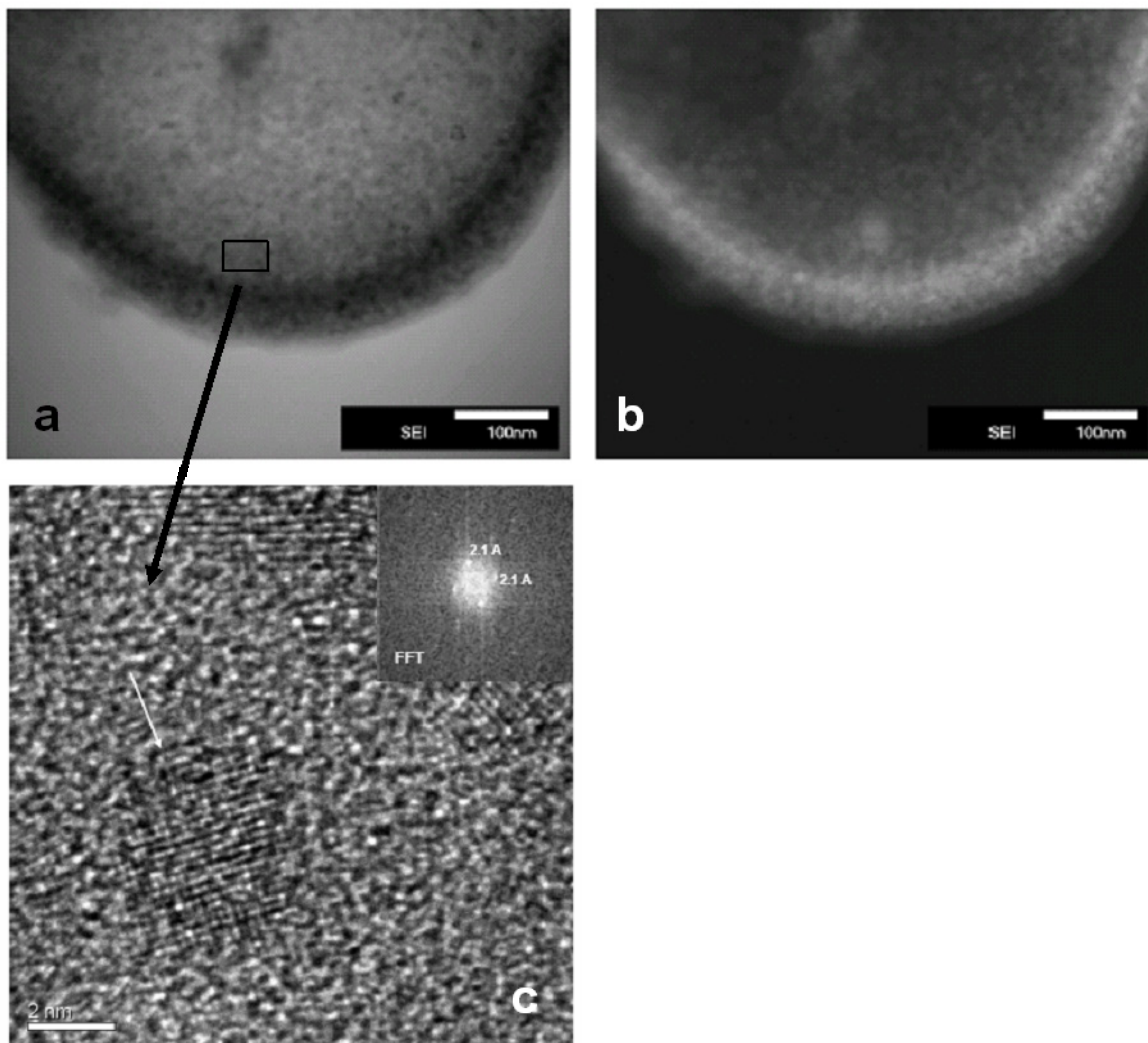


Figure 5.35: Bright Field (a), Dark Field (b) STEM measured on one isolated TiN hollow sphere. HRTEM (c) show that the sphere wall is composed of small (5-7 nm in size) TiN nanocrystals.

In conclusion, highly defined TiN hollow spheres with high surface area could be synthesized by firstly nanocoating the titanium precursor on the pore walls of a macroporous graphitic carbon nitride reactive template, followed by the decomposition of the carbon-nitride template during which the titanium precursor was then converted into the titanium nitride. The obtained hollow spheres are composed of TiN nanocrystallites. An important point to underline is that compared to the synthesis of the TiN/carbon nanofoam, a pure TiN is formed without any carbon residue. This indicates that by choosing an appropriate Ti/C₃N₄ ratio, the last being controlled by the wall thickness, a stoichiometric reaction is possible without the formation of any amorphous carbon residue. So obtaining chemically pure metal nitrides with the carbon nitride hard templating approach is just a matter of optimization, in the sense that a given wall thickness is controlled by the titanium precursor concentration.

5.4 Synthesis of mesoporous titanium nitride into mesoporous titanium oxide: maintaining the structure through the nitrogen source

Due to their combination of high surface area and narrow pore size distribution, mesoporous materials are of considerable interest for applications in e.g. catalysis, sensing or separation.^[125-127] The vast majority of mesoporous materials are based on oxides with amorphous (e.g. silica) or crystalline (e.g. anatase or other transition metal oxides) pore walls. The latter materials often feature pore walls composed of nanocrystallites and are therefore referred to as nanocrystalline (nc) mesoporous materials.^[128-130]

An attractive goal, providing new opportunities for material science, is the expansion of the composition of mesoporous materials to non-oxide analogues, as for example the corresponding metal nitrides. However, reports on mesoporous nitrides are rare and mainly based on silicon and boron nitrides.^[94, 131-134] This section describes a novel approach to synthesize mesoporous titanium nitride with high surface area from mesoporous titanium oxide using cyanamide or, more precisely, its condensation product, g-C₃N₄, as nitrogen source.

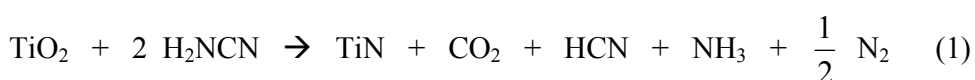
Titanium nitride is an important technological material because of its high hardness, high melting point (~3000°C) and good electrical conductivity.^[135] It thus is an attractive material for applications as abrasive materials,^[136] as electrodes in electrochemical capacitors in highly corrosive electrolytes and in semiconducting devices.^[137-141] Furthermore, due to their noble metal like electronic properties, early transition metal nitrides were applied as catalysts.^[135, 142] For example titanium nitride was recently successfully used as a noble metal free

hydrogenation catalyst^[3] and it will be shown below that the here synthesised mesoporous TiN was although acting as a catalyst for the C-C coupling of alcohols and ketones.

5.4.1 Synthesis of mesoporous titanium nitride

Mesoporous titanium nitride was synthesized from a mesoporous titanium oxide precursor with cyanamide or, more precisely, a carbon nitride as a nitrogen source. There are several mesoporous titanium oxides exhibiting well-defined mesostructures and pore sizes described in the literature, which could have definitely served as precursor for the approach shown here and would even lead to ordered mesoporous titanium nitrides.^[143-147] However, most of these studies deal with the preparation of thin films. As the products in this study were to be tested for catalytic activity, it was decided for a bulk preparation of another, yet unordered mesoporous titania. The bulk samples of mesoporous titanium oxide were synthesized as described by Wang and coworkers^[104, 148] using the non-ionic surfactant Triton X-100 as template. After extraction of the surfactant, a mesoporous nanocrystalline anatase powder was obtained (**Figure 5.36**, P-0.0). Several experiments using cyanamide (CA)/TiO₂ mass ratios from 2-14 were carried out (**Table 5.7**). The infiltrated materials were subsequently heated in a covered crucible to 800°C under nitrogen.

The reaction which is expected to take place between the cyanamide, the nitrogen donor, and the titanium oxide during the heating process is the following:



Under normal conditions, TiO₂ ($\Delta_f G_{298}^0 = -959.03$ kJ/mol) is more stable than TiN ($\Delta_f G_{298}^0 = -346.65$ kJ/mol).^[112] This reaction is favoured by the formation of thermodynamically stable species, such as CO₂, HCN, NH₃ and N₂. Moreover, after the principle of *Le Chatelier*, the reaction equilibrium is displaced toward the TiN formation, because all the products of this reaction, except the TiN, are volatile and permanently removed from the system during the reaction.

The resulting black powders after the annealing at 800°C were characterized by XRD, TEM, HRTEM, nitrogen sorption and elemental analysis. **Figure 5.36** shows the XRD pattern of the mesoporous TiO₂ precursor powder and the obtained powders resulting from the annealing of the cyanamide impregnated TiO₂.

Sample	CA/TiO ₂ mass ratio	CA/TiO ₂ mol. ratio	Crystallite size (nm)	Carbon weight %	BET surf. area (m ² /g)	BJH ads. Pore size (nm)	Pore Volume (cm ³ /g)
P-0 TiO ₂	0	0	6.4	0	230	6.0	0.29
P-2 TiO ₂	2	3.8 [1.9]	8.1	0.45	132	4.6	0.28
P-2.5 TiN	2.5	4.7 [2.35]	5.1	0.28	166	66.9	0.28
P-3.9 TiN	3.9	7.4 [3.7]	5.0	1.8	142	6.1	0.22
P-4.5 TiN	4.5	8.5 [4.25]	5.4	10.4	112	5.3	0.17
P-6 TiN	6	11.4 [5.7]	5.0	16.6	85	5.3	0.17
P-10 TiN	10	19 [9.5]	4.8	21.6	56	6.6	0.21
P-14 TiN	14	26.5 [13.25]	5	26.3	45	7.2	0.18

Table 5.7: Structure parameters of the starting mesoporous TiO₂ (P-0) and different TiN derivatives. The crystallite particle size was determined from XRD measurements, by the use of the Scherrer equation and from TEM measurements. The carbon content of the samples was determined with elemental analysis. Surface area, pore size and pore volume were determined by nitrogen sorption. The numbers in [] corresponds to the equivalents of cyanamide, considering reaction (1).

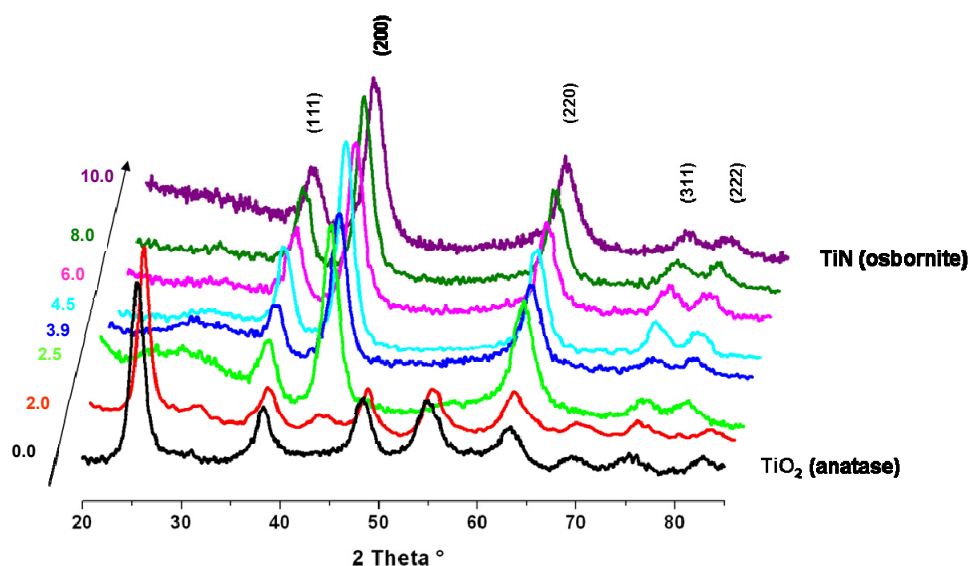


Figure 5.36: XRD pattern of as-prepared mesoporous TiO₂ powder and of the final mesoporous TiN powders prepared using different CA/TiO₂ weight ratios. (waterfall presentation with x shift of 10%)

The XRD patterns of all the resulting black powders, except for sample P-2.0 which has insufficient amount of nitrogen donor, are in good agreement with the XRD pattern of osbornite (TiN). Indeed the calculated cell parameter $a=b=c=4.21$ Å fits with the expected database value of 4.23 Å for cubic titanium nitride, belonging to the space group $Fm\bar{3}m$.^[149]

The measured peak positions and the corresponding lattice distances as well as the theoretical data base values are listed in **Table 5.8**. One has to remark, that the obtained TiN from

preformed mesoporous TiO₂ has slightly smaller cell parameters than the TiN nanoparticles obtained in mesoporous g-C₃N₄ ($a = b = c = 4.233 \text{ \AA}$). Furthermore the relative intensities of the (111) and (220) peaks are slightly different from those observed from the TiN nanoparticle synthesised in mesoporous graphitic carbon nitride. Nevertheless these effects were already observed by Buha *et al.*,^[109] who synthesised TiN nanoparticles from preformed TiO₂ (anatase) nanoparticles using cyanamide, urea and ammonia as the nitrogen source.

Sample	TiN Fm3m [148]		P-2.5	P-3	P-4.5	P-6	P-8	P-10	P-14
	2 θ [°]	d [Å]							
(111)	36.76	2.4451	36.90	36.89	36.79	36.87	36.89	36.88	36.81
(200)	42.70	2.1175	43.01	42.93	42.96	42.90	42.93	43.1	43.07
(220)	61.98	1.4973	62.42	62.44	62.30	62.37	62.43	62.59	62.57
(311)	74.27	1.2769	74.87	74.77	74.52	74.80	74.71	74.82	74.85
(222)	78.18	1.2225	79.00	78.91	78.85	78.88	78.98	78.91	78.95

Table 5.8: Theoretical peak positions of TiN Fm3m and measured peak positions of the different samples with increasing carbon content.

No peaks corresponding to anatase were observed in the XRD patterns of samples prepared with CA/TiO₂ mass ratios higher than 2, proving that nearly pure TiN can be produced using this synthetic pathway. For sample P-2 the amount of cyanamide is simply insufficient to convert the titanium oxide into titanium nitride. From the theoretical reaction, which supposedly occurs during the thermal treatment, only one equivalent of cyanamide would be required to completely convert the TiO₂ into TiN. This corresponds to a CA/TiO₂ mass ratio of 1.05, however experimentally nearly 2.3 equivalents of cyanamide are needed for complete conversion. This can be explained as some of the melamine formed during the condensation of cyanamide is sublimed during the heating process. To avoid this sublimation step, TiO₂ could have been converted into TiN in sealed quartz ampoules. But this would have considerably limited the synthesis to small amounts of TiO₂, which would have been inconvenient, since the TiN powders were planned to be used as catalysts. Moreover, recondensation of CN compounds from the gas phase, during the cooling down of the ampoule is a non desirable side effect. What is surprising with the sample P-2, except the fact that it is not converted into TiN, is that it is still anatase (see **Figure 5.37**). Indeed, at 800°C, the stable TiO₂ allotrope is normally rutile. As a reference experiment, a pure TiO₂ powder, without the addition of any cyanamide, was annealed at 800°C under nitrogen with the same annealing conditions. As expected, the obtained allotrope was rutile, as it can be seen in **Figure 5.37**. So it seems that the presence of cyanamide has an influence in the stabilisation of the anatase phase at high

temperature, in the sense that it hinders the expected phase transformation. Another remarkable point concerns the crystallite size in the two powders, as they were exposed exactly to the same temperature. For both powders, the starting TiO_2 powder consisted of nano crystalline anatase with crystallite size in the range of 6 nm, indicated by the broadness of the diffraction peaks. The P-2 sample is composed of anatase nanocrystals of 8 nm in size. In contrast, the resulting rutile powder, which exhibited much sharper peaks in the XRD pattern, ended with a crystallite size of 30 nm, due to the sintering of the crystallites at high temperature. As a consequence, it seems that the presence of cyanamide has an influence both on the stabilisation of the anatase phase at 800°C and on the stabilisation of the nano crystals toward sintering. This could be explained, by the fact that the cyanamide condenses into a solid phase around the TiO_2 during the heating process. This could firstly mechanically stabilise the oxide network toward collapse and sintering. Secondly, when the carbon nitride solid is decomposed, it is possible that the anatase phase undergoes some doping processes with carbon and/or nitrogen atoms, through solid diffusion processes, especially at high temperature.^[151] Moreover, it is interesting to note that no mixed or intermediate phases of TiO_2 and TiN can be observed using this synthesis, speaking for a dissolution-recrystallization mechanism rather than a topotactic transformation of preformed crystallites.^[109]

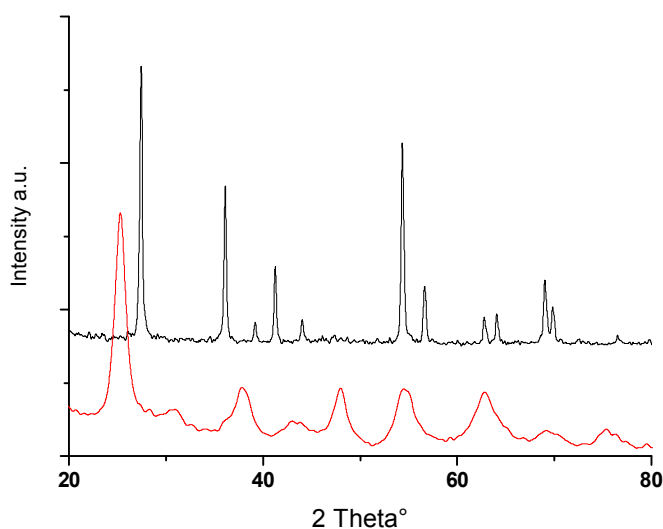


Figure 5.37: XRD diffraction pattern of the pure TiO_2 powder heated at 800°C under nitrogen (black line, allotrope rutile) and of the sample P-0.2 (red line, allotrope anatase).

The size of TiO_2 and TiN crystals forming the walls of the annealed materials was determined using the *Scherrer* equation. The exact values for each sample are summarised in **Table 5.7**. For as-made TiO_2 the crystallite size was estimated to 6.4 nm, while further heating the samples to 800°C , here indirectly indicated by sample P-0.2, increased the particle size to 8 nm. In contrast, for all TiN samples considerably smaller crystallite sizes of approximately 5 nm were observed.

The porosity of the as-made TiO_2 and the resulting TiN powders were characterized by nitrogen-sorption measurements (**Figure 5.38**). All materials show type IV isotherms characteristic for mesoporous materials. The TiN powders have lower surface areas compared to the mesoporous TiO_2 precursor powder, owing to the higher density of TiN compared to TiO_2 . However, comparing mesoporous TiO_2 (P-2) and TiN (P-2.5) both heated to 800°C , a higher surface area of the titanium nitride is observed. It can be assumed for TiO_2 that the high temperature treatment of the powder led to a partial fracture of the mesoporous structure, explaining the loss in surface area. It is also observed that the surface areas of the mesoporous TiN depend on the amount of cyanamide used during synthesis as a higher CA/ TiO_2 mass ratio results in a lower surface area. This can indeed be attributed to an increasing amount of carbon in the samples, produced by a side-reaction throughout the decomposition of the carbon nitride.

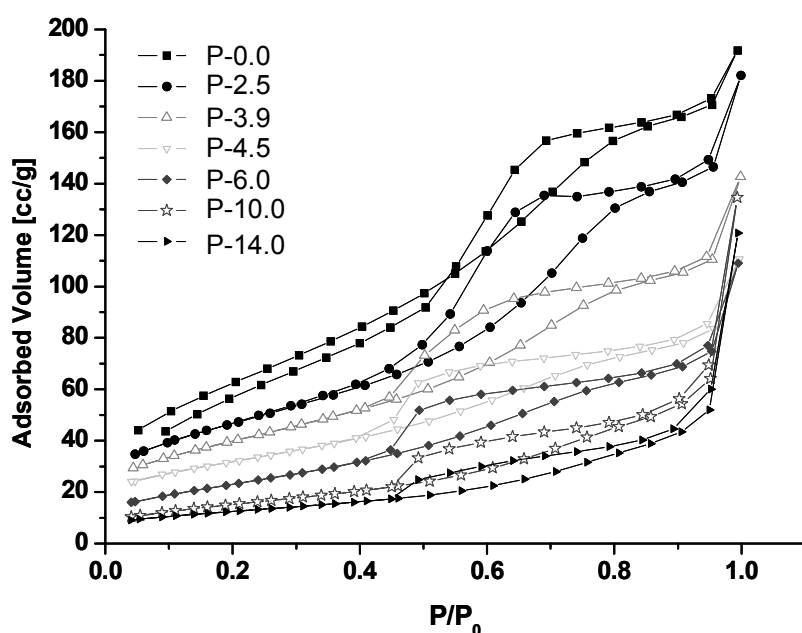


Figure 5.38: Nitrogen sorption isotherms of the starting mp- TiO_2 (---) and of the resulting mp-TiN materials made with different cyanamide amounts.

This can be proven by elemental analysis (**Table 5.7**) which show that with an increasing amount of cyanamide the carbon content in the resulting titanium nitride samples increases from close to zero up to 26 wt% of carbon. Thus, an approximately pure mesoporous TiN without further cleaning steps can be just observed at lower CA/ TiO_2 ratios (P-2.5) while higher cyanamide contents result in TiN/carbon nanocomposites. The average pore size calculated from the BJH model applied to the adsorption branch was determined to be 6 nm for the TiO_2 precursor powder and varied from 7.2 nm to 5.3 nm for the different TiN powders (**Table 5.7**). No clear trend can be observed concerning the different CA/ TiO_2 mass ratios, indicating that the formed carbon does not necessary block the pores, but still reduces

dramatically the surface area, without enormous changes in the pore sizes and the pore volume. **Figure 5.39** shows the TEM micrographs of the starting mesoporous TiO_2 and the obtained mesoporous TiN powder. The overall particular framework described by Wang *et al.*^[104] for the porous TiO_2 is also found in the resulting titanium nitride. The corresponding selected area electron diffraction patterns furthermore prove the existence of anatase and osbornite, respectively, confirming the results obtained by the powder XRD measurements.

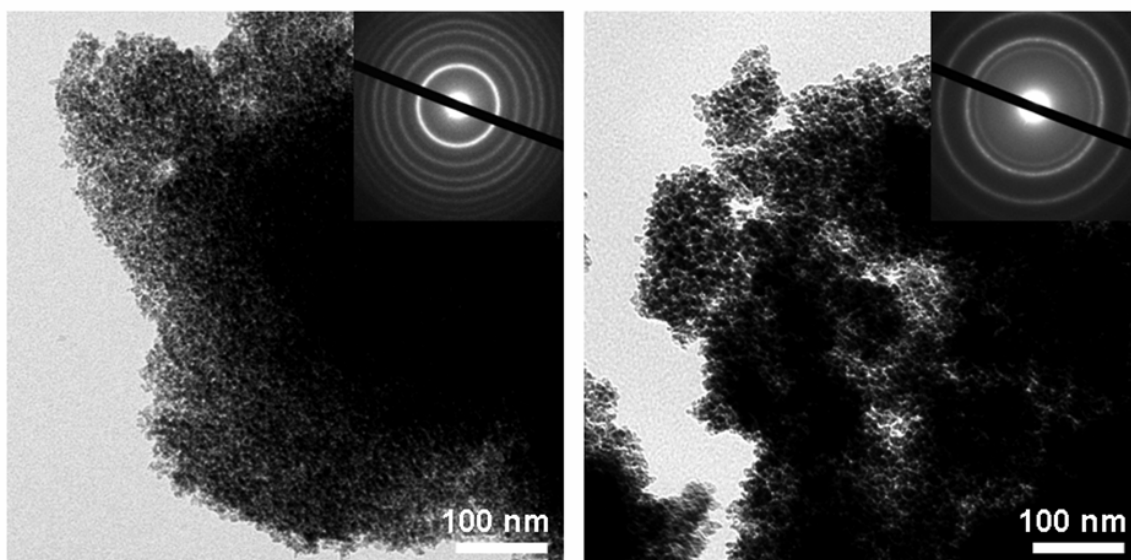


Figure 5.39: TEM pictures of the mesoporous TiO_2 precursor (P-0.0) (left) and the obtained osbornite TiN (P-2.5) (right). The insets represent the diffraction rings of anatase (left) and osbornite (right) obtained from SAED measurements.

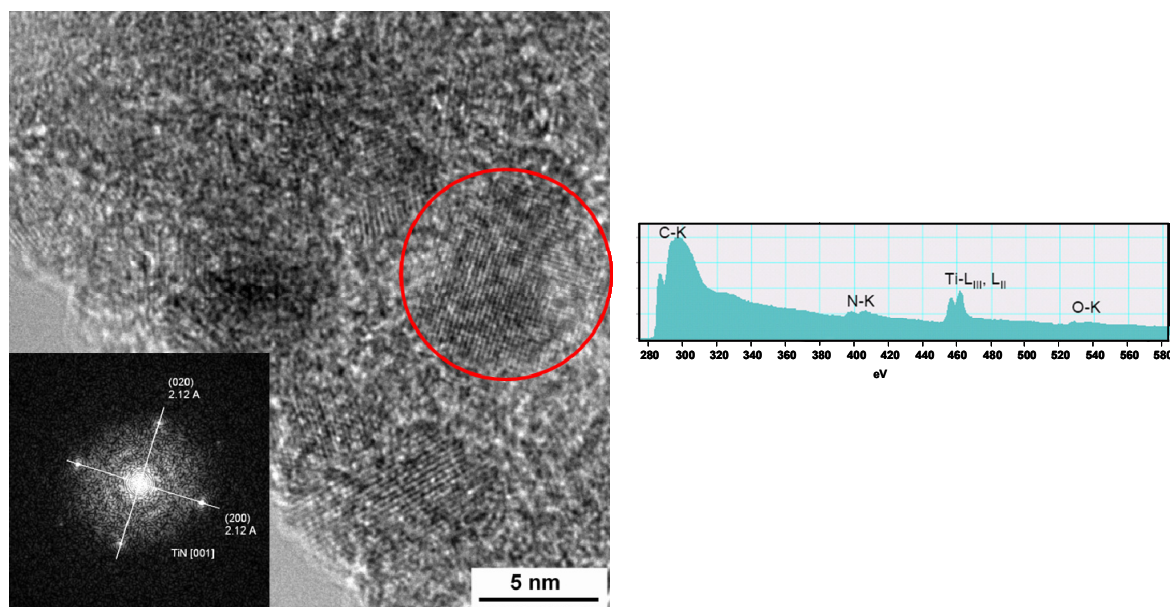


Figure 5.40: HRTEM image of crystalline particles exhibiting the TiN (osbornite) structure of the P-6 sample. The inset shows the calculated FFT of the indicated area. The particle is oriented with the [001] zone axis parallel to the electron beam.

On the nanometre scale HRTEM measurements (**Figure 5.40**) evidence once more that the sample is constituted of a framework of well crystallized TiN nanoparticles. As demonstrated by the fast Fourier transform (FFT) of the selected area on the HRTEM picture (red circle), the measured distance of 2.12 Å corresponds to the expected theoretical value of $d_{(200)} = 2.117$ Å of a cubic osbornite titanium nitride^[152] as well as the measured angle of 90° between the (020) and (200) planes. Apparently the particle is oriented with the [001] zone axis parallel to the electron beam.

To conclude, this solid state nitrification process permits the chemical conversion of anatase into osbornite, whilst keeping the nanostructure of the precursor oxide in the resulting nitride.

5.4.2 Application of mesoporous TiN in catalysis

Early transition metal nitrides are very promising catalyst materials. For example M.K. Neylon *et al.* used transition metal nitrides such as VN, Mo₂N, WN, TiN and NbN as catalysts for ethanol amination and compared their activity with classic catalysts for this reaction, such as Pt and Ni catalysts.^[153] The investigated metal nitrides showed high performances in this reaction as well as a good selectivity. To illustrate the potential of the here synthesised materials, we employed their higher basicity as compared to their corresponding oxides.^[154]

As the aim was to access cheap and easy to handle catalysts, the obtained powders were neither stored nor handled under inert gas. More over the scaling up of the synthesis of mesoporous TiN (in order to be able to run a large number of catalytic tests) proved easier with the procedure with the highest initial cyanamide/TiO₂ ratio. Thus the powders resulting from this synthesis (P-14) were used as a catalyst even if they featured a large amount of residual carbon as shown above. As preliminary tests, the activity of our TiN powder was tested in aldol condensation and further compared to the activity of mesoporous TiO₂ in the alkylation of ketones with alcohols.

5.4.2.1 Aldol condensation

The first reaction investigated was the aldol condensation. The aldol condensation, the reaction between two aldehydes or ketones to form an enal, respectively an enone, is among the most useful C-C bond forming reactions in organic synthesis^[155]. Many materials proved able to catalyze this reaction including functionalized mesoporous silica^[156] and basic oxides^[157]. It was thus relatively straight forward to test, in a first step, the as synthesized TiN/carbon composites as catalyst on this reaction.

As can be seen from **Table 5.9** mesoporous TiN can effectively act as a catalyst for this type of reaction, with conversion rates higher than 80% in all cases and relative good selectivities. It has to be mentioned that even under the relatively harsh reaction conditions employed the reaction mixtures remained relatively simple.

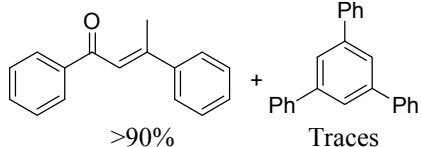
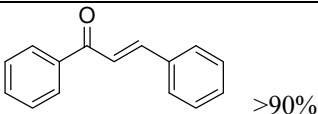
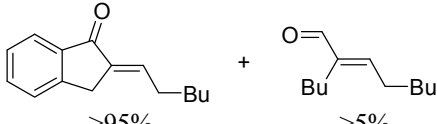
Substrate	Conversion % [a]	Products [b]
Acetophenone (500 mg)	85	
Cyclohexanone (500 mg)	95	
Acetophenone (120 mg) Benzaldehyde (110 mg)	100	
Indanone (140 mg) Hexanal (100 mg)	100 [c]	

Table 5.10: Aldol condensation catalysed by TiN. [a] Determined by GC with mesitylene as an internal standard. [b] The indicated percentage corresponds to the relative amount of compound within the reaction products as determined by GC. [c] Calculated on the basis of the aldehyde.

5.4.2.2 Alkylation of ketones with alcohols

The porous TiN was then tested as a catalyst on the direct alkylation of ketones with alcohols under very similar conditions and compared with the activity of the porous TiO₂ precursor. Table 3 summarizes some of the obtained results.

As can be seen, a large variety of ketones could be alkylated in moderate to high yields under the chosen conditions. The products obtained using TiN as a catalyst are, to a large extent, α,β -unsaturated ketones or aldehydes, confirming that TiN is able to catalyse this alkylation as it was reported for Nb₂O₅.^[158] Nevertheless, it is remarkable that in this case the reaction products are much cleaner than in the case of niobium oxide. The scope of alcohols, which could be used as electrophiles seems limited to benzyl alcohol derivatives (such as benzyl alcohol, **Table 5.11**, entry 1, 4-methylbenzylalcohol, **Table 5.12**, entry 3, or 4-methoxybenzyl alcohols, **Table 5.13**, entry 4) while the range of useful ketones is much broader. Acetophenone, indanone and cyclohexanone yielded the corresponding alkylation products with benzyl alcohol to more than 90 % (**Table 5.14**, entries 1, 8 and 9 respectively). Surprisingly, mesoporous TiO₂, meant as a reference sample, not only proved to be active for the same type of reactions but features a broader scope of applications. Indeed, this oxide was also able to promote the alkylation of numerous ketones with less active electrophiles such as

aliphatic alcohols (as exemplified by hexanol, **Table 5.15**, entry 6) or even secondary alcohols (such as 1-phenylethanol or cyclohexanol, **Table 5.16**, entries 5 and 7, resp.).

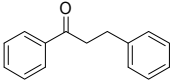
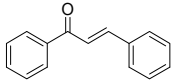
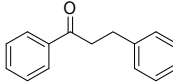
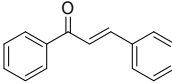
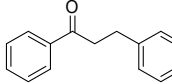
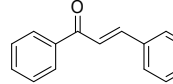
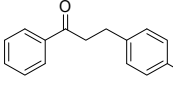
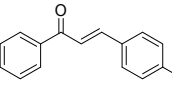
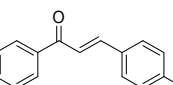
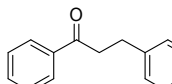
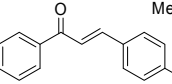
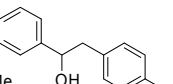
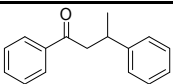
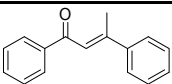
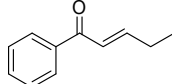
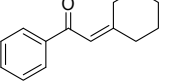
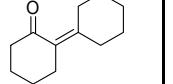
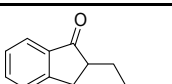
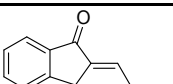
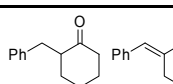
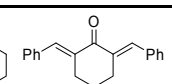
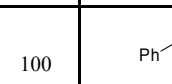
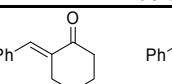
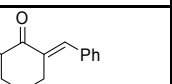
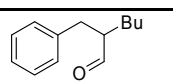
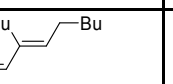
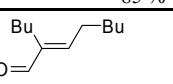
	Substrates	TiO ₂		TiN	
		Conv (%) ^[b]	Products ^[c]	Conv (%) ^[b]	Products ^[c]
1	Acetophenone Benzyl Alcohol	100	 > 95 %	100	 > 90 %
2	Acetophenone Benzyl Alcohol ^[d]	90	 70 %  30 %	40	 10 %  90 %
3	Acetophenone 4- Methylbenzyl Alcohol	100	 90 %  10%	31	 > 95 %
4	Acetophenone 4-Methoxy- benzyl Alcohol	100	 > 95 %	100	 10 %  90 %
5	Acetophenone 1-Phenyl- ethanol	99	 40 %  60 %	0	/
6	Acetophenone Hexanol	41	 < 95 %	0	/
7	Acetophenone Cyclohexanol	10	 65 %  35 %	0	/
8	Indanone Benzyl Alcohol	100	 > 95 %	100	 > 95 %
9	Cyclo- hexanone Benzyl Alcohol	50	 Traces  65 %  15 %	100	 15 %  85 %
10	Hexanal Benzyl Alcohol	100	 5 %  95 %	99	 > 90 %

Table 5.17: Alkylation of ketones with alcohols catalysed by TiN.

[a] In a typical reaction 50 mg of titanium dioxide or nitride were added to a 2 ml solution of 1 mmol ketone and 1 mmol aldehyde in xylene and heated to 150°C for 48h. [b] Determined by GC on the basis of the alcohol conversion with mesitylene as an internal standard. [c] The indicated percentage corresponds to the relative amount of compound within the reaction products. [d] Reference test with 10 mg of catalyst.

Contrary to what is observed with TiN, the obtained alkylation products are mostly saturated. This can be exemplified by the alkylation of acetophenone with benzyl alcohol (**Table 5.18**, entry 1). On one side; TiN yielded 90 % of 1,3-diphenylpropen-1-one, whereas on the other, TiO₂ gave 95 % of 1,3-diphenylpropan-1-one. The main mechanism involved in the TiO₂ catalyzed reaction thus presumably differs significantly from the assumed one for TiN, and involve the concomitant deprotonation of the ketone and activation of the alcohol, as depicted in **Figure 5.41**. This would then be very similar to the mechanism postulated by Sanchez et al. for the mesoporous ZrO₂ catalyzed hydroformylation of alkenes and alkynes.^[159, 160]

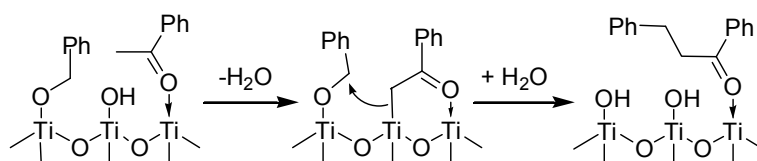


Figure 5.42: Proposed mechanism for the mp-TiO₂ catalysed alkylation of ketones

In this chapter, a new method to access high surface area TiN like materials from nanocrystalline anatase using cyanamide as nitrogen source was presented. It was shown that the overall nanoparticulate structure could be maintained during the nitrification process, keeping an acceptable porosity and surface area, since g-C₃N₄ a condensation product of cyanamide at high temperature acts as a scaffold to prevent the collapse of the pores upon nitration. Moreover, it was possible to achieve the synthesis of a pure TiN and as well the synthesis of TiN/carbon composites, by simply varying the nitrogen donor content, allowing the controlled tuning of the carbon content of the final material. In a second step this material was evidenced to be also able to act as a versatile catalyst for aldol condensations. More importantly, both TiO₂ and TiN/carbon composites could be used as versatile and valuable alternatives to noble metal complexes in various C-C bond forming reactions. The activity of these catalysts originates from a combination of Lewis acidic and Brønsted basic properties. The alkylation of ketones with alcohols appears to be a very attractive reaction option. The required reaction conditions are harsher than the one reported for noble metal catalysts, for example, by Kwon *et al.*^[161] but this draw-back might be balanced by the relative abundance of titanium compared to palladium.

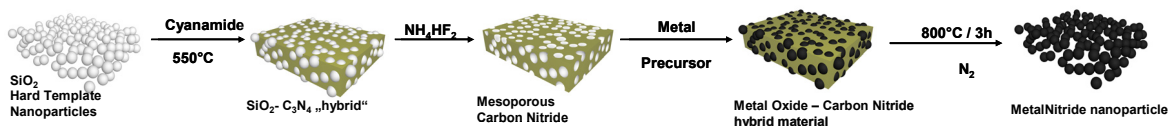
6 Conclusion and outlook

The aim of the present work was to investigate the use of graphitic carbon nitride (g-C₃N₄) nanoreactors for the controlled synthesis of metal nitride nanostructures and to establish the new concept of reactive hard templating, in which the template participates chemically towards the formation reaction of the final metal nitride.

g-C₃N₄ was shown to be a highly suitable reactive template material for the synthesis of metal nitrides, since during its thermal decomposition reactive nitrogen rich species are produced such as NH₃ or C_xN_yH_z gases. Through hard templating g-C₃N₄ nanoreactors could be designed in a controlled fashion. The high temperature condensation of cyanamide (T = 550°C) in the presence of different silica templates lead to well defined g-C₃N₄ nanostructures, once the template was removed. The resulting g-C₃N₄ nanostructures were showed to be perfect replicas or copies of the silica “nano”-templates. There are a multitude of hard templates available in different shapes and sizes allowing for the synthesis of graphitic carbon nitride nanorods, nanotubes, as well as mesoporous and macroporous graphitic carbon nitride powders with spherical pores of different sizes.

The mesoporous g-C₃N₄ (mpg-C₃N₄) showed interesting catalytic activities in the activation of aromatic compounds. In fact it was shown to be a suitable metal free catalyst for the acylation or alkylation of benzene. The experimental results suggested that these reactions do not result from the activation of the electrophile, as in “classical” Lewis acid (AlCl₃) catalysed Friedel-Crafts reactions, but are more likely to result from the direct activation of the benzene from electron donation from the tri-s-triazine motives building the g-C₃N₄ network.

The synthesis of metal nitrides was performed by using the g-C₃N₄ nanostructures as reactive hard templates. This synthetic strategy can be regarded as double replication of the silica nanostructure, used to template the g-C₃N₄.



Mesoporous g-C₃N₄ with 12 nm spherical pores was used as a nanoreactor for the controlled synthesis of binary metal nitride nanoparticles. By taking advantage of the induced confinement, highly crystalline TiN, VN and GaN quasi-spherical nanoparticles could be synthesised. This was achieved by infiltrating the mesoporous powder with an oxide precursor solution of the corresponding metal followed by the thermal decomposition of the g-C₃N₄ template at high temperature under inert atmosphere. In the case of TiN and VN amorphous

carbon was found in the samples as a side product of the reaction. This synthetic approach allowed a fine tuning of particle size either through the concentration of the precursor solution or by the pore size of the nanoreactor. Moreover, the reactive templating concept allowed to extend the metal nitride nanoparticle synthesis toward ternary metal nitride alloy nanoparticles, such as AlGaN or TiVN. Here, due to the confinement, the composition of the “alloy” nanoparticles could be adjusted within a certain range by the composition of the precursor solution, containing both metal precursors, without phase separation.

High surface area macroporous TiN/carbon composite materials could also be obtained by using macroporous g-C₃N₄ as a reactive template. The resulting TiN/carbon composite is the result of the nitrification of a titanium oxide coating preliminarily formed on the g-C₃N₄ pore wall. Following the same reaction mechanism, 480 nm TiN hollow spheres could be synthesised by using a macroporous g-C₃N₄ with 500 nm pores as reactive template. In this case, no carbon impurity was found in the sample.

Finally, by using cyanamide as the nitrogen source for the conversion of mesoporous anatase, mesoporous TiN could be obtained. It was shown that the cyanamide, in addition to its role as the nitrogen source, preserved the mesoporosity up until collapse. The as-synthesised TiN powders showed remarkable catalytic activity in aldol condensation and in the direct alkylation of ketones with alcohols.

In summary, it was shown that the reactive hard templating approach based on g-C₃N₄ templates is a new templating method, which now opens the way to nanostructured metal nitrides that are not accessible by classical templating methods. Nanoparticles are still the most commonly described nanomorphology of inorganic materials and there are many other pathways towards metal nitride nano-particles which can be found, for example by post-treatment of oxide nanoparticles with nitrogen donors. However the advantage of the reactive templating method described in this work can be seen from the abundance of different silica nanostructures that are available as templates. These structures range from particles of different sizes and shapes to porous materials with different morphologies (cylindrical pores, bimodal porosities, monolithic structures etc). This means a large variety of other morphologies for metal nitrides can be envisaged by first producing different graphitic carbon-nitride nanoreactor morphologies and then using the reactive templating method described in this work.

7 Instrumental details

X-Ray diffraction (WAXS and SAXS): WAXS measurements were performed on a D8 Advance machine from Bruker instruments. The X-ray tube was operated at 40 kV and 40 mA. The emitted Cu-K α radiation ($\lambda = 0.154$ nm) was monochromatized by a multilayer Göbel mirror. An energy dispersive detector (Sol-X, Bruker) was used to ensure low background noise, by filtering out the inelastic scattered photons. The samples were measured on silicon sample holders in a reflection geometry as coupled θ -2 θ scans.

SAXS experiments (Cu-K α radiation) were performed using a rotating anode machine with a two-dimensional MARCCD detector.

Nitrogen sorption: Nitrogen sorption experiments were carried out at 77 K using a Tristar 3000 machine (Micromeritics) and Autosorb-1 machine (Quantachrome). Evaluation of the obtained data was done with the BET, BJH and NLDFT models. The Autosorb-1 software was used for the evaluation of the isotherms. The samples were degassed at 150°C for several hours.

Electron microscopy (EM): The SEM used in this work is a LEO 1550-Gemini with an acceleration voltage from 0.1 kV to 30 kV. Non conductive samples were sputtered with gold. The TEM is an Omega 912 machine from Zeiss. It was operated with an acceleration voltage of 120 kV. The samples were measured on carbon coated copper grids (400 mesh). HRTEM on the binary metal nitride nanoparticle and AlGaN particle were done by Dr. Jens-Oliver Müller from the Fritz-Haber-Institute, Berlin on a Phillips TEM/STEM CM 200 FEG transmission electron microscope equipped with a Field-emission gun operated at 200 kV. HRTEM of the TiVN, the macroporous TiN/carbon composite and the TiN hollow spheres were done by Dr. Armin Feldhoff and Frank Steinbach from the University of Hannover on a JEOL TEM/STEM JEM-2100F-UHR transmission electron microscope equipped with a field emission gun operated at 200 kV.

Elemental analysis: A VARIO EL elemental analysis instrument from Elementar Analysensysteme was used to determine the carbon, nitrogen, hydrogen and sulphur content of the samples.

Thermogravimetric analysis (TGA) were performed using a TG 209 F1 machine from Netzsch, Al₂O₃ crucibles were used and a gas flow (oxygen or nitrogen) of 15 mL/min.

Density determination-Ultracentrifugation: The g-C₃N₄ have been mortared and finely dispersed in toluene and bromoform with a concentration of 1.5 mg/ml. To narrow the range of appropriate density of the gradient material, different ratios of bromoform and toluene have been mixed and the sample was allowed to sediment or float in earth gravitational field. The final solvent composition was 0.2 mL of toluene and 0.3 mL of bromoform. The density gradients have been performed on an Optima XLI centrifuge (Beckman Coulter, Palo Alto CA) with absorbance optics at 500 nm and a speed of 50000 rpm. The data have been evaluated with the program Newgradient (Kristian Schilling 2005, Nanolytics, Potsdam Germany) (Lechner M., *Macromol. Rapid Commun.* 18, 781-786 (1997)).

8 Publication List

1. T. Brezesinski, A. Fischer, K. Iimura, C. Sanchez, D. Grosso, M. Antonietti and B. M. Smarsly, *Generation of self-assembled 3d mesostructured SnO_2 thin films with highly crystalline frameworks*, *Advanced Functional Materials* 16 (2006), no. 11, 1433-1440.
2. A. Fischer, M. Kuemmel, M. Jarn, M. Linden, C. Boissiere, L. Nicole, C. Sanchez and D. Grosso, *Surface nanopatterning by organic/inorganic self-local assembly and selective local functionalization*, *Small* 2 (2006), no. 4, 569-574.
3. F. Goettmann, A. Fischer, M. Antonietti and A. Thomas, *Chemical synthesis of mesoporous carbon nitrides using hard templates and their use as a metal-free catalyst for friedel-crafts reaction of benzene*, *Angewandte Chemie-International Edition* 45 (2006), no. 27, 4467-4471.
4. F. Goettmann, A. Fischer, M. Antonietti and A. Thomas, *Metal-free catalysis of sustainable friedel-crafts reactions: Direct activation of benzene by carbon nitrides to avoid the use of metal chlorides and halogenated compounds*, *Chemical Communications* (2006), no. 43, 4530-4532.
5. F. Goettmann, A. Fischer, M. Antonietti and A. Thomas, *Mesoporous graphitic carbon nitride as a versatile, metal-free catalyst for the cyclisation of functional nitriles and alkynes*, *New Journal Of Chemistry* 31 (2007), no. 8, 1455-1460.
6. A. Fischer, M. Antonietti and A. Thomas, *Growth confined by the nitrogen source: Synthesis of pure metal nitride nanoparticles in mesoporous graphitic carbon nitride*, *Advanced Materials* 19 (2007), no. 2, 264.
7. A. Fischer, P. Makowski, J. O. Müller, M. Antonietti, A. Thomas and F. Goettmann, *High surface area TiO_2 and tin as noble metal free catalysts for the c-c coupling of alcohols and ketones*, *ChemSusChem* (2008), no. DOI: 10.1002/CSSC.200819.

9 Acknowledgements

Finally! When I started to write this thesis few months ago, I thought that I would never make it up to here. And now it is done, I reached the last pages of acknowledgements. And this would definitely not have been possible without all the support I received during the last two and a half years.

Firstly, I would like to thank all the people who contributed and helped me in this work:

Prof. Dr. Markus Antonietti, for the nice opportunity he offered me to realise this work. I am grateful for his contagious motivation and energy and especially for his continuous support and trust, helping me to find answers to so many questions.

My supervisor Dr. Arne Thomas for his enduring help and concern, for his suggestions and the numerous discussions we shared.

My coworker Dr. Frederick Goettmann for the exciting catalysis project we worked on, his help and fruitful advice.

Dr. Jens-Oliver Müller (Fritz Haber Institut) and Dr. Armin Feldhoff (University of Hannover) for the HRTEM measurements.

For the financial support I would like to thank the ENERCHEM Project and the Max Planck Society.

I would like to thank all the people of my group, for the friendly and enjoyable working atmosphere. Special thanks go to Regina Rothe for all the sorption measurements and her friendliness and to Dr. Jens Weber for the help with the SAXS experiments.

A big “Thank You” to all my colleagues, who became real friends during the last two and a half years. Andreas Ide, Madeleine Kittner, Marco Rusconi, Julia Maier, Laura Hartmann, Nicole Schreiber and of course Niki Baccile. Many thanks to the Torsten Gang, Silke, Micha and Jörg. Cheers guys! I extend my gratitude to Denis Gebauer for his friendship, help, patience and support in many personal situations. And of course many thanks to all the Chez Briel visitors.

Last but not least I would like to thank my family and my friends for all the supporting love they gave me. Especially my parents and my grand parents for being by my side, supporting me every day and always believing in me. I want to thank Sabrina Gröschke my “soul” sister and my fabulous flat mates Carolina Wicka and John Dunlop. Un énorme Merci à toi John. And all my friends in Paris.

And last but not least I want to thank Simon, for all his love, support and patience throughout all this time.

Thank You

10 References

1. Tiemann, M., *Repeated templating*. Chemistry Of Materials, 2008. **20**(3): p. 961-971.
2. Sproul, W.D., *Physical vapor deposition tool coatings*. Surface & Coatings Technology, 1996. **81**(1): p. 1-7.
3. Kaskel, S., K. Schlichte, and T. Kratzke, *Catalytic properties of high surface area titanium nitride materials*. Journal Of Molecular Catalysis A-Chemical, 2004. **208**(1-2): p. 291-298.
4. Ramanathan, S. and S.T. Oyama, *New Catalysts For Hydroprocessing - Transition-Metal Carbides And Nitrides*. Journal Of Physical Chemistry, 1995. **99**(44): p. 16365-16372.
5. Kwon, H., S. Choi, and L.T. Thompson, *Vanadium nitride catalysts: Synthesis and evaluation for n-butane dehydrogenation*. Journal Of Catalysis, 1999. **184**(1): p. 236-246.
6. Krawiec, P., et al., *Oxide foams for the synthesis of high-surface-area vanadium nitride catalysts*. Advanced Materials, 2006. **18**(4): p. 505-+.
7. Edgar, J.H., *Prospects For Device Implementation Of Wide Band-Gap Semiconductors*. Journal Of Materials Research, 1992. **7**(1): p. 235-252.
8. Claridge, J.B., et al., *Study of the temperature-programmed reaction synthesis of early transition metal carbide and nitride catalyst materials from oxide precursors*. Chemistry Of Materials, 2000. **12**(1): p. 132-142.
9. Panda, R.N. and S. Kaskel, *Synthesis and characterization of high surface area molybdenum nitride*. Journal Of Materials Science, 2006. **41**(8): p. 2465-2470.
10. Jacob, K.T., R. Verman, and R.M. Mallya, *Nitride synthesis using ammonia and hydrazine - a thermodynamic panorama*. Journal Of Materials Science, 2002. **37**(20): p. 4465-4472.
11. Vogt, K.W., L.A. Naugher, and P.A. Kohl, *Low-Temperature Nitridation Of Transition-Metals With Hydrazine*. Thin Solid Films, 1995. **256**(1-2): p. 106-115.
12. Weil, K.S., *The synthesis of transition metal nitrides via thermolysis of metal-ammine complexes, Part I: Chromium nitride*. Journal Of Solid State Chemistry, 2008. **181**(1): p. 199-210.
13. Kawaguchi, M. and K. Nozaki, *Synthesis, Structure, And Characteristics Of The New Host Material [(C3n3)(2)(Nh)(3)](N)*. Chemistry Of Materials, 1995. **7**(2): p. 257-264.
14. Zhao, H.Z., et al., *Route to GaN and VN assisted by carbothermal reduction process*. Journal Of The American Chemical Society, 2005. **127**(45): p. 15722-15723.
15. Schuth, F., *Endo- and exotemplating to create high-surface-area inorganic materials*. Angewandte Chemie-International Edition, 2003. **42**(31): p. 3604-3622.
16. Liebig, J., Ann. Pharm., 1834. **10**(10).
17. Cohen, M.L., *Calculation of bulk moduli of diamond and zinc-blende solids*. Physical Review B, 1985. **32**(12): p. 7988.
18. Liu, A.Y. and M.L. Cohen, *Prediction Of New Low Compressibility Solids*. Science, 1989. **245**(4920): p. 841-842.
19. Cohen, M.L., *Novel Materials From Theory*. Nature, 1989. **338**(6213): p. 291-292.
20. Horvath-Bordon, E., et al., *Tri-s-triazine derivatives, part III. Potassium melonate, K-3[C6N7(NCN)(3)]center dot 5H(2)O, and its potential use for the synthesis of graphite-like C3N4 materials*. New Journal Of Chemistry, 2005. **29**(5): p. 693-699.
21. Kroke, E., et al., *Tri-s-triazine derivatives. Part I. From trichloro-tri-s-triazine to graphitic C3N4 structures*. New Journal Of Chemistry, 2002. **26**(5): p. 508-512.
22. Guo, Y.J. and W.A. Goddard, *Is Carbon Nitride Harder Than Diamond - No, But Its Girth Increases When Stretched (Negative Poisson Ratio)*. Chemical Physics Letters, 1995. **237**(1-2): p. 72-76.
23. Teter, D.M. and R.J. Hemley, *Low-compressibility carbon nitrides*. Science, 1996. **271**(5245): p. 53-55.
24. Kroll, P., *Pathways to metastable nitride structures*. Journal Of Solid State Chemistry, 2003. **176**(2): p. 530-537.
25. Bai, X.D., et al., *Hydrogen storage in carbon nitride nanobells*. Applied Physics Letters, 2001. **79**(10): p. 1552-1554.
26. Kouvetakis, J., et al., *Novel Synthetic Routes To Carbon-Nitrogen Thin-Films*. Chemistry Of Materials, 1994. **6**(6): p. 811-814.
27. Montigaud, H., et al., *C3N4: Dream or reality? <Tau Beta > Solvothermal synthesis as macroscopic samples of the C3N4 graphitic form*. Journal Of Materials Science, 2000. **35**(10): p. 2547-2552.
28. Montigaud, H., et al., *Solvothermal synthesis of the graphitic form of C3N4 as macroscopic sample*. Diamond And Related Materials, 1999. **8**(8-9): p. 1707-1710.

29. Zhang, Z.H., et al., *High-pressure bulk synthesis of crystalline C₆N₉H₃ center dot HCl: A novel C₃N₄ graphitic derivative*. Journal Of The American Chemical Society, 2001. **123**(32): p. 7788-7796.
30. Guo, Q.X., et al., *Characterization of well-crystallized graphitic carbon nitride nanocrystallites via a benzene-thermal route at low temperatures*. Chemical Physics Letters, 2003. **380**(1-2): p. 84-87.
31. Guo, Q.X., et al., *Synthesis of carbon nitride nanotubes with the C₃N₄ stoichiometry via a benzene-thermal process at low temperatures*. Chemical Communications, 2004(1): p. 26-27.
32. Kodomari, M., Y. Suzuki, and K. Yoshida, *Graphite as an effective catalyst for Friedel-Crafts acylation*. Chemical Communications, 1997(16): p. 1567-1568.
33. Komatsu, T., *Attempted chemical synthesis of graphite-like carbon nitride*. Journal Of Materials Chemistry, 2001. **11**(3): p. 799-801.
34. Komatsu, T., *Prototype carbon nitrides similar to the symmetric triangular form of melon*. Journal Of Materials Chemistry, 2001. **11**(3): p. 802-805.
35. Komatsu, T., *The first synthesis and characterization of cyameluric high polymers*. Macromolecular Chemistry And Physics, 2001. **202**(1): p. 19-25.
36. Jurgens, B., et al., *Melem (2,5,8-triamino-tri-s-triazine), an important intermediate during condensation of melamine rings to graphitic carbon nitride: Synthesis, structure determination by X-ray powder diffractometry, solid-state NMR, and theoretical studies*. Journal Of The American Chemical Society, 2003. **125**(34): p. 10288-10300.
37. Gu, Y.L., et al., *Synthesis of C₃N₄ and graphite by reacting cyanuric chloride with calcium cyanamide*. Carbon, 2003. **41**(13): p. 2674-2676.
38. Gillan, E.G., *Synthesis of nitrogen-rich carbon nitride networks from an energetic molecular azide precursor*. Chemistry Of Materials, 2000. **12**(12): p. 3906-3912.
39. Miller, D.R., J.R. Holst, and E.G. Gillan, *Nitrogen-rich carbon nitride network materials via the thermal decomposition of 2,5,8-triazido-s-heptazine*. Inorganic Chemistry, 2007. **46**(7): p. 2767-2774.
40. Zimmerman, J.L., et al., *Synthesis of spherical carbon nitride nanostructures*. Nano Letters, 2001. **1**(12): p. 731-734.
41. Lu, X.F., et al., *Synthesis and characterization of C₃N₄ nanowires and pseudocubic C₃N₄ polycrystalline nanoparticles*. Materials Letters, 2007. **61**(21): p. 4255-4258.
42. Li, J., C.B. Cao, and H.S. Zhu, *Synthesis and characterization of graphite-like carbon nitride nanobelts and nanotubes*. Nanotechnology, 2007. **18**(11).
43. Tragl, S., et al., *Template assisted formation of micro- and nanotubular carbon nitride materials*. Solid State Communications, 2007. **141**(9): p. 529-534.
44. Zhao, Y.C., et al., *Turbostratic carbon nitride prepared by pyrolysis of melamine*. Journal Of Materials Science, 2005. **40**(9-10): p. 2645-2647.
45. Lotsch, B.V. and W. Schnick, *From triazines to heptazines: Novel nonmetal tricyanomelaminates as precursors for graphitic carbon nitride materials*. Chemistry Of Materials, 2006. **18**(7): p. 1891-1900.
46. Lotsch, B.V., et al., *Unmasking melon by a complementary approach employing electron diffraction, solid-state NMR spectroscopy, and theoretical calculations-structural characterization of a carbon nitride polymer*. Chemistry-A European Journal, 2007. **13**(17): p. 4969-4980.
47. Niu, C.M., Y.Z. Lu, and C.M. Lieber, *Experimental Realization Of The Covalent Solid Carbon Nitride*. Science, 1993. **261**(5119): p. 334-337.
48. Wu, D.W., et al., *Structure and characteristics of C₃N₄ thin films prepared by rf plasma-enhanced chemical vapor deposition*. Physical Review B, 1997. **56**(8): p. 4949-4954.
49. Guo, L.P., et al., *Identification of a new C-N phase with monoclinic structure*. Chemical Physics Letters, 1997. **268**(1-2): p. 26-30.
50. Chowdhury, A., et al., *Evidence for continuous areas of crystalline beta-C₃N₄ in sputter-deposited thin films*. Journal Of Materials Research, 1999. **14**(6): p. 2359-2363.
51. Groenewolt, M., *Nanostrukturierte Materialien durch neue Templatsysteme und Nutzung mesoporöser Silikate als Nano-Reaktoren*. Doktorarbeit, 2004.
52. Ruland, W. and B. Smarsly, *X-ray scattering of non-graphitic carbon: an improved method of evaluation*. Journal Of Applied Crystallography, 2002. **35**: p. 624-633.
53. Sing, K.S.W., et al., *Reporting Physisorption Data For Gas Solid Systems With Special Reference To The Determination Of Surface-Area And Porosity (Recommendations 1984)*. Pure And Applied Chemistry, 1985. **57**(4): p. 603-619.
54. Brunauer S., E.P., Teller E., *Adsorption of gases in multimolecular layers*. J. Am. Chem. Sci., 1938(60): p. 309-319.

55. Langmuir, I., *The constitution and fundamental properties of solids and liquids. II. Liquids*. Journal Of The American Chemical Society, 1917. **39**: p. 1848-1906.
56. Barrett, E.P., L.G. Joyner, and P.P. Halenda, *The Determination Of Pore Volume And Area Distributions In Porous Substances. I. Computations From Nitrogen Isotherms*. Journal Of The American Chemical Society, 1951. **73**(1): p. 373-380.
57. Johnson, S.A., P.J. Ollivier, and T.E. Mallouk, *Ordered Mesoporous Polymers of Tunable Pore Size from Colloidal Silica Templates*. Science, 1999. **283**(5404): p. 963-965.
58. Vinu, A., et al., *Preparation and characterization of well-ordered hexagonal mesoporous carbon nitride*. Advanced Materials, 2005. **17**(13): p. 1648-+.
59. Vinu, A., T. Mori, and K. Ariga, *New families of mesoporous materials*. Science And Technology Of Advanced Materials, 2006. **7**(8): p. 753-771.
60. Vinu, A., et al., *Three-dimensional cage type mesoporous CN-Based hybrid material with very high surface area and pore volume*. Chemistry Of Materials, 2007. **19**(17): p. 4367-4372.
61. Groenewolt, M. and M. Antonietti, *Synthesis of g-C₃N₄ nanoparticles in mesoporous silica host matrices*. Advanced Materials, 2005. **17**(14): p. 1789-+.
62. Soler-illia, G.J.D., et al., *Chemical strategies to design textured materials: From microporous and mesoporous oxides to nanonetworks and hierarchical structures*. Chemical Reviews, 2002. **102**(11): p. 4093-4138.
63. Taguchi, A. and F. Schuth, *Ordered mesoporous materials in catalysis*. Microporous And Mesoporous Materials, 2005. **77**(1): p. 1-45.
64. Shahbaz, M., et al., *Tri-S-Triazine - Synthesis, Chemical Behavior, And Spectroscopic And Theoretical Probes Of Valence Orbital Structure*. Journal Of The American Chemical Society, 1984. **106**(10): p. 2805-2811.
65. Enoki, T. and Y. Kobayashi, *Magnetic nanographite: an approach to molecular magnetism*. Journal Of Materials Chemistry, 2005. **15**(37): p. 3999-4002.
66. Tomita, S., et al., *Structure and electronic properties of carbon onions*. Journal Of Chemical Physics, 2001. **114**(17): p. 7477-7482.
67. Endo, M., et al., *Scanning tunneling microscope study of boron-doped highly oriented pyrolytic graphite*. Journal Of Applied Physics, 2001. **90**(11): p. 5670-5674.
68. Su, D.S., et al., *Nanocarbons in selective oxidative dehydrogenation reaction*. Catalysis Today, 2005. **102**: p. 110-114.
69. Macia-Agullo, J.A., et al., *Oxygen functional groups involved in the styrene production reaction detected by quasi in situ XPS*. Catalysis Today, 2005. **102**: p. 248-253.
70. Laporte, C., et al., *Acylation of aromatics under microwaves in the presence of graphite*. Comptes Rendus De L Academie Des Sciences Serie Ii Fascicule C-Chimie, 1998. **1**(2): p. 141-150.
71. Kruk, M., et al., *Synthesis and characterization of hexagonally ordered carbon nanopipes*. Chemistry Of Materials, 2003. **15**(14): p. 2815-2823.
72. Yoo, S., et al., *Engineering nanospaces: OMS/dendrimer hybrids possessing controllable chemistry and porosity*. Chemistry Of Materials, 2006. **18**(13): p. 2935-2942.
73. Pileni, M.P., *The role of soft colloidal templates in controlling the size and shape of inorganic nanocrystals*. Nature Materials, 2003. **2**(3): p. 145-150.
74. Liu, S.Y., et al., *Synthesis of pH-responsive shell cross-linked micelles and their use as nanoreactors for the preparation of gold nanoparticles*. Langmuir, 2002. **18**(22): p. 8350-8357.
75. Kane, R.S., R.E. Cohen, and R. Silbey, *Synthesis of PbS nanoclusters within block copolymer nanoreactors*. Chemistry Of Materials, 1996. **8**(8): p. 1919-1924.
76. Kane, R.S., R.E. Cohen, and R. Silbey, *Synthesis of doped ZnS nanoclusters within block copolymer nanoreactors*. Chemistry Of Materials, 1999. **11**(1): p. 90-93.
77. Hamley, I.W., *Nanostructure fabrication using block copolymers*. Nanotechnology, 2003. **14**(10): p. R39-R54.
78. Bronstein, L., et al., *Successive use of amphiphilic block copolymers as nanoreactors and templates: Preparation of porous silica with metal nanoparticles*. Chemistry Of Materials, 1999. **11**(6): p. 1402-+.
79. Groger, H., et al., *Enantioselective enzymatic reactions in miniemulsions as efficient "nanoreactors"*. Angewandte Chemie-International Edition, 2006. **45**(10): p. 1645-1648.
80. Musyanovych, A., V. Mailander, and K. Landfester, *Miniemulsion droplets as single molecule nanoreactors for polymerase chain reaction*. Biomacromolecules, 2005. **6**(4): p. 1824-1828.
81. Taden, A., et al., *Inorganic films from three different phosphors via a liquid coating route from inverse miniemulsions*. Chemistry Of Materials, 2004. **16**(24): p. 5081-5087.
82. Antonietti, M., et al., *Nonclassical shapes of noble-metal colloids by synthesis in microgel nanoreactors*. Angewandte Chemie-International Edition In English, 1997. **36**(19): p. 2080-2083.

83. Thomas, A., F. Goettmann, and M. Antonietti, *Hard Templates for Soft Materials: Creating Nanostructured Organic Materials*. Chem. Mater., 2008. **20**(3): p. 738-755.
84. Napolsky, K.S., et al., *Preparation of ordered magnetic iron nanowires in the mesoporous silica matrix*. Materials Science & Engineering C-Biomimetic And Supramolecular Systems, 2003. **23**(1-2): p. 151-154.
85. Guari, Y., et al., *Indium and indium-oxide nanoparticle or nanorod formation within functionalised ordered mesoporous silica*. New Journal Of Chemistry, 2003. **27**(7): p. 1029-1031.
86. Li, Y.Z. and S.J. Kim, *Synthesis and characterization of nano titania particles embedded in mesoporous silica with both high photocatalytic activity and adsorption capability*. Journal Of Physical Chemistry B, 2005. **109**(25): p. 12309-12315.
87. Yang, H.F., et al., *One-step nanocasting synthesis of highly ordered single crystalline indium oxide nanowire arrays from mesostructured frameworks*. Journal Of The American Chemical Society, 2003. **125**(16): p. 4724-4725.
88. Zhang, Z.T., et al., *Controlled synthesis of CdS nanoparticles inside ordered mesoporous silica using ion-exchange reaction*. Journal Of Physical Chemistry B, 2001. **105**(29): p. 6755-6758.
89. Hsueh, H.S., et al., *Formation of titanium nitride nanoparticles within mesoporous silica SBA-15*. Journal Of Physical Chemistry B, 2005. **109**(10): p. 4404-4409.
90. Ryoo, R., et al., *Ordered mesoporous carbons*. Advanced Materials, 2001. **13**(9): p. 677-681.
91. Groenewolt, M., A. Thomas, and M. Antonietti, *Nanoparticles and nanosheets of aromatic polyimides via polycondensation in controlled pore geometries*. Macromolecules, 2004. **37**(12): p. 4360-4364.
92. Goettmann F., F.A., Antonietti M. & Thomas A., *Chemical Synthesis of Mesoporous Carbon Nitrides Using Hard Templates and Their Use as a Metal-Free Catalyst for Friedel-Crafts Reaction of Benzene*. Angewandte Chemie-International Edition In English, 2006. **45**(27): p. 4467-4471.
93. Sirvio, E.H., M. Sulonen, and H. Sundquist, *Abrasive wear of ion-plated titanium nitride coatings on plasma-nitrided steel surfaces*. Thin Solid Films, 1982. **96**(1): p. 93.
94. Kaskel, S. and K. Schlichte, *Porous silicon nitride as a superb catalyst*. Journal Of Catalysis, 2001. **201**(2): p. 270-274.
95. Ponce, F.A. and D.P. Bour, *Nitride-based semiconductors for blue and green light-emitting devices*. Nature, 1997. **386**(6623): p. 351.
96. Li, P.G., et al., *Preparation of nitrides and carbides from g-C₃N₄*. Materials Chemistry And Physics, 2007. **105**(2-3): p. 234-239.
97. Lei, A., et al., *Ammonium dicyanamide as a precursor for the synthesis of metal nitride and carbide nanoparticles*. Diamond And Related Materials, 2007. **16**(11): p. 1974-1981.
98. Chen, X.Z., et al., *Synthesis of transition-metal nitrides from nanoscale metal particles prepared by homogeneous reduction of metal halides with an alkali*. Chemistry Of Materials, 1997. **9**(5): p. 1172-1176.
99. Sun, X.M. and Y.D. Li, *Ga₂O₃ and GaN semiconductor hollow spheres*. Angewandte Chemie-International Edition, 2004. **43**(29): p. 3827-3831.
100. Gole, J.L., et al., *Highly efficient formation of visible light tunable TiO₂-xN_x photocatalysts and their transformation at the nanoscale*. Journal Of Physical Chemistry B, 2004. **108**(4): p. 1230-1240.
101. Qian, Y.T., *Solvothermal synthesis of nanocrystalline III-V semiconductors*. Advanced Materials, 1999. **11**(13): p. 1101-+.
102. Sardar, K., et al., *InN nanocrystals, nanowires, and nanotubes*. Small, 2005. **1**(1): p. 91-94.
103. Sardar, K. and C.N.R. Rao, *New solvothermal routes for GaN nanocrystals*. Advanced Materials, 2004. **16**(5): p. 425-+.
104. Wang, Y., Z.H. Jiang, and F.J. Yang, *Preparation and photocatalytic activity of mesoporous TiO₂ derived from hydrolysis condensation with TX-100 as template*. Materials Science And Engineering B-Solid State Materials For Advanced Technology, 2006. **128**(1-3): p. 229-233.
105. Niederberger, M., M.H. Bartl, and G.D. Stucky, *Benzyl alcohol and titanium tetrachloride - A versatile reaction system for the nonaqueous and low-temperature preparation of crystalline and luminescent titania nanoparticles*. Chemistry Of Materials, 2002. **14**(10): p. 4364-4370.
106. Hasegawa, M. and T. Yagi, *Systematic study of formation and crystal structure of 3d-transition metal nitrides synthesized in a supercritical nitrogen fluid under 10 GPa and 1800 K using diamond anvil cell and YAG laser heating*. Journal of Alloys and Compounds, 2005. **403**(1-2): p. 131.
107. Christensen, A.N., *A neutron diffraction investigation of single crystals of titanium carbide, titanium nitride, and zirconium nitride*. Acta Chemica Scandinavica, Series A, 1975. **29**: p. 563-568.
108. Zhao, H.Z., et al., *Facile route to metal nitrides through melamine and metal oxides*. Journal Of Materials Chemistry, 2006. **16**(45): p. 4407-4412.

109. Buha, J., et al., *Thermal transformation of metal oxide nanoparticles into nanocrystalline metal nitrides using cyanamide and urea as nitrogen source*. Chemistry Of Materials, 2007. **19**(14): p. 3499-3505.
110. Metcalfe, A.E., *The mutual solid solubility of tungsten carbide and titanium carbide*. Journal of the Institute of Metals, 1947. **73**: p. 591-607.
111. Duwez, P. and F. Odell, *Phase relationships in the binary systems of nitrides and carbides of zirconium, columbium, titanium, and vanadium*. Journal of the Electrochemical Society, 1950. **97**: p. 299-304.
112. Chase, M.W., Jr., *NIST-JANAF Thermochemical Tables, Fourth Edition*. J. Phys. Chem. Ref. Data, Monograph 9, 1998: p. 1-1951.
113. Choi, D. and P.N. Kumta, *Nanocrystalline TiN derived by a two-step halide approach for electrochemical capacitors*. Journal Of The Electrochemical Society, 2006. **153**(12): p. A2298-A2303.
114. Hosoya, S., T. Yamagishi, and M. Tokonami, *Study of electron state in vanadium nitride by intensity measurements of X-Ray diffraction*. Journal of the Physical Society of Japan, 1968. **24**: p. 363-367.
115. Timofeeva, I.I. and L.K. Shvedova, *Microhardness and thermal expansion of transition metal nitrides at 80-300 K*. Izvestiya Akademii Nauk SSSR, Neorganicheskie Materialy, 1972. **8**: p. 1169-1170.
116. Becker, K. and F. Ebert, *Die Kristallstrukturen einiger binärer Carbide und Nitride*. Zeitschrift fuer Physik, 1925. **31**: p. 268-272.
117. Pflueger, J., et al., *Dielectric properties of Ti C_x, Ti N_x, V C_x, and V N_x from 1.5 to 40 eV determined by electron-energy-loss spectroscopy*. Physical Review, Serie 3. B - Condensed Matter, 1984. **30**: p. 1155-1163.
118. Juza, R. and H. Hahn, *Ueber die Kristallstrukturen von Cu₃ N, Ga N und In N*. Zeitschrift fuer Anorganische und Allgemeine Chemie, 1938. **239**: p. 282-287.
119. Schulz, H. and K.H. Thiemann, *Crystal structure refinement of Al N and Ga N*. Solid State Communications, 1977. **23**: p. 815-819.
120. Ponce, F.A. and D.P. Bour, *Nitride-based semiconductors for blue and green light-emitting devices*. Nature, 1997. **386**(6623): p. 351-359.
121. Benaissa, M., K.E. Gonsalves, and S.P. Rangarajan, *AlGa_N nanoparticle/polymer composite: Synthesis, optical, and structural characterization*. Applied Physics Letters, 1997. **71**(25): p. 3685-3687.
122. Jain, S.C., et al., *III-nitrides: Growth, characterization, and properties*. Journal Of Applied Physics, 2000. **87**(3): p. 965-1006.
123. Latella, B.A., et al., *Titanium nitride/vanadium nitride alloy coatings: mechanical properties and adhesion characteristics*. Surface & Coatings Technology, 2006. **200**(11): p. 3605-3611.
124. A. Fischer, M.A.A.T., *Growth Confined by the Nitrogen Source: Synthesis of Pure Metal Nitride Nanoparticles in Mesoporous Graphitic Carbon Nitride*. Advanced Materials, 2007. **19**(2): p. 264-267.
125. Corma, A., *From Microporous to Mesoporous Molecular Sieve Materials and Their Use in Catalysis*. Chem. Rev., 1997. **97**(6): p. 2373-2420.
126. Sanchez, C., et al., *Optical properties of functional hybrid organic-inorganic nanocomposites*. Advanced Materials, 2003. **15**(23): p. 1969-1994.
127. Scott, B.J., G. Wirnsberger, and G.D. Stucky, *Mesoporous and mesostructured materials for optical applications*. Chemistry Of Materials, 2001. **13**(10): p. 3140-3150.
128. Choi, S.Y., et al., *Thermally stable two-dimensional hexagonal mesoporous nanocrystalline anatase, meso-nc-TiO₂: Bulk and crack-free thin film morphologies*. Advanced Functional Materials, 2004. **14**(4): p. 335-344.
129. Grosso, D., et al., *Periodically ordered nanoscale islands and mesoporous films composed of nanocrystalline multimetallic oxides*. Nature Materials, 2004. **3**(11): p. 787-792.
130. Smarsly, B. and M. Antonietti, *Block copolymer assemblies as templates for the generation of mesoporous inorganic materials and crystalline films*. European Journal Of Inorganic Chemistry, 2006(6): p. 1111-1119.
131. Dibandjo, P., et al., *Synthesis of boron nitride with ordered mesostructure*. Advanced Materials, 2005. **17**(5): p. 571-+.
132. Cheng, F., et al., *Preparation of mesoporous silicon nitride via a nonaqueous sol-gel route*. Journal Of The American Ceramic Society, 2004. **87**(8): p. 1413-1417.
133. Cheng, F., et al., *Preparation of a mesoporous silicon boron nitride via a non-aqueous sol-gel route*. Chemical Communications, 2003(2): p. 242-243.

134. Kaskel, S., K. Schlichte, and B. Zibrowius, *Pore size engineering of mesoporous silicon nitride materials*. Physical Chemistry Chemical Physics, 2002. **4**(9): p. 1675-1681.
135. Oyama, S.T., *The Chemistry of Transition Metal Carbides and Nitrides*, ed. S.T. Oyama. 1996, London: Blackie Academic & Professional.
136. Sirvio, E.H., M. Sulonen, and H. Sundquist, *Abrasive Wear Of Ion-Plated Titanium Nitride Coatings On Plasma-Nitrided Steel Surfaces*. Thin Solid Films, 1982. **96**(1): p. 93-101.
137. Janes, R.A., M. Aldissi, and R.B. Kaner, *Controlling surface area of titanium nitride using metathesis reactions*. Chemistry Of Materials, 2003. **15**(23): p. 4431-4435.
138. Kaskel, S., et al., *Synthesis and characterisation of titanium nitride based nanoparticles*. Journal Of Materials Chemistry, 2003. **13**(6): p. 1496-1499.
139. Li, J.G., et al., *Synthesis of nanocrystalline titanium nitride powders by direct nitridation of titanium oxide*. Journal Of The American Ceramic Society, 2001. **84**(12): p. 3045-3047.
140. Ning, J., et al., *XPS study for reactively sputtered titanium nitride thin films deposited under different substrate bias*. Physica B-Condensed Matter, 2004. **352**(1-4): p. 118-126.
141. Qiu, Y. and L. Gao, *Novel polyaniline/titanium nitride nanocomposite: Controllable structures and electrical/electrochemical properties*. Journal Of Physical Chemistry B, 2005. **109**(42): p. 19732-19740.
142. Oyama, S.T., *Preparation And Catalytic Properties Of Transition-Metal Carbides And Nitrides*. Catalysis Today, 1992. **15**(2): p. 179-200.
143. Antonelli, D.M., *Synthesis of phosphorus-free mesoporous titania via templating with amine surfactants*. Microporous And Mesoporous Materials, 1999. **30**(2-3): p. 315-319.
144. Grosso, D., et al., *Highly organized mesoporous titania thin films showing mono-oriented 2D hexagonal channels*. Advanced Materials, 2001. **13**(14): p. 1085-+.
145. Smarsly, B., et al., *Highly crystalline cubic mesoporous TiO₂ with 10-nm pore diameter made with a new block copolymer template*. Chemistry Of Materials, 2004. **16**(15): p. 2948-2952.
146. Soler-Illia, G., A. Louis, and C. Sanchez, *Synthesis and characterization of mesostructured titania-based materials through evaporation-induced self-assembly*. Chemistry Of Materials, 2002. **14**(2): p. 750-759.
147. Alberius, P.C.A., et al., *General predictive syntheses of cubic, hexagonal, and lamellar silica and titania mesostructured thin films*. Chemistry Of Materials, 2002. **14**(8): p. 3284-3294.
148. Wang, Y., Z.H. Jiang, and F.J. Yang, *Effect of Fe-doping on the pore structure of mesoporous titania*. Materials Science And Engineering B-Solid State Materials For Advanced Technology, 2006. **134**(1): p. 76-79.
149. Hasegawa, M. and T. Yagi, *Systematic study of formation and crystal structure of 3d-transition metal nitrides synthesized in a supercritical nitrogen fluid under 10 GPa and 1800 K using diamond anvil cell and YAG laser heating*. Journal Of Alloys And Compounds, 2005. **403**(1-2): p. 131-142.
150. K. Yvon, W.J.a.E.P., J. Appl. Cryst., 1977. **10**: p. 73.
151. Wang, X., et al., *Multi-type carbon doping of TiO₂ photocatalyst*. Chemical Physics Letters, 2007. **444**(4-6): p. 292.
152. Yvon, K., W. Jeitschko, and E. Parthe, *Lazy Pulverix, A Computer-Program, For Calculating X-Ray And Neutron-Diffraction Powder Patterns*. Journal Of Applied Crystallography, 1977. **10**(FEB1): p. 73-74.
153. Neylon, M.K., et al., *Ethanol amination catalysis over early transition metal nitrides*. Applied Catalysis A-General, 2002. **232**(1-2): p. 13-21.
154. McGee, R.C.V., S.K. Bej, and L.T. Thompson, *Basic properties of molybdenum and tungsten nitride catalysts*. Applied Catalysis A-General, 2005. **284**(1-2): p. 139-146.
155. Mestres, R., *A green look at the aldol reaction*. Green Chemistry, 2004. **6**(12): p. 583-603.
156. Corma, A. and H. Garcia, *Silica-bound homogenous catalysts as recoverable and reusable catalysts in organic synthesis*. Advanced Synthesis & Catalysis, 2006. **348**(12-13): p. 1391-1412.
157. Figueras, F., M.L. Kantam, and B.M. Choudary, *Solid base catalysts in organic synthesis*. Current Organic Chemistry, 2006. **10**(13): p. 1627-1637.
158. Makowski, P., New Journal of Chemistry, 2008.
159. Goettmann, F., et al., *New hybrid bidentate ligands as precursors for smart catalysts*. Chemistry-A European Journal, 2005. **11**(24): p. 7416-7426.
160. Goettmann, F., P. Le Floch, and C. Sanchez, *Highly regioselective terminal alkynes hydroformylation and Pauson-Khand reaction catalysed by mesoporous organised zirconium oxide based powders*. Chemical Communications, 2006(2): p. 180-182.
161. Kwon, M.S., et al., *Recyclable palladium catalyst for highly selective alpha alkylation of ketones with alcohols*. Angewandte Chemie-International Edition, 2005. **44**(42): p. 6913-6915.